Department of Precision and Microsystems Engineering

Optimization of the hot-filament chemical vapor deposition setup

Dilpreet Singh

Report no : 2023.030
Coach : Dr. J.G. Buijnsters
Professor : Dr. J.G. Buijnsters
Specialisation : Micro and Nano Engineering (MNE)
Type of report : Thesis
Date : 13 June 2023

Optimization of the hot-filament chemical vapor deposition setup

Investigating the effects of filament placement and exploring the growth conditions for diamond synthesis

Dilpreet Singh

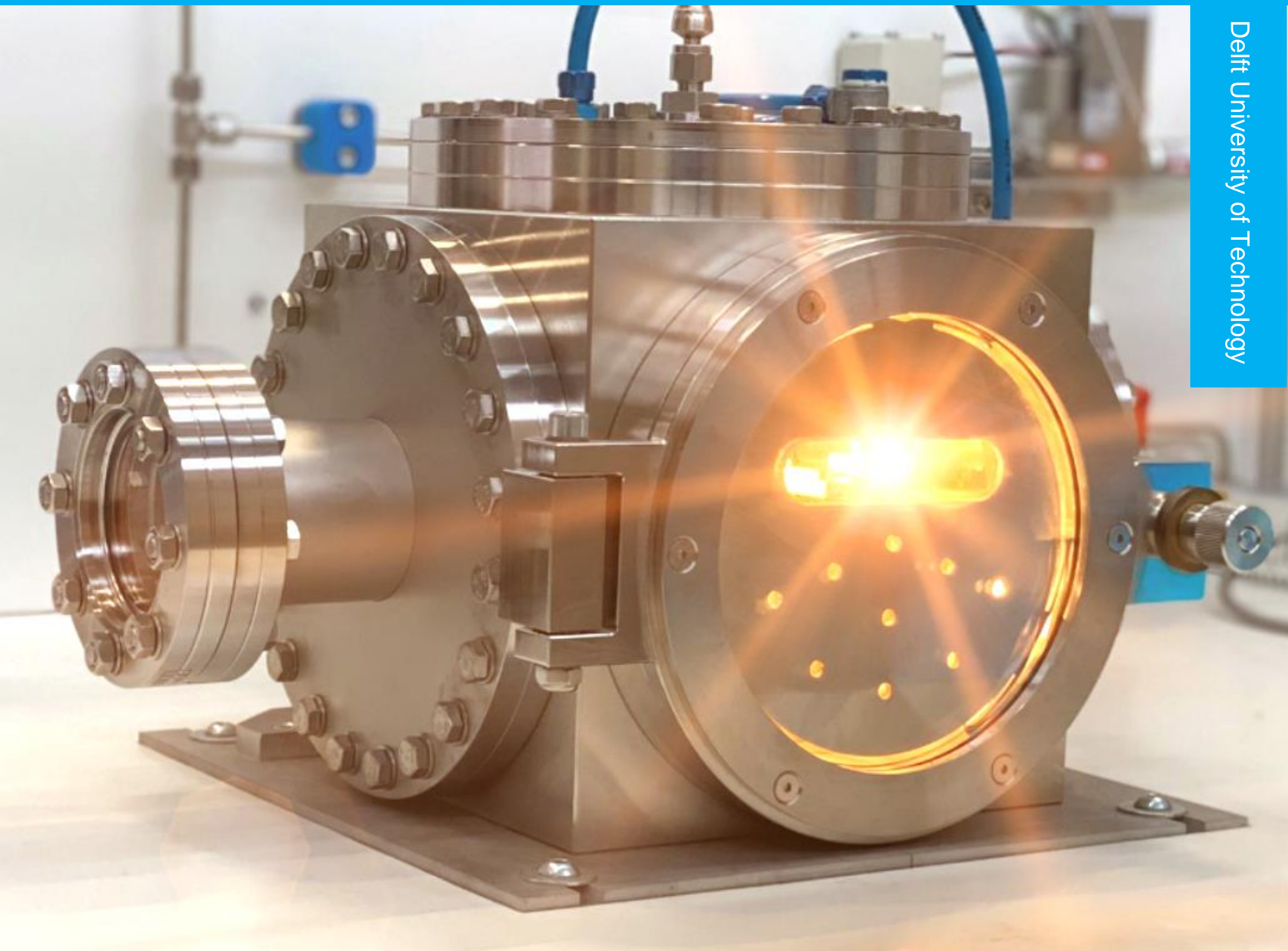

Delft University of Technology

TU Delft

Optimization of the hot-filament chemical vapor deposition setup

Investigating the effects of filament placement and exploring the growth conditions for diamond synthesis

By

Dilpreet Singh

in partial fulfilment of the requirements for the degree of

Master of Science
in Mechanical Engineering

at the Delft University of Technology,
to be defended publicly on Tuesday June 13, 2023 at 14:30 AM.

Student number: 4496892

Thesis supervisor:	dr. J.G. Buijnsters	TU Delft
Thesis committee:	dr. J.G. Buijnsters (chair)	TU Delft
	dr. A. Hunt	TU Delft
	dr.ir. S. Vollebregt	TU Delft
	dr. S. Baluchová	TU Delft

An electronic version of this thesis is available at http://repository.tudelft.nl/.

Acknowledgements

I would like to express my deepest gratitude to all those who have supported and contributed to the successful completion of this thesis project.

First and foremost, I would like to thank my supervisor, Dr. Ivan Buijnsters, for his exceptional guidance, friendship, and sustained support throughout the course of this project. His enthusiasm and extensive knowledge on diamonds and thin films have played a key role in the completion of this research work. I would also like to express my appreciation for the opportunities he provided me to present my research during various project-related events. Working with him has been an invaluable experience, and I feel truly fortunate to have had him as my supervisor.

I would also like to thank Simona Baluchová and Zhichao Liu for their involvement and interest in this project. It was always reassuring to know that I could turn to you for questions and advice, both on a professional and personal level. I am truly grateful for your continuous presence, support, and encouragement during this project.

Furthermore, I would like to extend my gratitude to the technical support staff at PME for their active involvement in this project. In particular, Bradley, Alex, Gideon, and Patrick were my reliable pillars of support whenever a technical problem occurred that required immediate action. Their quick response and involvement in this project were truly remarkable.

Thank you to all the fellow graduate students, researchers, and PME staff members for their presence, and interest in my research topic.

I would like to express my sincere gratitude to my family for their presence and support throughout this journey. Their love, encouragement, and belief in me have been a constant source of motivation. Thank you for always being there for me!

I am also grateful for the friends I made during my years as a student. Our time together in Delft was not only about studying but also about creating unforgettable memories. Thank you for being a part of this wonderful journey.

Dilpreet Singh
Amsterdam, May 2023

Abstract

The hot-filament chemical vapor deposition (HF-CVD) method is widely used for the synthesis of thin films of polycrystalline diamond. These films are used in a broad range of applications, such as coating material on cutting tools, heat spreaders, and electrochemical sensors. HF-CVD offers some unique advantages in terms of simplicity, low equipment cost, and scalability.

Recently, a novel HF-CVD system has been designed and built at dept. PME (TU Delft), which should enable diamond deposition over relatively large substrate areas (i.e., two-inch wafers) by employing an array of multiple straight metallic filaments. However, the use of this setup so far has been primarily restricted due to the premature failure of the tungsten filaments. During the high-temperature chemical vapor deposition process, the filaments undergo large deformations due to carburization, leading to the formation of brittle metal carbides. In the initial configuration, the filaments were placed in a custom-made clamping device, obstructing their ability to expand and contract freely, resulting in residual mechanical stresses that caused premature failure of the filaments after cooling down. To enable diamond growth in this setup, a new approach is needed.

In this research, different placements of the filaments within the existing clamping device were tested to determine the optimized placement that ensures a longer filament lifespan. Additionally, a preliminary experimental parameter study was performed to investigate the effects of different deposition parameters (i.e., filament-substrate distance, stage temperature, and methane concentration) on the diamond growth on Si (100) substrates.
The optimized filament placement was achieved by simply resting the tungsten filament on both electrodes without additional fixations. In this configuration, the filaments could be used for multiple interrupted deposition runs, and even after 162 hours of usage, the filaments remained intact. The average carburization time required to reach a constant filament power consumption and to initiate the thin-film growth of diamond was found to be 8 hours when using 0.5 vol.% methane and 5 hours when using 1.0 vol.%. As the carburization proceeded, the filaments elongated and exhibited a sagging effect. The growth experiments showed that dense polycrystalline diamond films can be synthesized in this setup with growth rates ranging from ~50 nm/h to 300 nm/h depending on the deposition parameters. As diamond growth is a temperature-driven process, the substrate temperature was found to have a particularly strong effect on the film growth rate in the investigated range of 360 to 780 °C. Finally, based on the experimental results, new designs for the clamping device are proposed to maintain straight filaments during the deposition process in future experiments.

Contents

1. Introduction 1
2. Literature Review 3
2.1 Diamond and graphite 3
2.2 Diamond synthesis 5
2.2.1 High-Pressure-High-Temperature (HPHT) 5
2.2.2 Detonation nanodiamond (DND) 5
2.2.3 Chemical Vapor Deposition (CVD) 5
2.2.4 Process parameters 8
2.2.5 Substrate for diamond growth 9
2.2.6 Polycrystalline diamond films 10
2.2.7 Applications 11
2.3 Filament characteristics 12
2.3.1 Filament properties 12
2.3.2 Carburization process in detail 12
2.3.3 Filament behavior 13
3. Research focus 18
3.1 Problem statement 18
3.2 Goal of this research 18
3.3 Research questions 18
4. Methodology 19
4.1 HF-CVD setup 19
4.2 Materials 20
4.3 Filament carburization experiments 20
4.4 Pyrometer 21
4.5 Seeding 21
4.6 Diamond film growth experiments 22
4.7 Scanning electron microscopy 22
4.8 Raman spectroscopy 22
4.9 Software 22

5. Results and discussion 23
5.1 Extended lifespan of single W filament 23
5.1.1 Filament configurations 23
5.1.2 Filament carburization 27
5.2 Diamond growth 30
5.2.1 Parametric growth conditions 30
5.2.2 Substrate pre-treatment 31
5.2.3 Filament-substrate distance variation 32
5.2.4 Stage temperature variation 36
5.2.5 Methane concentration variation 40
5.3 Clamping device 44
5.3.1 Boundary conditions and functional requirements 44
5.3.2 Material selection 45
5.3.3 Conceptualization 45
6. Conclusions and recommendations for future work 49
6.1 Conclusions 49
6.2 Recommendations for future work 50
7. Bibliography 51
8. Appendix 56

1. Introduction

Diamonds find great interest from science and industry owing to their outstanding properties, including extreme hardness, wide optical transparency, the highest thermal conductivity at room temperature, and excellent chemical inertness [1–3]. However, the direct use of natural diamonds in engineering applications is limited for several reasons, such as high cost, varying quality, and difficulties in processing to make them suitable for specific uses. Developments in diamond synthesis techniques have overcome these limitations. At present, thin films of polycrystalline diamond (PCD) can be synthesized under low pressure conditions through a technique called chemical vapor deposition (CVD). Diamond thin films are already being used in many applications, such as coating materials on cutting tools, heat spreaders, and optical windows [4–6]. The properties of these diamond films can be tuned by adding impurities, dopants, and other extended defects. For example, electrically conductive diamond films can be produced by introducing boron dopants into the diamond lattice. This is also referred to as boron-doped diamond (BDD). In the field of electrochemistry, BDD is showing great potential for many uses, e.g., biosensors and wastewater treatment [7, 8].

Among the several CVD techniques, the hot-filament chemical vapor deposition (HF-CVD) method offers some unique advantages in terms of low equipment cost and scalability [9]. In most HF-CVD setups, tungsten (W) and tantalum (Ta) wires are used as filaments for the activation of the injected precursors (methane and hydrogen) to produce PCD films. A HF-CVD system can simply be scaled up by increasing the filament length or by adding more filaments to the precursor activation zone [10]. This allows the deposition of diamond over larger substrate areas. A major drawback of the HF-CVD method is the large deformation and embrittlement of the filaments as a result of carburization, which ultimately leads to the premature failure of the filaments. Particularly when heat and cooling cycles are involved, thermal stresses tend to shorten the filament's life even further. For steady and efficient diamond growth, prolonged and repeated use of the same filaments is essential.

Recently, a novel HF-CVD system has been designed and built at dept. PME (TU Delft), which should enable the uniform deposition of diamond films (primarily BDD material) over a relatively large substrate area (i.e., two-inch wafers). In this setup, an array of multiple straight filaments of equal length with equal wire spacing are placed next to each other in a custom-made clamping device. In the initial configuration, the filaments were restricted from expanding and contracting, which resulted in the development of residual stresses and subsequently led to the failure of the carburized filaments after cooling down. Premature failure of the filaments has delayed the use of the new HF-CVD system.

The main objective of this MSc. thesis project was to enable diamond growth in the new HF-CVD setup. Several experiments were conducted throughout this research. This project is divided into three main research activities. The first step was to extend the lifespan of the filaments, as this allows the formation of reactive species from the chemical precursors needed for diamond growth. Next, a growth study was performed to investigate the isolated effects of various deposition parameters (filament-substrate distance, stage temperature, and methane concentrations) on the morphology and quality of diamond films. Finally, preliminary concept designs for the clamping mechanism to maintain straight filaments during the deposition process are proposed.

This report is divided into six chapters, with the introduction being the first. Chapter 2 provides a comprehensive theoretical background on diamond synthesis through chemical vapor deposition methods. It also includes an in-depth literature survey on the carburization of W filaments and the existing approaches that are currently being used to extend the lifespan of filaments. Chapter 3 summarizes the problem statement, research objectives, and research questions, setting the framework for this research. Chapter 4 outlines the methods used in this research, including a description of the HF-CVD setup, experimental procedures (e.g., sample preparation, monitoring carburization, etc.), and characterization techniques. Chapter 5 presents the results and discussion of this project. This chapter is divided into three parts: the first part discusses the experimental results of different filament placements with a focus on extending their lifespan; the second part deals with the results obtained from the parametric growth study; and the third part outlines the preliminary designs for the new clamping mechanism. Finally, chapter 6 concludes this research by summarizing the key findings and providing recommendations for future work.

2. Literature Review

This chapter provides an overview of the carbon allotropes diamond and graphite, diamond synthesis techniques, and filament characteristics.

2.1 Diamond and graphite

Diamond and graphite are both allotropes of carbon. Although they are entirely made up of carbon atoms, their properties are completely different. The different properties are due to the different arrangements and bonding of the carbon atoms. This section starts with a brief explanation of the hybridization process essential for shaping the respective crystal structures. Next, the crystal structures and material properties of diamond and graphite will be discussed.

2.1.1 Crystal structure

In diamond, each carbon atom is bonded to four neighboring carbon atoms by the so-called sp^3 hybridized orbitals. On the other hand, in graphite, each carbon atom is bonded to three neighboring carbon atoms by sp^2 hybridized orbitals. The atomic orbitals needed to form these hybridized orbitals are shown in Figure 2.1 [11].

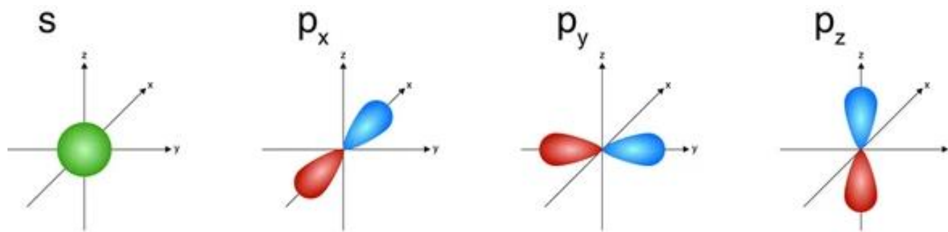

Figure 2.1: Atomic *s* and *p* orbitals [11]

In the case of diamond, four sp^3 orbitals are created by combining three *2p* orbitals and a single *2s* orbital, yielding four σ-bonds arranged in a tetrahedral geometry as shown in Figure 2.2a [12]. Similarly, sp^2 hybridization occurs when two *2p* orbitals and a single *2s* orbital are mixed together to form three σ-bonds arranged in the trigonal planar geometry (see Figure 2.2b). In this case, one *p* orbital did not participate in the hybridization, which means that each carbon atom features one non-bonded electron, known as a delocalized electron. The sp^3 hybridized carbon atoms tend to form a three-dimensional crystal structure known as the diamond lattice, as illustrated in Figure 2.3a [13]. The carbon atoms inside the lattice are bonded to four other carbon atoms according to the tetrahedral geometry. The diamond lattice is isomeric and can be considered as a combination of two face-centered cubic (FCC) lattices that have been merged by moving them relative to each other along the diagonal axis by a_0(¼,¼,¼), with a_0 being the lattice constant (1.54 Å) [14]. The dense-packed lattice structure of diamond exhibits the highest atomic number density and strong covalent carbon-carbon bonds. This gives rise to diamond's superior material properties. Graphite consists of stacked layers of sp^2 hybridized carbon atoms arranged in a hexagonal structure (see Figure 2.3b). The layers are stacked parallel to each other according to the ABABAB… sequence. The individual layers of carbon atoms are known as graphene. Within a single graphene layer, the carbon atoms are bonded covalently, while the adjacent graphene layers are loosely held together by weak π bonds.

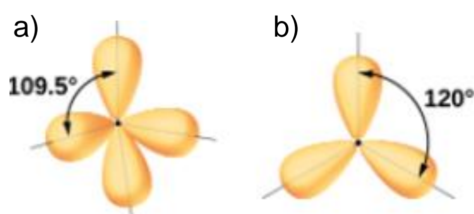

Figure 2.2: a) Sp^3 orbitals and b) sp^2 orbitals [12]

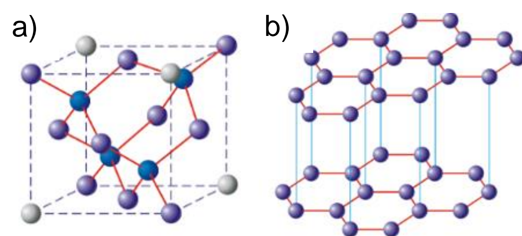

Figure 2.3: Allotropes of carbon: a) Diamond unit cell and b) crystal structure of graphite [13]

2.1.2 Carbon phase stability

Diamond is thermodynamically stable under extremely high pressure and temperature conditions (see Figure 2.4) [15]. Still, at 298 K and 1 atm pressure, diamond exists as a solid. At these conditions, one would expect diamond to convert into the more thermodynamically stable graphite. Still, diamond gems have remained unchanged over centuries and have not converted into the stable graphite phase. This phase transformation is inhibited by the large energy barrier between the two different carbon phases. A large amount of energy (0.4 eV per atom) is required to convert diamond into graphite due to the strong covalent bonding between the carbon atoms. Therefore, it is said that diamond is metastable at room temperature and atmospheric pressure. Once a diamond has formed, it does not conveniently reconvert into graphite [1]. This is exploited in the so-called chemical vapor deposition (CVD) of diamond and will be explained in more detail in Section 2.2.3.

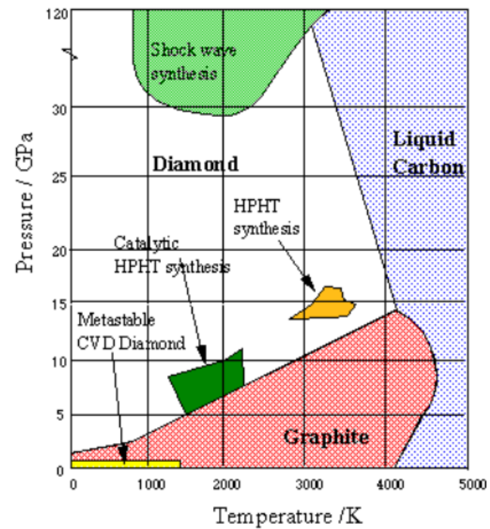

Figure 2.4: The phase diagram of carbon indicating the pressure-temperature conditions of various diamond synthesis methods [15]

2.1.3 Material properties

Diamond and graphite have different properties due to their distinct crystal structures. The appearance of diamond is transparent and shiny, while graphite is opaque and gray-black in color. Diamond possesses excellent properties, including extreme hardness, high electrical resistance, a low thermal expansion coefficient, high chemical inertness, and wide optical transparency [16]. Contrarily, graphite is soft and greasy and can conduct electricity. The softness is due to the relatively weak van der Waals forces by which the adjacent graphene layers are held together, and the presence of the delocalized electrons explains its electrical conductivity. There are various types of natural graphite, and the carbon content varies among these types, resulting in diverging material properties. A selection of material properties for single-crystal diamond and graphite are given in Table 2.1.

Table 2.1: Properties of diamond and graphite [16]

Properties	Diamond	Graphite
Crystal structure	Cubic	Hexagonal
Density (g/cm^3)	3.52	2.26
Mohs hardness	10	~1
Thermal conductivity ($W\ m^{-1}\ K^{-1}$)	~2200	~150
Electrical resistivity (Ω m)	$\sim 10^{12}$	$\sim 3 \times 10^{-3} - 4 \times 10^{-6}$
Chemical inertness	High	High

Diamonds are of great interest across many fields of science and industry owing to their outstanding properties. However, the scarcity, bulky shape, and high cost of natural diamonds limit their extensive usage. At present, several methods are used to synthesize diamonds. Synthetic diamonds can differ significantly from their natural counterparts, as their properties can be tuned by adding impurities, dopants, and other extended defects. Diamond growth through chemical vapor deposition (CVD) has been a major driver in the diamond industry since its rapid development in the 1980's and 1990's. This method has enabled the deposition of diamond on diamond and a range of non-diamond substrates (mostly in the form of thin films). The next section will discuss the various diamond synthesis techniques.

2.2 Diamond synthesis

This section focuses on the existing techniques by which diamond can be synthesized. These include the high-pressure-high-temperature (HPHT), detonation nanodiamond (DND) and chemical vapor deposition (CVD) methods. Special attention is paid to the CVD method, as this allows the deposition of diamond films on non-diamond substrates. The key features of the low-pressure CVD methods, diamond growth (homo- and heteroepitaxial), and substrate compatibility are summarized. A classification of the types of diamond films and their use in various applications will also be discussed.

2.2.1 High-Pressure-High-Temperature (HPHT)

The HPHT method aims to recreate the thermodynamic conditions under which natural diamonds are formed. In this method, graphite is placed in a hydraulic press in which it is subjected to extremely high pressure (14-17 GPa) and temperature conditions (≥ 3000 K). The addition of a metallic catalyst (Fe, Ni, Co and their alloys) can lower the pressure and temperature conditions at which the conversion of graphite into diamond occurs [17]. The HPHT and catalytic HPHT growth conditions are within the region at which diamond is the stable phase of carbon, as shown in Figure 2.4. With the HPHT technique, single-crystal diamonds with high purity, typically in sizes ranging from nanometers to a few millimeters, can be produced. HPHT-grown diamonds are subsequently used for homoepitaxial diamond growth using CVD methods.

2.2.2 Detonation nanodiamond (DND)

With this method, as its name implies, nanoparticles of diamond are obtained through detonation. In this process, an explosive mixture of trinitrotoluene (TNT) and hexogen (RDX) is detonated in the absence of oxygen. The explosion is usually carried out in a closed stainless steel chamber. Immediately after the explosion, the detonation soot consisting of diamond nanoparticles is cooled off rapidly, as the diamond yield strongly depends on the cooling rate. The final step consists of the removal of impurities originating from the stainless steel chamber and the nondiamond material. One method to extract diamond particles from the detonation soot is through boiling in acid. After synthesis and purification, the diamond nanoparticles have an average crystallite size of ~4 nm. These particles are used for seeding on non-diamond substrates to promote heteroepitaxial diamond growth. The DND growth conditions are marked as the shock wave synthesis in Figure 2.4.

2.2.3 Chemical Vapor Deposition (CVD)

Chemical vapor deposition (CVD) methods are widely used for the synthesis of diamond at reduced pressure conditions (<< 1 bar). This technique involves the deposition of carbon atoms, which originate from a carbon precursor, onto a heated substrate surface. In general, CVD setups consist of a feed system containing the vapor precursors, a deposition chamber, and an effluent gas treatment system. In the deposition chamber, diamond growth occurs through a series of steps:
(1) The activation of the inserted precursors, (2) chemical reactions between the activated species, (3) transport of the activated species to the substrate, (4) reactions on the substrate, (5) diamond growth and film formation on the substrate, and (6) transport of the byproducts.

For diamond growth, typically a mixture of carbon-containing source (usually methane) and excessive hydrogen is fed into the chamber. This mixture is then activated either thermally (e.g., by a hot-filament) or through a plasma (microwave, radio-frequency, DC discharge, plasma jet). Despite the fact that these CVD methods differ in the way the precursors are activated, they still share some common features. These include the growth in the presence of excessive atomic hydrogen, the dissociation of carbon-containing source gases, and substrate temperatures in the range of 700 °C - 1000 °C.

2.2.3.1 Role of hydrogen

Atomic hydrogen (H), which is generated from molecular hydrogen (H_2) through activation, is the secret behind low-pressure diamond growth. Atomic H performs a number of key functions in the CVD process [1]:

- H atoms react with the carbon precursor (typically CH_4) to create reactive radicals (e.g., CH_3). These radicals then diffuse and attach to suitable sites on the substrate surface, and carbon gets incorporated into the growing diamond material.
- H atoms create reactive surface sites for carbon addition. Carbon atoms are added one by one to the existing diamond lattice. Initially, H atoms are adsorbed on the surface sites in order to terminate the so-called dangling bonds. Subsequently, these surface H atoms are abstracted by other H atoms, resulting in H_2 and creating reactive surface sites that are accessible to carbon. This is repeated until surface H atoms are replaced by carbon radicals.
- H atoms etch sp^2-bonded graphite at a faster rate than sp^3 carbon. This suppresses the formation of graphitic clusters on the surface, while diamond clusters remain.
- H atoms react with long-chained hydrocarbons, splitting them into smaller pieces. This prevents the buildup of polymers, which ultimately obstructs diamond growth.
- H atoms act as carriers of heat from the filament to the substrate surface. The formation of H atoms is endothermic, while the recombination of H atoms to form molecular hydrogen on the substrate level is exothermic.

2.2.3.2 Hot-Filament CVD

A widely used technique to grow diamond films at low pressure is hot-filament chemical vapor deposition (HF-CVD). A schematic representation of a HF-CVD setup is given in Figure 2.5a. In the HF-CVD setup, atomic H is generated by the thermal decomposition of H_2 (i.e., dissociation) on the hot-filament surface (see Figure 2.5b). Refractory metals, including tungsten (W), tantalum (Ta), and rhenium (Re), are typically used as filament materials [18]. These filaments are heated electrically in the range of 2000 °C - 2300 °C using a DC power supply. The substrate is heated through the radiation of the hot-filament or by a separate heating source. The advantages of the HF-CVD method are that diamond films can be deposited over large areas and on complex geometrically-shaped substrates. Other advantages include its relatively simple design and low equipment costs, and ease of scalability. The deposition area can be scaled up by increasing the filament length and by adding more filaments to the precursor activation zone. Homogeneous diamond films can be obtained using the HF-CVD method. However, the average deposition rate (approx. 1µm/h) and film quality are considerably lower in comparison to other CVD methods. The low deposition rate is due to the upper limit of the filament temperature producing relatively less atomic H. The impurities incorporated in the diamond film are due to filament evaporation.

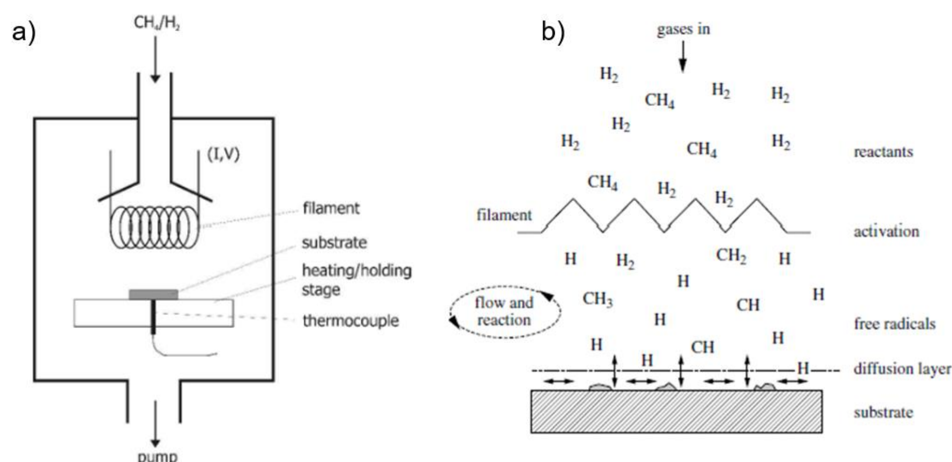

Figure 2.5: a) Schematic representation HF-CVD setup and b) physical and chemical processes during HF-CVD process [1]

2.2.3.3 Plasma-Enhanced CVD

Another widely used technique to grow diamond films at low pressure conditions is plasma-enhanced chemical vapor deposition (PECVD). In PECVD, thin films of diamond can be deposited at much lower temperatures than in HF-CVD. A plasma, which is a mixture of partially or fully ionized gases, contains free electrons that will accelerate and gain kinetic energy when an electric field is applied. These energetic electrons collide with the gas molecules and form reactive species by either ejecting or accepting an electron. Electron collisions cause H_2 to decompose into atomic H and activate hydrocarbon radicals, promoting diamond growth. Frequently used methods to generate plasma include microwave (MW), radio-frequency (RF), direct current (DC), and arc plasma jet. In most MWCVD reactor designs (see Figure 2.6), a ball-shaped plasma, which is confined in the center of the chamber, is generated from a gas discharge using microwaves (~2.45 GHz). The advantages of MWCVD are the high growth rates (≥ 10μm/h) and the ability to grow highly pure diamond [2]. The main disadvantage is that only small substrate areas can be covered with uniform diamond films due to the ball-shaped plasma. A more widespread plasma can be generated by introducing the source gases between two parallel electrodes operating either in the radio-frequency (RF) or direct current (DC) mode, or by using linear antenna MW designs [19].

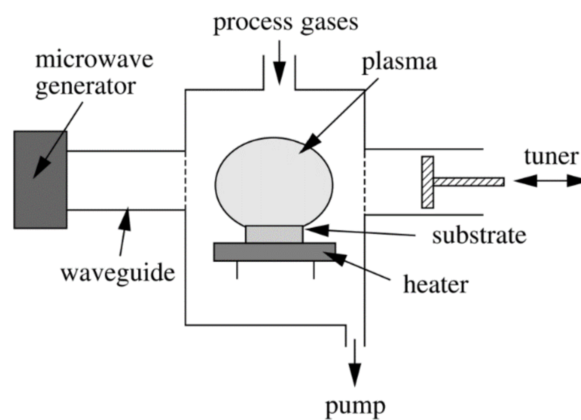

Figure 2.6: Schematic of MWCVD setup [1]

Diamond can also be grown at atmospheric pressure using combustion flames from the acetylene torch. Acetylene and oxygen are supplied to the torch in order to generate the combustion flame. The substrate is placed in the plasma-like intermediate region of the flame. Although this method is simpler and cheaper than the previously discussed methods, its use is still limited. Only relatively small areas can be covered with diamond films, and radial inhomogeneities are present in the grown diamond layers due to changing chemistry determined by the flame geometry.

The advantages and disadvantages of the previously discussed low-pressure CVD methods are summarized in Table 2.2. Energy sources can be combined in order to enhance diamond growth. This is referred to as a hybrid system. For instance, a hybrid HF-CVD technique was developed in which a DC plasma is induced by applying a potential to the filament and substrate [20].

Table 2.2: Advantages and disadvantages of low-pressure diamond synthesis methods [2, 21]

Method	Advantages	Disadvantages
Hot filament	Relatively simple setup Growth homogeneity (large/complex shaped (3D) substrates) Low-equipment cost Scalable (up to m^2 growth area)	Filament non-stability Impurities (filament evaporation) Low growth rates (1µm/h)
Microwave	High growth rates (≥ 10µm/h) High diamond quality Easy temperature control	3D-deposition difficult Inhomogeneous diamond deposition
RF & DC discharge	Large deposition area Simple setup	Impurities (electrode erosion) Sputtering (RF mode)
DC plasma jet	High growth rates (up to ~1mm/h)	Substrate cooling required High power and gas consumption High equipment cost
Combustion flame	Low equipment cost Simple setup	High gas consumption Radial film inhomogeneities

2.2.4 Process parameters

The properties of synthetic diamond films are largely defined by the following main process parameters [21]:

- Carbon-to-hydrogen ratio (typically CH_4 (0.5 vol.% - 2 vol.%) / H_2): An increase in methane concentration results in higher growth rates, but at the same time, the defect density in the diamond crystals increases, resulting in lower quality diamond due to the increased sp^2 content.
- System pressure (<<1 bar): The formation of atomic H from H_2 is favored at low pressure conditions. Typically, diamond CVD is performed at a system pressure of 5-100 mbar.
- Substrate temperature (700 °C - 1000 °C): At high substrate temperatures (>1000 °C), the grown diamond converts into graphite, whereas temperatures below 600 °C suppress the diamond deposition rate significantly. A substrate temperature of ~800 °C is considered optimal for diamond growth, as recombination of atomic H into H_2 is prevented at the substrate surface.

2.2.5 Substrate for diamond growth

Diamond growth can be subdivided into homoepitaxial and heteroepitaxial. Homoepitaxial growth occurs on diamond substrates and results in single-crystalline diamond films, whereas heteroepitaxial growth, where diamond is grown on non-diamond substrates, produces polycrystalline diamond films. In the latter, only a small selection of materials are compatible with diamond growth. For successful diamond deposition, the substrate must meet the following requirements [22]:

- Melting point: The substrate should be able to withstand the deposition temperature (~800 °C) without undergoing a phase transformation (e.g., melt or vaporize). Materials with low melting points, such as polymers, glass, and aluminum are not suitable substrate materials.
- Thermal expansion: The substrate will expand during the initiation of the diamond synthesis process as a result of the high temperatures, and after deposition, the substrate is cooled off and will experience contraction. The thermal expansion coefficient of the substrate material should be close to that of diamond. Large differences in the thermal expansion coefficient will induce (compressive) shear stresses at the substrate-to-film interface, which can lead to cracking or even detachment of the deposited diamond film.
- Reactivity: The attachment of the diamond film to the substrate surface, also known as adhesion, is very important. A strong bonding between the diamond film and the substrate surface is preferred. The substrate can react and form a thin carbide interlayer on which diamond can grow. The latter depends on the reactivity of the material of choice. The substrates can be categorized into three classes based on their reactivity [1]:
    1. Substrates with little or no carbon solubility: no carbide formation includes materials such as copper, silver, gold, diamond, and graphite.
    2. Substrates with mutual solubility: carbon dissolves in the substrate material includes materials such as platinum, palladium, rhenium, and nickel.
    3. Carbide compounds are readily formed on materials such as titanium, tantalum, tungsten, molybdenum, and silicon.

Spontaneous diamond growth on non-diamond substrates is extremely difficult due to the large surface energy difference. To stimulate diamond growth, a pre-treatment of the substrate is usually required, through which additional nucleation sites are formed on the substrate surface. These sites act as the basic building blocks for crystals to grow out of. Potential substrate materials and various substrate treatments for diamond epitaxy are summarized by Liu & Dandy [23]. A simple and more effective approach to realize continuous film growth is through spin-seeding with nanodiamond particles [24]. This method relies on the deposition of diamond nanoparticles, e.g., obtained from the DND-method as discussed in Section 2.2.2, by which homogenous seed layers with high seed density (up to 5×10^{10} cm^{-2}) can be obtained. These nanodiamonds act as nuclei from which diamond crystals can evolve. Depending on the growth conditions, various polycrystalline diamond films with different microstructures and surface morphologies can be produced, which will be discussed next.

2.2.6 Polycrystalline diamond films

Synthetic diamond can be subdivided into single-crystal and polycrystalline diamonds. In a single-crystal diamond (SCD), the crystal lattice is continuous and the atomic structure is periodic across its entire volume. Polycrystalline diamond (PCD) is comprised of many individual grains (crystallites) with different sizes and orientations, separated by grain boundaries. The diamond grains are solely composed of sp^3 hybridized carbon atoms, while the grain boundaries consist of sp^3 and sp^2-bonded carbon. The previously discussed CVD methods (see Section 2.2.3) enable the growth of SCD and PCD films. The growth conditions and time determine the surface morphology and film thickness. PCD films can have different microstructures, and depending on the growth time, different film thicknesses (ranging from fractions of a micrometer to a few millimeters) can be obtained.

Three different microstructures are usually distinguished based on the average grain size: microcrystalline diamond (MCD – grain size > 1 µm), nanocrystalline diamond (NCD – grain sizes between about 10 and few 100s nm), and ultra-nanocrystalline diamond (UNCD – grain sizes varying in the narrow range of 3 - 6 nm) [3]. The properties of PCD films strongly depend on their microstructure. Starting from randomly oriented nuclei, the diamond crystals can grow in a random (secondary nucleation) or preferred (textured growth) orientation as the film thickness increases. MCD films are typically synthesized in a mixture of H_2 (99%) / CH_4 (1%) [3]. As the growth proceeds, the film thickness increases, and a columnar structure is formed, as shown in Figure 2.7.

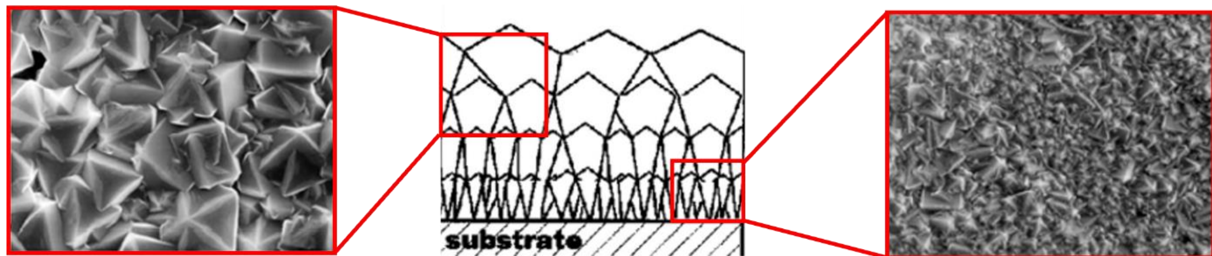

Figure 2.7: Schematic representation of columnar structure (middle) and corresponding surface morphologies of MCD films at layer thicknesses of 15 µm (left) and 5 µm (right) [2]

The grain size scales with the film thickness, resulting in high surface roughness determined by the surface facets. Depending on their application, these films usually require some surface treatment, e.g., polishing, to reduce the surface roughness. On the other hand, NCD films are grown in methane-rich gas mixtures of typically H_2 (100-x vol.%) / CH_4 (x vol.%), with x varying between 2 and 5. The growth process comprises low to moderate re-nucleation, which has a limiting effect on the average grain size as new crystallites evolve. The grain sizes of UNCD films are grown in a different gas mixture consisting of Ar (99%) / CH_4 (1%). The grain sizes are independent of the film thickness due to the continuous re-nucleation by which nanometer-sized grains are obtained. UNCD films have a very smooth surface. A decrease in grain size results in an increase in the surface smoothness of PCD films. However, a decrease in grain size increases the number of grain boundaries, thus raising the sp^2 content in the diamond films.

The properties of diamond films can be tuned further by adding impurities and dopants to the crystal structure. Of particular interest is the synthesis of electrically conductive diamond by introducing boron dopants into the precursor gas mixture. As-produced material is referred to as boron-doped diamond (BDD) films. In the BDD crystal lattice, some of the carbon atoms are substituted by boron atoms. The boron concentration determines the conductivity of the diamond film.

The growth conditions have immediate implications on the properties of the film. Depending on the application of interest, growth conditions can be adjusted accordingly to obtain the required film properties. Various applications of CVD diamond films will be discussed in the next section.

2.2.7 Applications

Diamond possesses excellent properties that enable its use in a wide range of applications. The deposition of diamond films by CVD methods has increased the applicability of diamond even further. Diamond is finding its way into many fields. This section gives a brief overview of the current and potential applications of CVD films. CVD diamond films are ideal candidates for coatings on wear parts, heat-spreaders, and optical windows [2]. Cutting and milling tools can benefit from the high hardness and wear resistance of (polycrystalline) diamond films deposited on the tool surface [4]. The tool, which can be considered as the substrate, is usually made of cemented tungsten carbide (WC-Co), owing to its high fracture toughness [5]. At present, diamond-coated tools, including drill bits, core bits, blades, and saws, are commercially available (see Figure 2.8) [25]. Diamond-coated tools have a longer lifetime and provide a better surface finish than uncoated cutting tools. The high thermal conductivity, low thermal expansion coefficient, and large electrical resistivity make diamonds very suitable heat spreaders, particularly in high-power electronic devices [6]. Damages due to overheating of these devices can be prevented by coating the concentrated source with diamond films [22]. For this use, only high-quality PCD films are desired since grain boundaries and impurities significantly reduce heat conduction. The wide optical transparency in combination with other remarkable properties, makes diamond an ideal material for optical windows. As transparency is related to the diamond quality, defects and impurities need to be minimized in order to grow optical-grade single-crystal CVD or polycrystalline diamond [6]. Diamond is known to be biocompatible, which therefore expands its potential use to in vivo applications, e.g., diamond-coated biomedical implants and electrodes for deep brain stimulation [7, 26]. In the field of electrochemistry, electrically conductive diamond (BDD) is showing great potential for many uses, e.g. biosensors and wastewater treatment. Diamond biosensors can be used for health monitoring, and large-sized diamond electrodes show great potential for water purification.

Figure 2.8: Diamond products: diamond cutting blade (left), diamond drill bit (middle) and optical grade PCD (right) [6, 25]

Despite the various application examples listed above, the full potential of CVD diamond films has not yet been explored, as several challenges, such as the growth of large-area, single-crystal diamond, the high substrate temperature, and viable n-type doping, have to be overcome first. Some of these challenges are currently being investigated at TU Delft. Recently, a new home-built HF-CVD reactor has been added to the deposition lab, which should enable the deposition of uniform diamond films on large-area (~5 cm in diameter) substrates. The new reactor setup and its associated challenges, particularly the non-stability of metallic filament and mechanical clamping during diamond CVD, will be discussed next.

2.3 Filament characteristics

A frequent problem of the HF-CVD method is the premature failure of the metallic filaments. The heated filaments undergo phase changes and large deformations when exposed to a carbon-containing atmosphere. This section provides an overview of the filament behavior during the diamond deposition process and outlines existing clamping mechanisms that may prevent the early breakage of the filaments.

2.3.1 Filament properties

Not all materials are suitable for use as filament. A filament is required to operate at high temperatures in order to activate the precursor gases, which makes refractory metals ideal candidates. Among the refractory metals, tungsten (W) and tantalum (Ta) are widely used as filaments owing to their high melting points and widespread availability [18, 27–36]. Some HF-CVD systems employ rhenium (Re) filaments [32, 37]. However, rhenium filaments are far more expensive and less common in use as compared to W and Ta filaments and will therefore not be discussed in this review. A selection of the mechanical and physical properties of tungsten and tantalum is given in Table 2.3.

Table 2.3: Properties of Ta and W at room temperature conditions (T = 298K, p = 1atm) [38, 39]

Metal	**Melting point (°C)**	**Electrical resistivity (Ω m)**	**Vickers hardness (kg/mm²)**	**Elastic modulus (GPa)**	**Yield strength (MPa)**
Ta	2996	1.25×10^{-7}	100	186	185
W	3410	5.65×10^{-8}	400	400	750

Despite the remarkable properties of these refractory metals, their characteristics do change over time when used as filaments in the CVD synthesis of diamond films. The reason for this is that metallic filaments interact with the carbon present in the gas mixture at high operating temperatures.

2.3.2 Carburization process in detail

The incorporation of carbon into the metal lattice is called carburization. W and Ta filaments react with carbon to form metal carbides. During the carburization process, the filaments undergo physical and chemical changes, and, as a result, the material properties change accordingly. The carburization of these filaments proceeds according to the following sequence of steps [40]:

1. Transport of CH_4 molecules to the filament surface, where they are physically adsorbed;
2. Decomposition of CH_4 molecules on the heated filament surface where the resulting products (H, H_2, and CH_x) are chemisorbed;
3. Release of the gaseous species mentioned in the previous step;
4. Transformation of the surface adsorbed carbon atoms into the dissolved state;
5. Diffusion of carbon atoms into the metal lattice to form sub- and monocarbides.

Several studies have been conducted on the carburization of W and Ta filaments during the diamond deposition process. The outcomes of these studies are summarized in Table 8.1 and Table 8.2 (see Appendix A. Literature review (part II)), respectively.

2.3.3 Filament behavior

W and Ta filaments undergo multiple phase changes during the carburization process. The carburization of the filaments is a dynamic process in which chemical changes are accompanied by physical changes. The findings from the literature do provide consistent information regarding filament carburization over time. The carburization process can be characterized by changes in filament composition, structure, electrical resistivity, and mechanical properties. This section provides a detailed description of the behavior of W filaments during the diamond deposition process and its effect on diamond growth. The literature results on the carburization of Ta filaments have been included in the Appendix A1. Tantalum filaments.

2.3.3.1 Tungsten filaments

Phase change

The carburization of W filaments is a two-step process. First, W is transformed into tungsten sub-carbide (W_2C), after which W_2C is converted into tungsten carbide (WC). The metallographic cross-sections of a partially carburized W filament (99.8% purity) are shown in Figure 2.9. The authors of [31, 34] have demonstrated that the first conversion is completed relatively fast (about 1 hour), while the second conversion was not completed even after 40 hours of carburization. The carburization of W filaments proceeds according to the following sequence:

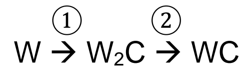

The carburization rate increases with increasing the methane concentration in the gas mixture and rising the filament temperature. This dependency can be explained by Fick's first law of diffusion:

$$J = - D \frac{dC}{dx} \qquad \text{(Eq.2.1)}$$

where J ($mol\ m^{-2} s^{-1}$) is the diffusion flux, D ($m^2\ s^{-1}$) is the diffusion coefficient, C ($mol\ m^{-3}$) is the concentration and x (m) is the distance into the material of diffusion. The flux J measures the moles of a substance that will flow through a unit area per unit time. The diffusion rate can be determined by multiplying J with the surface area of diffusion. In this case, Fick's law states that the diffusion rate is proportional to both the surface area of the filament and the difference in carbon concentration (in the gas mixture vs. in the filament) and is inversely proportional to the thickness of the filament. The diffusion coefficient (D) is dependent upon temperature T (K) and follows from:

$$D = D_0\, e^{\left(\frac{-Q}{RT}\right)} \qquad \text{(Eq.2.2)}$$

where D_0 ($m^2\ s^{-1}$) is the maximum diffusion coefficient, Q ($J\ mol^{-1}$) is the activation energy for diffusion, and R (8.31446 $J\ mol^{-1} K^{-1}$) is the ideal gas constant. Increasing the filament temperature results in an increase in D and, consequently, the diffusion rate. The carburization rate decreases with increasing gas pressure [10].

.

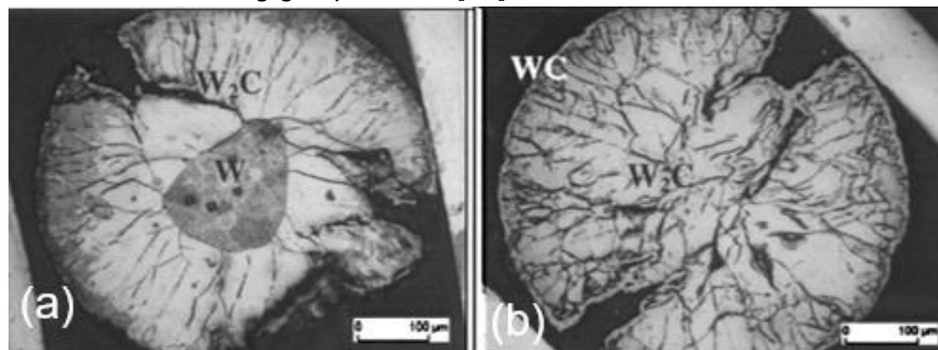

Figure 2.9: Optical micrographs of technically pure W filaments (99.8% purity) when carburized for a) 60 minutes and b) 70 minutes [10]

Carburization kinetics

The carburization kinetics of W filaments have been examined. There are two rate-determining steps during the carburization process (see Figure 2.10). The formation of W_2C is surface-controlled, and the dissociation of methane is the corresponding rate-determining step. This reaction is characterized by the formation of a W_2C layer, which increases in thickness over time. The growth of the W_2C layer starts from the surface of the filament and continues radially inward as long as W is present in the core (Figure 2.9a). The formation of the W_2C layer is rather fast since the filament absorbs a significant amount of the available carbon in the gas mixture. The reason for this is that the diffusion rate of carbon into the W filament is higher than the dissociation rate of CH_4 (the slowest step), which leads to depletion of the carbon in the gas mixture and subsequently to unsteady diamond growth conditions [29, 31, 34]. After the W_2C formation is completed, a WC shell is formed on the perimeter (Figure 2.9), and its growth proceeds in a similar way as described for the W_2C layer. When the WC layer becomes thick enough, the rate-determining step changes to the diffusion of carbon through the carbide layer, as it becomes more difficult for the carbon atoms to diffuse through the expanding WC layer to reach the WC - W_2C interface. This reaction is slow, and over time, more carbon atoms accumulate on the surface. This may ultimately lead to a decrease in gas activation as the carbon atoms could occupy the surface sites available for hydrogen dissociation.

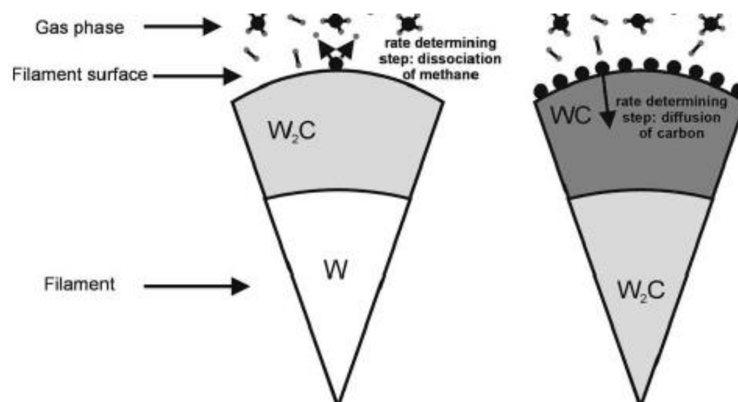

Figure 2.10: The rate determining steps during carburization of tungsten filaments [34]

Filament poisoning

When the carbon concentration on the filament surface reaches its saturation value, e.g., if the incoming flux of carbon atoms is higher than the outgoing (diffusion) flux, solid carbon is deposited on the surface [27, 41]. This ultimately results in the formation of a graphite layer, which covers the entire filament surface, as illustrated in Figure 2.11. This phenomenon is called filament poisoning and inhibits the filament from activating the chemical precursors in the gas mixture [29]. The diffusion rate of carbon into the (partially) carburized W filament and the thickness of the graphite layer are the parameters that control the formation of the graphite layer. Filament poisoning is more likely to occur during the second conversion step (W_2C → WC) owing to the higher carbon concentration on the filament surface [31]. Previous studies have revealed that poisoning of carburized W filaments occurred at relatively low filament temperatures (≤1900 °C) or high CH_4 concentrations (>1 vol%) [27, 29, 31]. Sommer and Smith also found that a poisoned filament can regain its activity by increasing the filament temperature (1900 °C → 2200 °C). This led to the etching of the deposited graphite and to a partial decarburization of the filament [29].

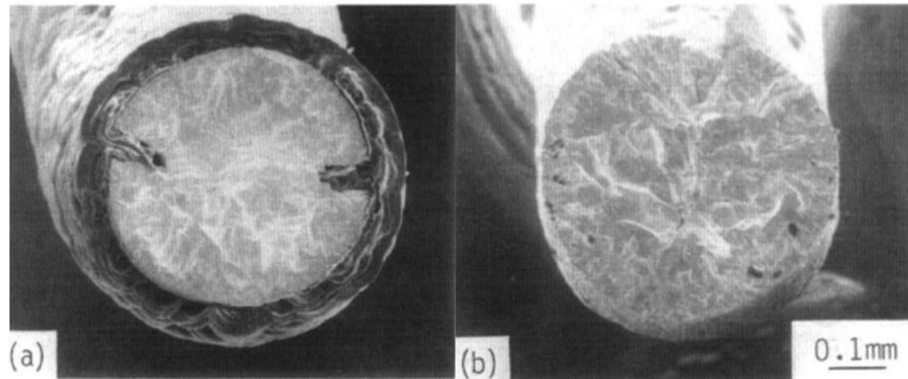

Figure 2.11: Cross-sectional structure of the filament heated at a) 1900 °C (poisoned) and b) 2150 °C in 1.6 vol.% CH_4 for 7 hours [31]

Volume expansion and crack formation

During the carburization process, a dense network of irregular microcracks formed along the length of the filament (Figure 2.9). A total volume increase in the range of 8.8% - 22.5% is reported for carburized W filaments [30, 34]. The volume expansion is induced by the incorporation of carbon atoms into the metal lattice [28]. However, during the conversion steps, internal stresses developed in the filament due to the different densities (see Table 2.4) of the different phases [42]. Compressive stresses are established in the carbide at the W - W_2C interface, while on the surface level, the carbide layer is under hoop tension. As the carburization process proceeded further, the stresses increased, and when the outer tensile stresses exceeded the tensile strength of the carbide phase, cracks were induced. These cracks resulted in the embrittlement of the filaments, and even small mechanical disturbances could lead to the breakage of the filaments.

Electrical resistance

The carburization of the W filaments has a significant influence on their electrical resistance. The filaments are resistively heated to a desired temperature by electrical power. Typically, the carburization process is monitored by tracking the changes in filament resistance (or voltage) over time [27, 30, 33, 34]. This is done when a steady electrical current is applied. The resistance curves of the various studies showed a similar response. At first, the electrical resistance showed an increase with increasing filament temperature. In the second stage, a steep increase in resistance is noticed, which indicates that the first conversion of W into W_2C is taking place. In the third stage, a notable stagnation of the resistance is noticed, and a near-steady resistance value is reached. Typically, the latter indicates that the first conversion (W → W_2C) is completed [27, 29]. In the last stage, a slight decline in electrical resistance is noticed, which indicates that the second conversion of W_2C into WC is taking place. This electrical resistance behavior is consistent with the specific resistances of the different W phases (see
Table 2.4). However, this behavior is only valid when the central parts of the filament are considered. In cases where the electrical resistance (or voltage) of the entire filament is measured, the stagnation and decrease in resistance occur at a later stage than expected [33, 34]. The reason for this is that the carburization of the entire filament is not uniform. The temperature of the filament near the clamping is lower than in the central parts, and therefore the carburization at the filament ends occurred at a slower rate.

Table 2.4: Density and specific resistance of different tungsten phases at 25°C and 2200 °C [30, 34]

Phase	Density (g/cm^3)	Specific resistance at 25 °C (µΩ cm)	Specific resistance at 2200 °C (µΩ cm)
W	19.3	5.28	75
W_2C	17.23	80	125
WC	15.67	25	-

Pure vs. doped (non-sag) tungsten

The carburization of commercially pure and doped tungsten filaments was investigated [34]. The commercially pure W filament had a purity of 99.8% and consisted of the following trace elements: K (<10 ppm); Si (<30 ppm); Al (10 ppm); O (<800 ppm); and Mo (<50 ppm). The same purity was used for the doped W wire, whose composition included: K (<80 ppm); Si (<160 ppm); Al (<33 ppm); and Mo (<50 ppm). The grain size of the pure tungsten wire increased drastically right after initiating the carburization process, while doped tungsten showed no increase in grain size for the metallic phase. Both filaments showed crack formation over time. When the second conversion was initiated, several irregular cracks were observed in pure W (see Figure 2.9), while doped W showed mainly a single crack along the filament axis leading to a "Pac-Man" like overall shape (see Figure 2.12). The formation of WC occurred at a faster rate in pure W than in doped W. The reason for this is that the diffusion paths for carbon in pure tungsten are shorter due to the dense network of cracks [34].

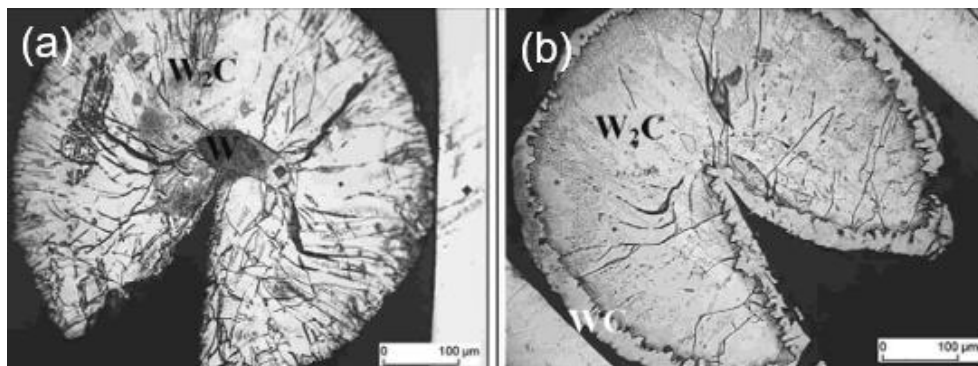

Figure 2.12: Optical micrographs of doped W filaments (99.8% purity) when carburized for a) 50 min and b) 360 min [34]

Doped tungsten is also referred to as non-sag tungsten. When used as filaments in light bulbs at service temperatures in the range of 2500 °C – 3000 °C, pure W wires failed rapidly as a result of grain boundary sliding, while doped W wires lasted considerably longer owing to their interlocking long-grained microstructures, which prevented grain boundary sliding and diffusional creep. The addition of potassium (K) increases the shape stability (i.e., resistance to deformation under its own weight) of doped W significantly as compared to commercially pure W. This potassium enables the formation of rows of smaller potassium bubbles during the wire fabrication and consequently the formation of the long-grained interlocking microstructures during filament operation, which is the key to the non-sag properties of doped W wires [43]. This makes doped W wires significantly more creep-resistant than pure tungsten wires.

2.3.3.2 Filament condition and its effects on diamond growth

Well-faceted diamond films with comparable growth rates can be grown using both W and Ta filaments. The effect of the filament material on HF-CVD diamond growth has been investigated and will be outlined in this subsection [29, 30, 32].

Temperature drop of the filaments

The temperature of the W and Ta filaments decreased over time. The increased area of the filaments and the formation of the different phases, which have different electrical conductivities and different thermal emissivity, are responsible for the temperature drop [30]. W filaments experienced a greater temperature drop (~200 °C) as compared to Ta filaments owing to the higher heat dissipation at the clamps [30].

During the HFCVD process, the introduced power is dissipated through convection (P_{conv}), conduction at the clamps (P_{cond}), dissociation of molecular hydrogen (P_H) and radiation (P_{rad}). It has been reported that P_{rad} and P_H are the more dominant mechanisms for heat loss [34]. The power dissipation can be denoted by the following set of equations:

$$P_{in} = P_{out} \qquad \text{(Eq. 2.3)}$$
$$P_{out} = P_{rad} + P_{conv} + P_{cond} + P_H \qquad \text{(Eq. 2.4)}$$
$$P_{rad} = \varepsilon A \sigma T^4 \qquad \text{(Eq. 2.5)}$$
$$P_H = n(T,p)\gamma(T)E_{H2/2H}A \qquad \text{(Eq. 2.6)}$$

Eq. 2.3 represents the law of conservation of energy in which the introduced electrical power P_{in} is equal to the dissipated power by the filament. The power dissipation by radiation (Eq. 2.5) is determined by the emissivity (ε), filament surface area (*A*), Stefan-Boltzmann-constant σ (5.7×10^{-8} W m^{-2} K^{-4}) and filament temperature (*T*). The power dissipation through the dissociation of molecular hydrogen is described by Eq. 2.6, in which *n(T,p)* is the number of collisions between hydrogen molecules and the filament surface per time and square unit, *γ(T)* is the probability of hydrogen dissociation, and $E_{H2/2H}$ is the bonding energy of the H_2 molecule (4.5 eV). As stated earlier, the carburization of the filaments is a dynamic process, and the contribution of each of the power dissipation mechanisms changes during the carburization of the filaments.

Filament contamination and lifetime

For W and Ta filaments, the degree of filament metal impurity content in the diamond film strongly depends on the carburization state of the filaments. Conditioned (carburized) filaments show considerably lower amounts of impurities as compared to their metal counterparts owing to the higher melting points of the metal carbides [35, 44]. The metal impurity content in diamond films when using carburized W and Ta filaments under the same deposition conditions was investigated [32]. The films grown using a carburized W filament contained only 4.6 ppm W impurity, while the films grown using a carburized Ta filament exhibited impurity levels of 37 ppm Ta.
The higher diffusion rates of carbon into the metallic filaments allow carbon to diffuse quickly into the filament, which leads to the depletion of carbon in the gas mixture and consequently low diamond growth rates when using fresh metallic filaments. Furthermore, the conversion of metal (M) into its sub-carbide (M_2C) occurs faster than the conversion of sub-carbide into carbide (MC). In general, the filaments need to be conditioned before initiating the diamond synthesis process to ensure steady deposition conditions.

A major drawback of the HFCVD method is the deformation and embrittlement of the filaments, which ultimately results in the breakage of the filaments. Particularly when heat and cooling cycles are involved, thermal stresses tend to shorten the filament's life even further. The repeated use of the same filament is of great importance, as it exempts one from conditioning the filaments for each deposition run, making the overall process more efficient.

Various solutions have been proposed in order to overcome the premature failure of the filaments. Most of these methods encourage the use of straight filaments rather than coiled filaments, as straight filaments can maintain their original shape by applying a (small) tension to the filament to take up any thermal and carburization expansion during the carburization process [35, 37]. Several clamping mechanisms have been suggested in the literature as an attempt to extend the lifespan of the filament by preventing it from breaking. A detailed description of these mechanisms can be found in the Appendix A2. Tensioning mechanisms.

3. Research focus

This chapter will highlight the scope, goal, and research questions of this MSc thesis project.

3.1 Problem statement

A new HFCVD reactor setup (2nd generation) has been designed and built at dept. PME (TU Delft) as an upgrade to the existing reactor (see Appendix B1. HF-CVD setup (1st generation)). This reactor is the scaled up version and will employ an array of straight filaments instead of a single coiled filament, which should enable the uniform deposition of diamond films (primarily BDD material) over larger substrate areas (~5 cm diameter). In this setup, the filaments are placed in a custom-made clamping device to ensure secure fixation and reliable electrical contact. However, in the current configuration, the filaments are restricted from expanding and contracting freely, resulting in residual mechanical stresses that ultimately cause premature failure of the filaments. To enable diamond growth in the new setup, a new approach is needed to extend the lifespan of the filaments.

3.2 Goal of this research

The main objective of this MSc thesis project is to enable diamond growth in the new HF-CVD setup. An experimental optimization study will be conducted for this purpose. The first crucial step is to extend the lifespan of the W filaments to enable diamond growth. Once the lifespan of the filaments is extended, the next step is to perform a growth study that investigates the effect of different deposition parameters on diamond growth in this setup. In the final stage, based on the experimental results, new designs for the clamping device will be proposed as an improvement to the existing fixation of the filaments.

3.3 Research questions

The main question of this research is:
How to mechanically constrain straight metallic tungsten filaments to ensure continuous and intermittent growth of diamond in a home-built hot-filament chemical vapor deposition reactor setup?

The sub-questions that need to be answered during the course of this project are:

- What is the average lifetime of the W filaments in the current setup under typical diamond deposition conditions?
- How can the lifespan of the W filaments be extended?
- How long do the filaments need to be carburized (i.e., conditioned) to enable diamond growth?
- How do various deposition parameters (filament-substrate distance, stage temperature, and methane concentration) affect the morphology, quality, and growth rate of synthesized diamond films in the new HF-CVD setup?
- How can the filaments be maintained in a straight position during the deposition process without compromising their lifespan?

4. Methodology

This chapter outlines the experimental setup (HF-CVD) and provides an overview of the materials, equipment, and experimental procedures used in this research.

4.1 HF-CVD setup

A schematic representation of the HF-CVD setup is given in Figure 4.1. This setup consists of a cubic-shaped reaction chamber made of stainless steel 304. The size of the chamber is 204 x 204 x 204 mm^3, and the flanges are water-cooled by the circulating fluid temperature controller (SMC – HRS). The front flange can be opened and closed, allowing the insertion and removal of samples, while the other flanges are fixed. The front and left flanges are equipped with borosilicate glass windows. The gas feed system, which consists of high-precision mass flow controllers (BROOKS Instrument), a custom pipeline network, and gas supply, enables the insertion of different gases in the chamber at a controlled rate. In its current state, methane, hydrogen, and argon gases can be inserted. However, the gas supply can be extended to include nitrogen, trimethyl borane, and other gases of interest. A vacuum pump system (Adixen ACP 15) is used to maintain the low pressure conditions required for the diamond synthesis process. Two copper electrodes are mounted on the rear flange inside the chamber, on which a custom-made clamping mechanism rests. This clamping device is used to secure the filaments, and a DC power supply provides the electrical power to the filaments. Additionally, this setup is equipped with a heated stage (Thermic Edge) on which the substrate can be placed. The actively heated stage is located in the center of the vacuum chamber and has the ability to rotate. By rotating the stage, the substrate is exposed to more evenly distributed temperatures, improving the uniformity of the diamond films. The heated stage can also be adjusted in height, allowing control of the distance between the substrate and the filament. An internal thermocouple measures the temperature of the stage, and the PID heater controller monitors and regulates the temperature. Various parameters, such as the gas flow, stage temperature, and filament power, can be precisely controlled and monitored through the associated software (NI LabView).

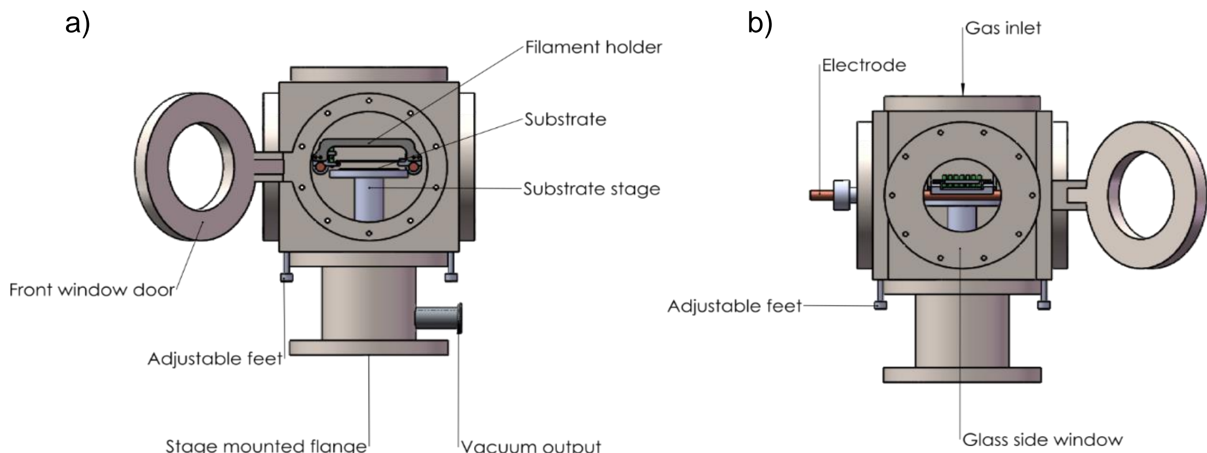

Figure 4.1. Schematic representation of the HF-CVD setup with a) front-view and b) side-view

The filaments are placed in a custom-made clamping device, as can be seen in Figure 4.2. The original clamping device consists of a pair of molybdenum electrodes, insulators, a circular guide electrode, a fixation plate, and multiple dead weights. The molybdenum electrodes make direct electrical contact with the underlying copper electrodes and are interconnected by the insulators to prevent any electrical short circuits. The circular guide electrode ensures that equal spacing is maintained between the filaments, while the dead weights exert a downward force to compensate for filament elongation, thereby aiming to keep the filaments straight.

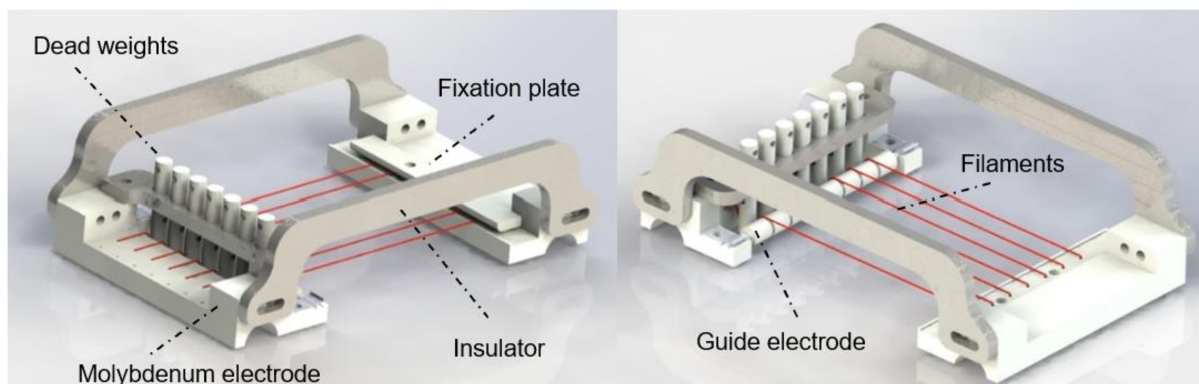

Figure 4.2. Isomeric views of the 3D model representing the original clamping device

4.2 Materials

Tungsten (W) wires with a purity of 99.95% and a diameter of 0.5 mm were used as filament material. The wire was wound around a spool in its as-delivered state (supplier Goodfellow). A side cutter, drill machine, and vise were used for the straightening of the filaments.

P-type silicon (Si) wafers with (100) crystal orientation were used as substrates. An ethanol-based dispersion (supplier Sigma Aldrich) containing nanometer-sized detonation diamond (DND) particles was used for the pre-treatment of the substrates. During the growth experiments, high-purity methane (CH_4) and hydrogen (H_2) gases were utilized as precursors for the diamond synthesis process, while argon (Ar) gas was used as the carrier gas during the chamber evacuation process.

The designs of the conceptualized clamping devices were 3D-printed using the Prusa i3 MK3 printer. The printed parts were made of PLA and Prusament resin.

4.3 Filament carburization experiments

Throughout this research, several experiments were conducted. The first part was mainly focused on the filament carburization experiments. Each carburization experiment was initiated by inserting the clamping device, including the filament, into the deposition chamber and subsequently evacuating the chamber. The filaments were resistively heated to the desired temperatures (2100 °C – 2200 °C) in an environment consisting of x vol.% CH_4 and 100-x vol.% H_2, with a total gas flow of 303 standard cubic centimeters per minute (sccm) at a deposition pressure ranging from 10.8 mbar to 12.5 mbar. For a single W filament, a steady electrical current of 23 A was applied. To minimize the risk of excessive thermal stresses, which negatively affect the lifespan of the filament, the electrical current was gradually increased from 0 A to 23 A at a rate of 0.1 A/s. An electrical current of 23 A was sufficient to initiate the carburization process at an acceptable rate. After several operating hours, the CVD process was interrupted by turning off the W filament. The electrical current was gradually reduced from 23 A to 0 A at a rate of 0.1 A/s. Once the electrical current reached 0 A, the filament was allowed to cool down for several minutes.

The carburization process was monitored by tracking the changes in voltage and electrical power at 15-minute intervals. Additionally, the pressure, gas flow, and current were also monitored throughout this process.

4.4 Pyrometer

The filament temperature was measured using an optical pyrometer (PYRO MicroTherm) equipped with a lens (lens code C). To measure temperatures above 1900 °C, the pyrometer was set to temperature range mode #3. By adjusting the rheostat, the intensity of the in-view instrument filament could be adjusted to match the intensity of the target (hot-filament). The temperature is measured correctly when the intensity of the light radiated from the target cannot be distinguished from the intensity of the light radiated from the in-view instrument filament, as demonstrated in Figure 4.3. The digital display electronic unit allows users to read the measured target temperature. Additionally, this unit also enables users to insert an emissivity value to display an emissivity-corrected temperature (T_e). After the W filaments reached near-constant power consumption, the emissivity value was set to 0.85 [33]. This value was selected based on the emissivity values found in the literature for carburized filaments, enabling us to determine the emissivity-corrected temperature.

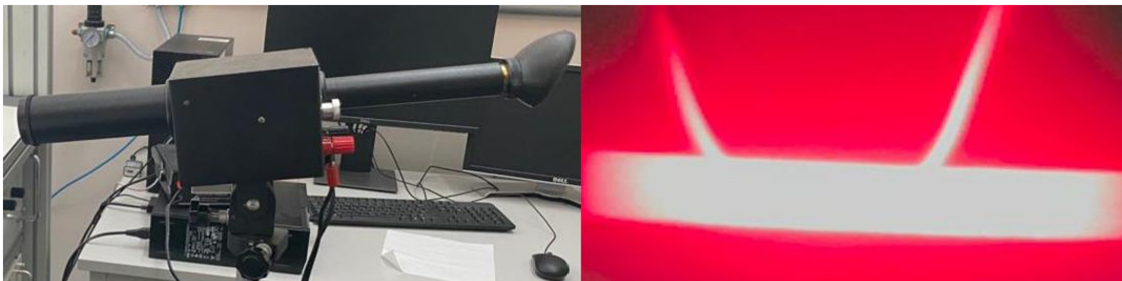

Figure 4.3: Pyrometer (left) and an optical image (right) of the in-view filament (U-shape) intensity matched with the target (hot-filament)

4.5 Seeding

The spin-coating machine (POLOS 200) was used for the pre-treatment of the substrates. Prior to coating, the 2” Si wafers were cut into smaller 10 x 10 mm-sized wafers and cleaned using sonification. The spin-seeding approach with nanodiamond (ND) particles was implemented for the pre-treatment of the substrates due to its simplicity and effectiveness [24]. After the sonification process, the diced wafers were individually placed on the chuck of the spin-coating machine. Figure 4.4 illustrates the steps involved in the spin-seeding process. Initially, when the chuck was stationary, the ND dispersion was carefully pipetted onto the substrate surface. Three droplets of the solution were applied to ensure complete coverage of the substrate surface with the seeding solution. Next, the spin-coating was started, and during the spin-up process, another three droplets of the seeding solution were applied. Next in the process was the rinsing step, where the wafer rotated at 1500 rpm while being periodically (i.e., 3 times in total, each with a duration of 3 seconds) sprayed with 99.9% pure ethanol. This step was crucial to remove the excessive seeding from the substrate surface and minimize the agglomeration of the ND particles. Finally, the wafer is spin-dried and stored in a Petri dish.

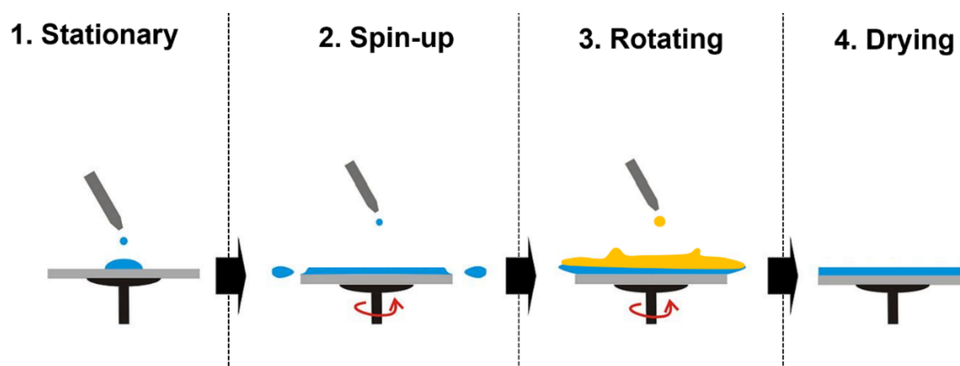

Figure 4.4: Overview of the steps involved in the spin-seeding process. The ND solution is indicated in blue and pure ethanol in yellow.

4.6 Diamond film growth experiments

After sample preparation, the next step involved the growth of diamond films. The diamond growth experiments were conducted using a single partially carburized W filament. After evacuation of the chamber, H_2 and CH_4 gases were introduced with a total mass flow rate of 303 sccm. The filament temperature and deposition time were kept constant at 2180 ± 20 °C and 7.5 h, respectively. During the growth process, the deposition parameters (i.e., pressure, gas flow, filament voltage and temperature, stage temperature, etc.) were monitored.

4.7 Scanning electron microscopy

Scanning electron microscopy (SEM) measurements were performed using the JEOL JSM-6500F and JEOL JSM-6010LA scanning electron microscopes. The pre-treated substrates were analyzed using the JEOL JSM 6500F in a secondary electrode imaging mode operated at 5 kV and a magnification of 45000x to observe the distribution of the nano-sized diamond particles on the substrate surface. The diamond-coated substrates were characterized using the JEOL JSM-6010LA scanning electron microscope. The top and cross-sectional views were examined to visualize the surface morphology and thickness of the diamond films at an accelerating voltage of 10 kV and 15 kV, respectively. These SEM analyses are performed over a range of magnifications (10000x – 30000x). The measurement tool available in the associated software (In Touch Scope) was used for the analysis of the SEM images. The average grain size for each sample was determined using four different SEM images (top view), and on each SEM image, 25 randomly selected grains were measured. The average thickness was based on 10 measurements from different SEM images (cross-section).

4.8 Raman spectroscopy

The quality of the diamond films was assessed using Raman spectroscopy (Horiba LabRAM HR). This setup is equipped with a solid-state laser operating at an excitation wavelength of 514 nm. The measurements were taken at multiple locations on each diamond-coated sample to determine the variations in sp^3 and sp^2 contents. Raman spectroscopy was performed using an objective with a magnification of x50 and a 100% ND filter. The Raman spectra were investigated in the spectral range of 800 cm^{-1} to 2000 cm^{-1} and normalized to a range of 0 to 1 for better comparison of the data and to evaluate the ratio between sp^3 and sp^2 content.

4.9 Software

The HF-CVD setup was controlled using the NI LabView software, as described earlier.
Microsoft Excel, MATLAB and Origin Pro were used to process the measurement data. The designs of the conceptualized clamping devices were generated using SolidWorks.

5. Results and discussion

This chapter consists of three sequential subsections, which correspond to the three main parts of this research. Each subsection provides a detailed description of the experimental procedures, results, and discussion for the respective part. The first part of this research aims to extend the lifespan of the W filaments. The second part focuses on the experimental parametric growth study of diamond films, while the last part of this research deals with the designs proposed for the new clamping device.

5.1 Extended lifespan of single W filament

To enable diamond growth in the new HF-CVD setup, the first crucial step is to extend the lifespan of a single W filament. For this, the possibilities within the existing configuration were investigated before considering any modifications to the HF-CVD setup. This subsection outlines the steps that were taken to extend the lifespan of the W filaments, followed by the results and discussion.

5.1.1 Filament configurations

Before initiating the CVD process, the filaments need to be prepared. The W wires were wound around small spools in the as-delivered state. When these wires were uncoiled from the spools, some residual curvatures were present. Straightening these wires is essential to obtain filaments of equal length, as small deviations in filament length can induce different responses, such as variations in stress or temperature. This can affect both the filament lifespan and the deposition process. A detailed description of the straightening protocol that was used to prepare the filaments can be found in Appendix B2. Filament straightening protocol. After obtaining straight filaments, several configurations were tested in an effort to increase the lifespan of the filaments.

In the original configuration, the filament is subjected to some out-of-plane stresses, as can be seen in Figure 5.1. On the left end, in between the molybdenum electrode and the circular guide electrode, a downward force is exerted on the filament by the dead weight. Similarly, on the right end, some out-of-plane stresses are induced due to the clamping of the filament.

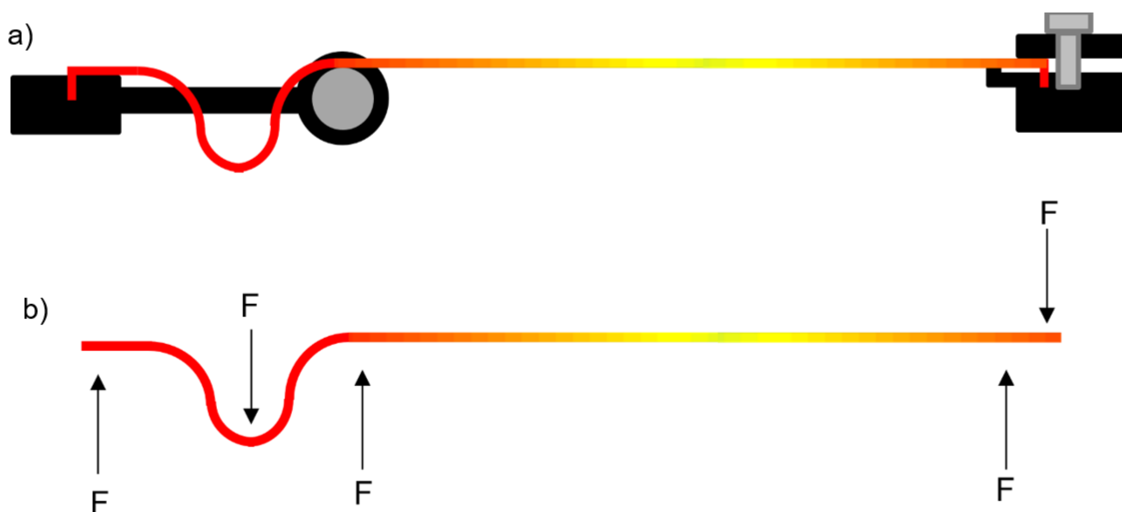

Figure 5.1: Schematic representation of a) the original configuration and b) forces acting on the filament (approach A) *The region in yellow represents the highest temperature and the region in red represents a lower temperature*

An effective starting point for this experimental study was to change the positioning of the filament within the existing clamping device (see Figure 4.2), with a particular focus on minimizing the out-of-plane stresses on the filament, and evaluate how different placements would affect the lifespan of the filaments. Various configurations of the filaments were tested to identify the optimal placement (see Figure 5.2). The first set of experiments involved a combination of coiled and straight configurations (approach B). The difference in stiffness between the coiled and straight parts may compensate for the thermal and carburization expansion of the straight part, which is actively heated between the two contact points. These experiments included configurations with one, two, and three coils. In the second series of experiments, the filament was fixed on the left end with a loop to ensure good electrical contact with the circular guide electrode (approach C). In the final set of experiments, a straight filament was resting on both electrodes (approach D). The fixation plate that was used to clamp the filament on the right end was removed to reduce the out-of-plane stresses on the filament even further.

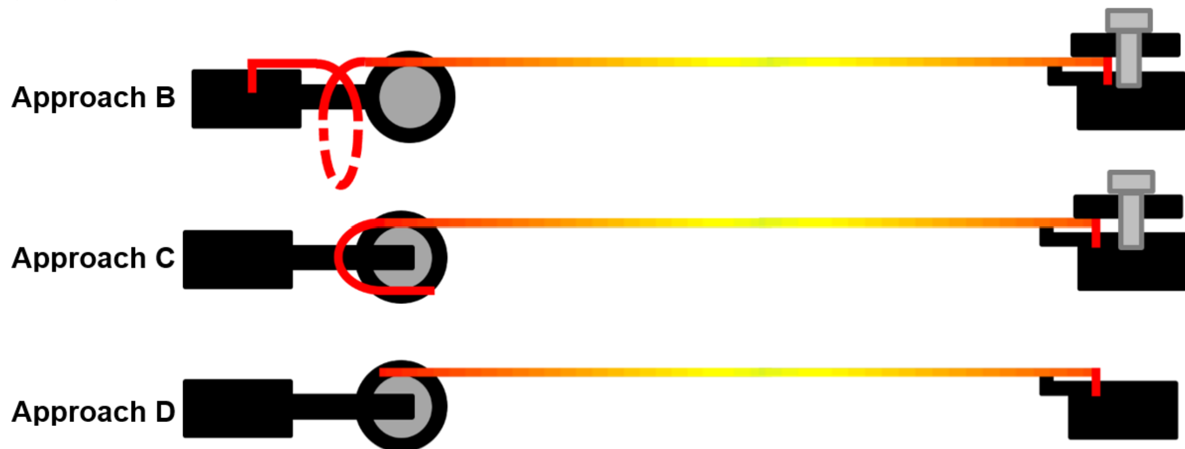

Figure 5.2: Schematic representation of different filament placements (approaches B, C, and D)

Table 5.1 provides an overview of the experiments that were performed in the first part of this study. The different placements of the filaments are represented by the letters A (dead weights), B (coiled + straight), C (loop), and D (rest), as explained above. This table summarizes the gas composition (vol.% CH_4), applied electrical current (A), operating time (h), number of interruptions, and state of the filaments (functional or non-functional) for each experiment. The filament state is classified as functional if it remained intact after usage and non-functional if it failed.

Table 5.1: Parameters used during and the final filament state after the filament-related experiments

Experimental sequence number	CH_4 (vol.%)	Filament current (A)	Operating time (h)	Number of interruptions	Filament state
A	0.5	23	5 ¼	1	Non-functional
B1			4 ¼	1	
B2	0.5	23	9	2	Non-functional
B3			8 ½	2	
C1	0.5	23	13 ½	2	Functional
C2			24	3	Functional
C3	1.0	23	32 ¾	7	Non-functional
C4			31	4	Non-functional
D1	1.0		27 ½	4	Functional
D2	1.0		51 ½	7	Functional
D3	1.0 – 2.0	23	41 ¼	6	Functional
D4	1.0		162	25	Functional
D5	1.0		43	6	Functional
D6	1.0	21	7 ¼	1	Functional
D7	1.0	24	3 ¾	1	Non-functional

In experiments D1 - D4, temperature measurements were performed since the optical pyrometer (see Figure 4.3) became only available halfway through this research project. The temperature measurements were carried out during stable filament operation. The measured filament temperatures at the corresponding voltages are given in Table 5.2.

Table 5.2: Temperature measurements performed during a selection of filament carburization experiments

Experimental sequence number	**Voltage (V)**	**Temperature (°C)**
D1	12.0	Tu = 2130 Te = 2173
D2	12.6	Tu = 2140 Te = 2184
D4	13.0	Tu = 2160 Te = 2205
D5	13.7	Tu = 2200 Te = 2254

The uncorrected filament temperatures are represented by T_u and the emissivity corrected temperatures by T_e. The filament temperatures exhibit a direct correlation with the filament voltage, as higher voltage leads to an increase in filament temperature.

In the original configuration, the W filament lasted for 5 ½ hours and experienced failure during the first cooling-down process. The failure occurred in the region near the clamping on the right end, as illustrated in Figure 5.3a. An improvement in lifespan was noticeable when the filaments were placed according to the second configuration (approach B). This placement enabled the use of the W filaments for multiple interrupted deposition runs. However, in this configuration, the filaments survived for a maximum of 9 hours and failed right after the second cooling-down process. Throughout these experiments, the failure was observed either in the middle or near the clamping on the right (see Figure 5.3b). A notable improvement was observed with the placement of the filaments according to the third configuration (approach C), resulting in a substantial increase in filament lifespan. In this configuration, the W filaments were able to operate for over 30 hours with up to seven interruptions. The failure occurred in the middle region and was preceded by localized thinning at the point of failure (see Figure 5.3c). The most promising results were obtained when the filaments were simply resting on both electrodes (approach D). In this configuration, the W filaments showed a maximum lifespan of 162 hours, withstanding up to 25 interruptions (see Figure 5.3d).

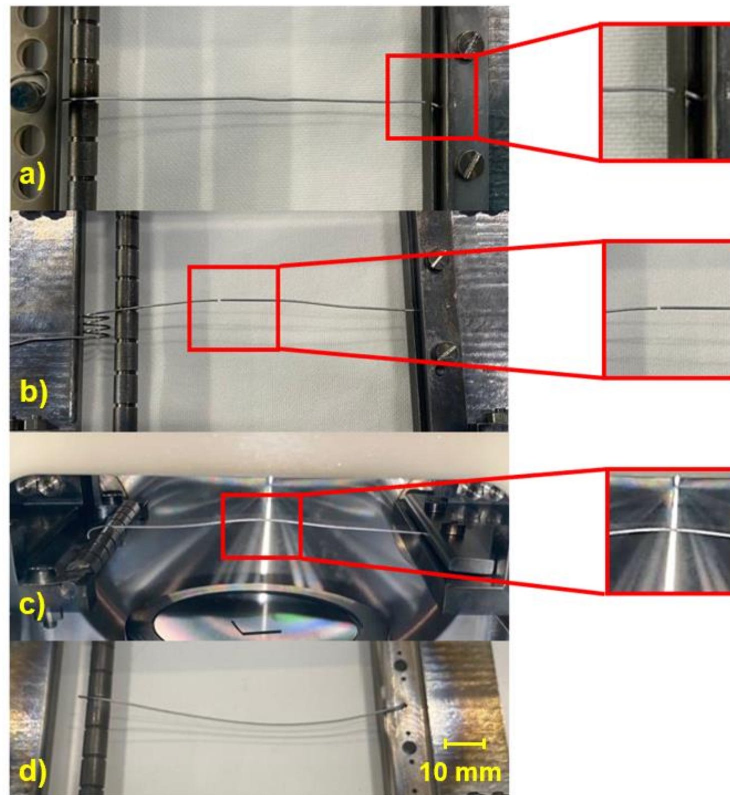

Figure 5.3: Optical images showing the failure modes and deformations of the filaments after several hours of usage when placed according to a) original configuration, b) approach B (experiment B3), c) approach C (experiment C2) and d) approach D (experiment D5)

The filaments expanded when heated from room temperature to operating temperatures and were therefore subjected to thermally-induced stresses. Furthermore, during the CVD process, the filaments reacted with the carbon-containing gases, resulting in the formation of W carbides, further lengthening and embrittling the filaments, as explained previously (see Section 2.3). In the first two configurations (approaches A and B), the filaments were constrained on both sides, limiting their expansion along the filament axis. This led to the development of internal stresses within the filament, resulting in premature failure of the filaments. The metal carbides are very delicate and brittle and therefore have limited ability to withstand stresses, making them prone to failure [45]. A previous study revealed that the bending strength was strongly correlated to the degree of carburization [36]. It was found that in the initial stages of carburization, the bending strength decreased significantly, making the filaments more prone to failure. Similar results were obtained from experiments A and B, with the filaments failing at the location where small (bending) curvatures were present during the initial stage of carburization. Providing a certain degree of freedom of movement on one side can effectively reduce the development of internal stresses, thereby increasing the lifespan of the filaments. This favorable condition was achieved in the third configuration (approach C), where the filaments were securely hooked on the left circular electrode, and in the final configuration (approach D), where the filaments were simply resting on both electrodes. Especially in the latter, the filaments were allowed to move more freely over the left circular electrode due to lower friction between the filament and the electrode since the contact area was less than in the third approach, and no fixation force was present.

5.1.2 Filament carburization

The carburization results obtained from the experiments using W filaments are presented in Figure 5.4. This figure illustrates the relation between voltage and carburization time. The starting voltage of the filaments prior to carburization is usually in the range of 5.5 – 6.5 V. The experimental results can be divided into two distinct series. The first series of experiments (Exp. A – C2) used a gas-mixture ratio of 0.5 vol.% (1.5 sccm) CH_4 and 99.5 vol.% (301.5 sccm) H_2, and the corresponding carburization results are represented by the blue plots. The second series of experiments (Exp. C3 – D7) used a gas-mixture ratio of 1 vol.% (3 sccm) CH_4 and 99 vol.% (300 sccm) H_2, represented by the red plots. The D-series experiments are denoted by dashed lines. The dash-dotted lines represent experiments D6 and D7, which indicate the use of a different current than 23 A.

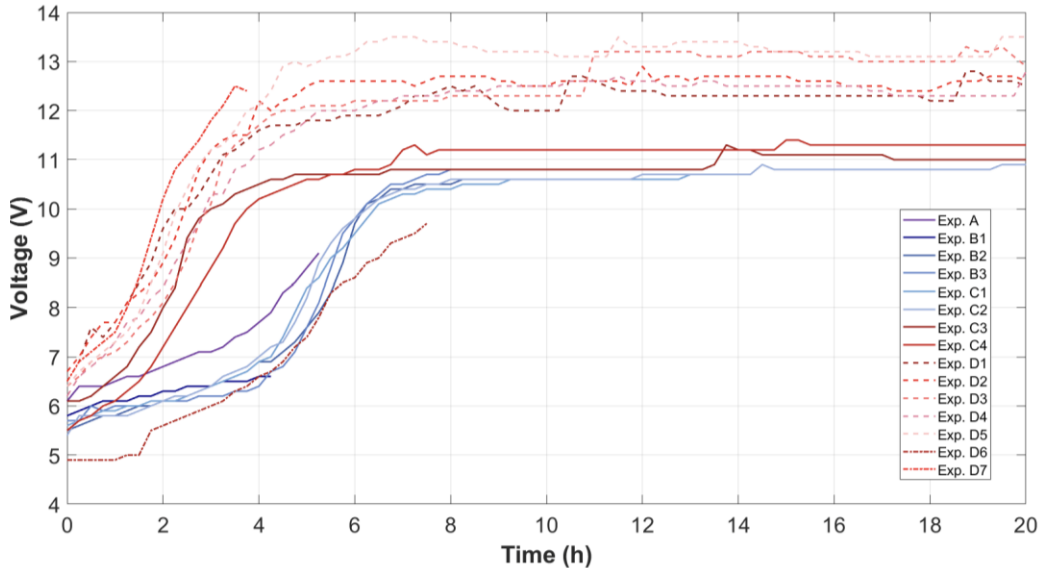

Figure 5.4: Filament voltage vs. time for all carburization experiments

Figure 5.5 provides a more detailed comparison by focusing on specific experiments and zooming in on relevant regions of the data. For experiments performed with 0.5 vol.% CH_4, the average carburization time required to reach a constant filament power consumption (i.e., constant filament voltage) is approximately 8 hours, while experiments using 1.0 vol.% required 5 hours (see Figure 5.5a). Moreover, the experiments in the D series exhibited a higher voltage range as compared to the other experiments. Figure 5.5b shows the graphs for experiments D5, D6, and D7, which were performed using different electrical currents.

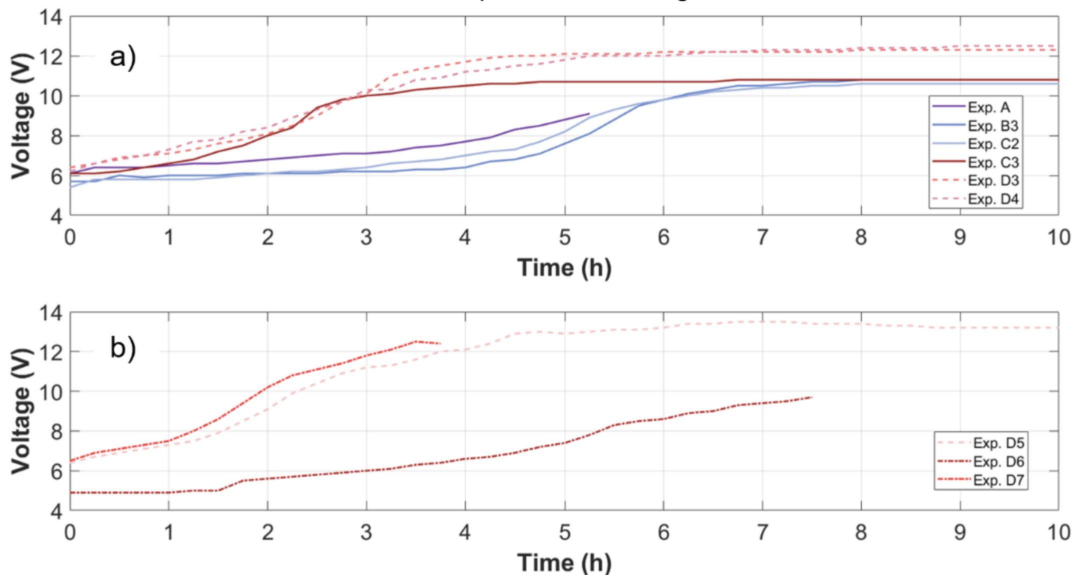

Figure 5.5: Comparison of the carburization results a) using different methane concentrations and different placements, and b) using different electrical currents

The carburization results showed that the rate of carburization increased when the concentration of CH_4 in the gas mixture or filament temperature was raised. This correlation is in agreement with previous findings in the literature and can be explained by Fick's law of diffusion (see Section 2.3.3.1). According to Fick's law of diffusion, the diffusion flux is directly proportional to the concentration gradient, so an increase in CH_4 concentration results in an increase in the diffusion flux (J). Similarly, raising the temperature of the filament leads to an increase of the diffusion coefficient (D), which also increases the diffusion flux and thus the carburization rate.
The carburization results show that the voltage obtained in experiment series D is higher as compared to the experiments of series A, B, and C. This difference is due to the absence of the fixation plate on the right side. Figure 5.6 illustrates the impact of the fixation plate on the activation region of the W filament. When the fixation plate was used (Figure 5.6a), a smaller region of the W filament was activated compared to when no fixation plate was used (Figure 5.6b, corresponding to exp. series D).

The resistance of a wire can be determined by the following equation:

$$R = \rho * (L/A) \quad \text{(Eq. 5.1)}$$

where R (Ω) is the resistance, ρ (Ωm) is the resistivity, L (m) is the length of the wire, and A (m^2) is the cross-sectional area of the wire. When a steady electrical current is applied, the voltage is directly proportional to the resistance (Ohm's law). Therefore, a longer region of filament activation, as is the case for exp. series D, results in a higher resistance and consequently a higher voltage.

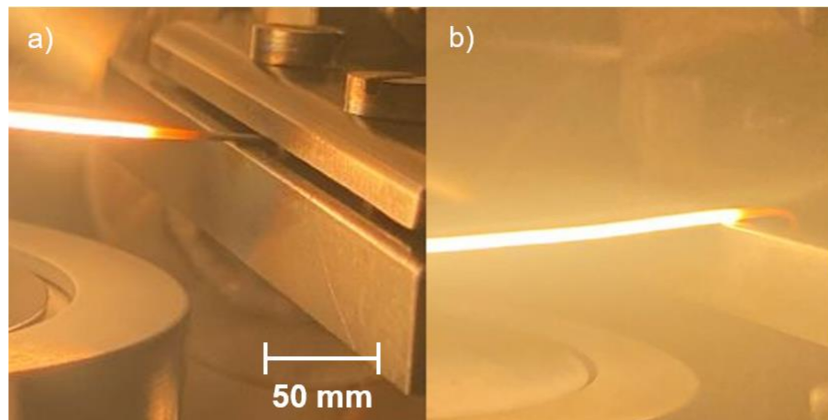

Figure 5.6: Difference in activated filament length when using a) fixation plate and b) no fixation plate

The voltage curves in Figure 5.4 exhibit a similar response as reported in the literature, with one notable difference. Small voltage fluctuations can be observed, which occurred when the filament was heated again after interrupting the HF-CVD process. While no explicit explanation for this phenomenon was found in the literature, several potential factors may contribute to this behavior. One possibility is that the filaments were poisoned during the cool-down or heat-up process, particularly at temperatures ≤1900 °C (see 'filament poisoning' Section 2.3.3.1) [27, 29, 31]. This poisoning results in the formation of a graphite layer, which partially or entirely covers the filament surface and inhibits the filament to activate the chemical precursors in the gas mixture. Similarly, carbon deposits were observed on the surface of a filament (see Figure 5.7a) that had been used for multiple interrupted carburization runs. The presence of foreign atoms or molecules (such as carbon or oxygen) on the surface of the filament and the formation of irregular microcracks (see Figure 5.7b) along the length of the filament can disrupt the flow of electrons, leading to deviations in filament resistance or voltage when a steady electrical current is applied.

Concentric metal carbide layers were formed during the carburization of the W filaments, as can be seen in Figure 5.7c. Different phases were observed at the outer lateral ends of the filament, while in the middle, no visual distinction in phase can be made. This non-uniformity in carburization is due to the temperature difference between the middle and the outer parts of the filament, since the temperature of the filament near the clamping is lower than in the central parts, and therefore the carburization at the filament ends proceeded at a slower rate (see 'Electrical Resistance' Section 2.3.3.1).

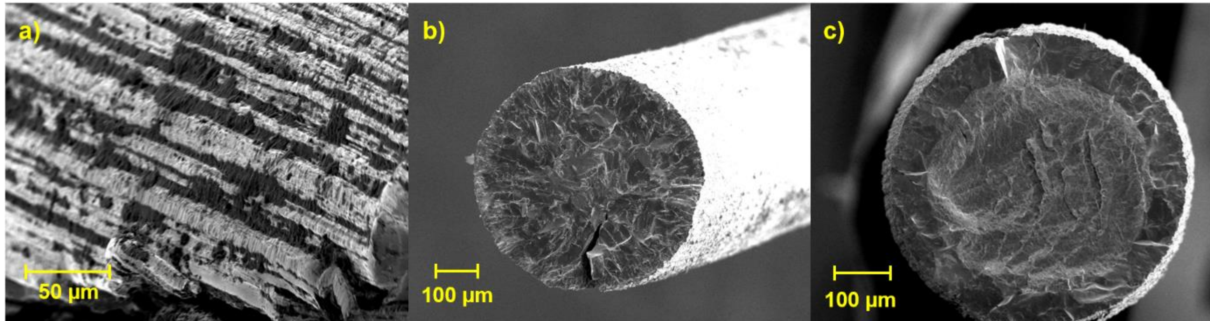

Figure 5.7: Carburized W filament (exp. C1) after 13 ½ h carburization with a) top view of the filament surface with carbon deposits (black dots), b) cross-section of the middle part of the filament, and c) cross-section of the outer end of the filament showing different material phases

As the carburization proceeded, the filaments elongated and exhibited a sagging effect. Figure 5.8 illustrates the deformation of a carburized W filament (exp. D4) over time. Similar observations were found in the literature [34, 46, 47]. Besides the thermal and carburization expansion, the weight of the filament contributed to the deformation and sagging of the filament. In a study on W filaments, changes in the grain size of the filament were noticed during the carburization process [34]. These changes are accompanied by grain boundary sliding, which, along with the diffusional creep, eventually results in the sagging of the filaments [31,45].

Figure 5.8: Deformation of W filament (exp. D4) after a) 8 h, b) 35 h, and c) 148 h of carburization

5.2 Diamond growth

The second part of this research focuses on diamond growth using the new HF-CVD setup. This process can be divided into two main steps. The first step involved sample preparation, as described in Section 4.5. Once the substrate is prepared, the next step is the diamond synthesis process, which takes place inside the HF-CVD setup. This section will present and discuss the results of the experimental parametric growth study.

5.2.1 Parametric growth conditions

The effect of key parameters (filament-substrate distance, substrate temperature, and gas composition H_2/CH_4) on diamond growth and quality was investigated. Six experiments were planned for each parameter study. In all the experiments, the stage was rotated at a speed of 10 rpm. In the first series of experiments, the filament-substrate distance was varied in the range of 4 to 14 mm with increments of 2 mm, and a 1.0 vol.% methane concentration was used. In the second parameter study, the stage temperature was adjusted in the range of 360 to 780 °C. The target stage temperature was set on the heater controller, and the settings on the DC power supply were adjusted accordingly. However, at higher substrate temperatures (> 750 °C), the stage did not receive the required power to maintain a steady temperature, leading to small temperature fluctuations (i.e., +/- 20 °C). In the third parameter study, the hydrogen to methane ratio was varied while the total gas flow was maintained at 303 sccm. The last three experiments (i.e., experiments G4 - G6 using methane concentration of ≥ 2.0 vol.%) in this series could not be performed due to stage malfunctions and detected system leakages. In the second and third parameter studies, the filament-substrate distance was maintained at 10 mm. An overview of the experiments that were performed is given in Table 5.3.

Table 5.3: Overview of the experimental parameters used during the parametric growth study

Parameter study	Experimental sequence number	Filament-substrate distance (mm)	Stage temperature (°C)	CH_4 concentration (vol.%)
	1	4		
	2	6		
E	3	8	780 ± 20	1.0
	4	10		
	5	12		
	6	14		
	1*		360 ± 1	
	2*		450 ± 1	
F	3*	10	540 ± 1	
	4*		630 ± 1	1.0
	5		720 ± 5	
	6		780 ± 20	
	1*			0.5
G	2*	10	780 ± 20	1.0
	3*			1.5

Experiments marked with * indicate pressure fluctuations in the range of ~1.0 – 2.0 mbar during the experiments, which were caused by the malfunctioning of the stage and associated system leaks

5.2.2 Substrate pre-treatment

The spin-seeding approach is frequently used for the pre-treatment of Si wafers to achieve thin, continuous, and high-quality polycrystalline diamond films through HF-CVD [24, 48]. Typically, an ethanol-based seeding dispersion is used as liquid material, and homogeneous seed layers with seeding densities up to 5 x 10^{10} cm^{-2} (see Figure 5.9a) can be obtained [24]. Similar steps were applied in this research as described in Section 4.5. Figure 5.9b shows the SEM image of a seeded sample obtained using the stock solution in this research. To determine the seeding density, three SEM images of three different samples were analyzed using ImageJ software. The results showed that the average seeding density obtained was about 5 x10^{10} cm^{-2}, which is consistent with the densities reported in the literature.

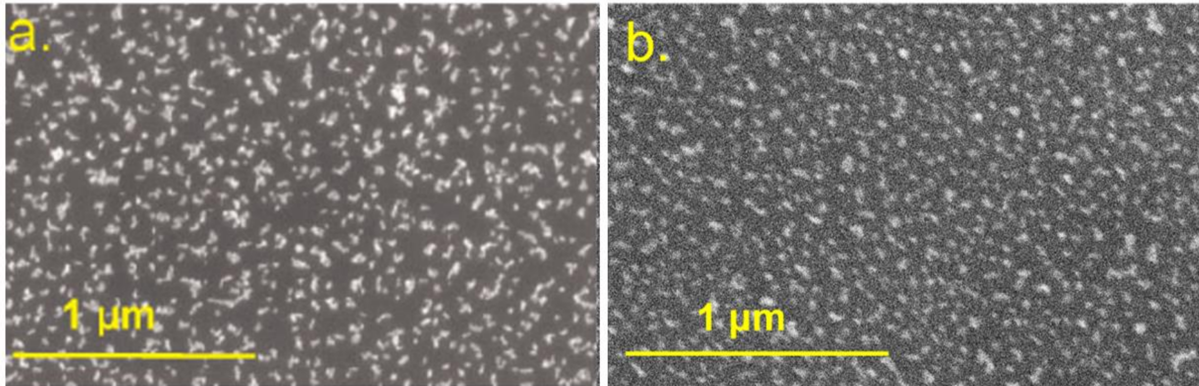

Figure 5.9: SEM images of seeded samples a) using an ethanol-based ND dispersion (adapted from the literature) and b) using in-house stock solution

It is important to note that the calculated seeding density is based solely on the image analyses of three SEM images of three different samples, and, as the pre-treatment involves several manual steps (e.g., pipetting and rinsing with ethanol), the actual seeding density of the remaining samples may differ slightly from the calculated range.

The following subsections will outline the results and discussion of the experimental parametric growth study. In the experiments, only one deposition parameter was varied at a time, while other (controllable) parameters were held constant. The influence of filament-substrate distance will be discussed first, followed by the effects of stage temperature and variations in methane concentration on diamond film growth and quality, respectively.

5.2.3 Filament-substrate distance variation

Figure 5.10 presents a complete set of SEM micrographs of the diamond films obtained from the first parameter study (experiments E1 - E6), where the filament-substrate distance (d_{fs}) was varied. The surface morphologies of the diamond films are shown by the plan-view SEM images, while the cross-section morphologies are shown by the corresponding insets. Continuous polycrystalline diamond (PCD) films were successfully synthesized. The diamond films comprise large, well-faceted pyramid-shaped polycrystals, which are predominant in films obtained at lower filament-substrate distances, and smaller, un-faceted crystals, which are more prevalent at larger filament-substrate distances. When observing Figure 5.10 from top to bottom, column by column, a decrease in average grain size can be observed with increasing filament-substrate distance. The diminishing grain sizes are accompanied by an increasing number of grain boundaries.

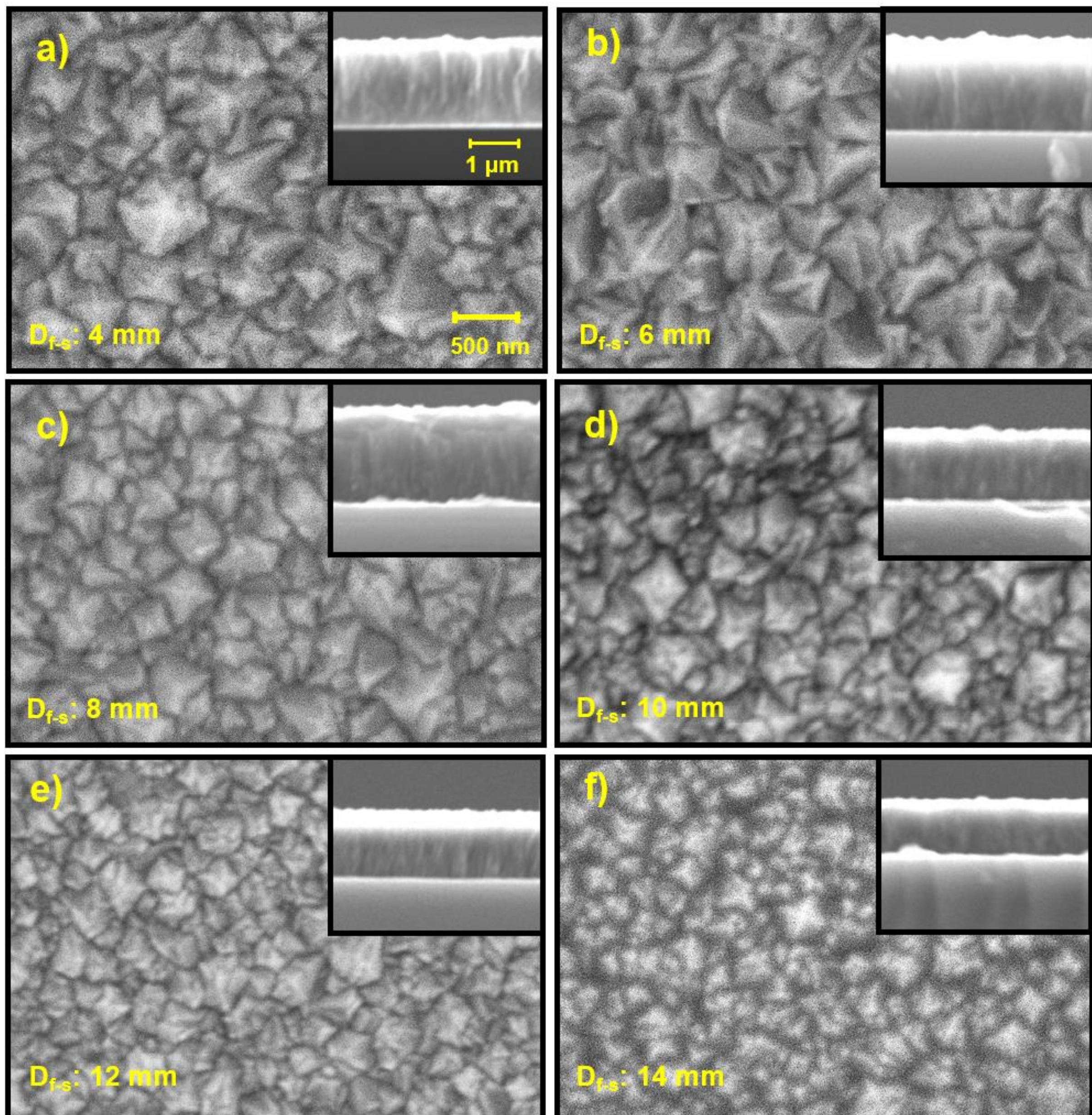

Figure 5.10: SEM micrographs showing the surface and cross-section (insets) morphologies of diamond films obtained at varying filament-substrate distance

The average grain size and growth rate as a function of the filament-substrate distance are shown in Figure 5.11 and Figure 5.12, respectively. Variations in grain size were visible, as indicated by the error bars (see Figure 5.11), ranging from tens of nanometers to sub-micron-sized crystals. Increasing the filament-substrate distance from 4 mm to 6 mm resulted in a noticeable increase in both the average grain size and growth rate, followed by a persistent decline with increasing filament-substrate distance. The maximum average grain size (~433 nm) and highest growth rate (~267 nm/h) were achieved at a filament-substrate distance of 6 mm, whereas the minimum average grain size (~267 nm) and lowest growth rate (~143 nm/h) were obtained at 14 mm.

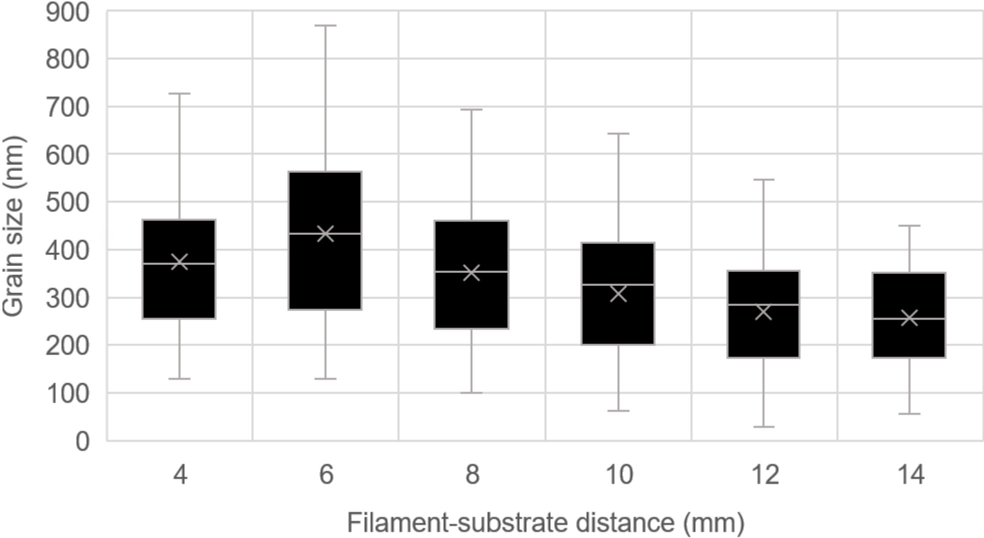

Figure 5.11: Boxplot showing the effect of filament-substrate distance on (average) grain size (the average grain size is indicated by the cross and the median by the horizontal line)

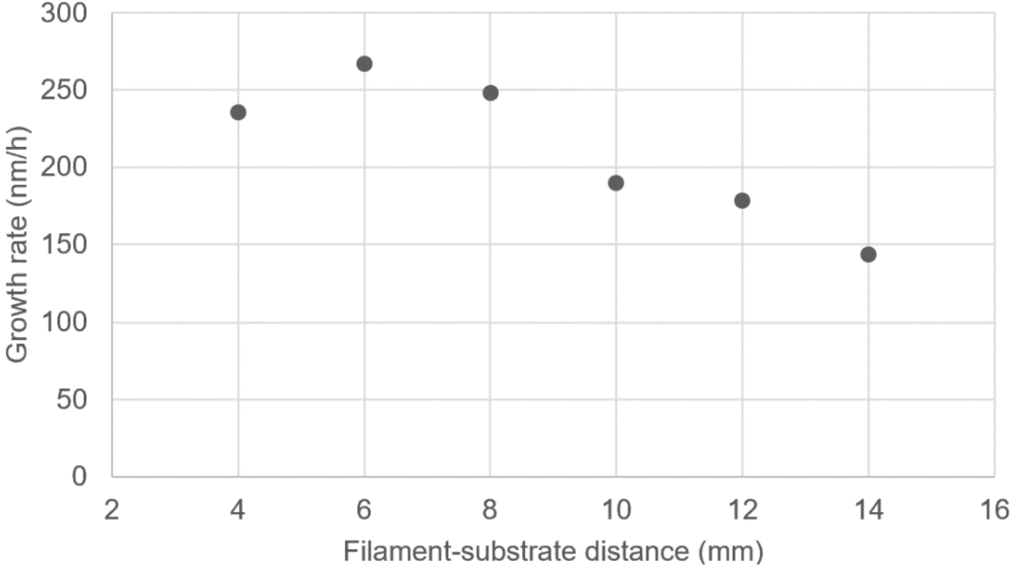

Figure 5.12: Influence of the filament-substrate distance on diamond film growth rate

The obtained diamond films exhibited a consistent morphology across the entire substrate surface. However, large variations in grain sizes were observed, particularly in the films synthesized at low filament-substrate distance. The average grain size and growth rate showed some correlation with changing filament-substrate distance. While no clear monotonic trend can be observed, the literature and theory were consulted in order to explain this dependency.

Previous studies have reported that the gas-phase chemistry is strongly affected by the distance (x) measured from the filament, where $x = 0$ represents the zone in the immediate vicinity of the filament [49–52]. The gas temperature and the production of atomic hydrogen (H) are highly dependent on this parameter. The independent effect (i.e., separate substrate heating) of filament-substrate distance on diamond film growth was investigated in a previous study [49]. This study revealed that reducing the filament-substrate distance resulted in a significant increase in both the growth rate and film quality. Specifically, in the near filament region, the concentration of reactive species H and CH_3 was significantly higher as compared to more distant regions. In particular, an increase in the [H] / [CH_3] ratio was observed for lower values of x due to the higher temperatures, promoting diamond growth and film quality at low filament-substrate distances [49, 51, 52]. However, in the immediate vicinity of the filament, the high filament temperature led to complex gas-phase chemistry. The high filament temperature does not only promote the production of H, which in turn generates CH_3 radicals, but also causes cracking of the hydrocarbons and converts parts of the CH_4 precursor into C_2H_2 (or other C_2 species), which is the thermodynamically stable compound at the typical filament temperature of about 2100 °C [10, 53]. This process can lead to the depletion of CH_4 and CH_3 radicals, decreasing both diamond growth and film quality in the immediate vicinity of the filament. Furthermore, the reactive species concentration on the substrate level decreases with increasing filament-substrate distance as a result of the decreasing gas temperature, resulting in more recombination of H in the gas phase and subsequently lowering the H concentration near the substrate surface [10]. The reported findings are consistent with the results of this study and provide a plausible explanation for the dependency of the diamond growth on filament-substrate distance.

It is important to emphasize that the actual substrate surface temperature can deviate from the set stage temperature (780 °C ± 20 °C) since the substrate surface is exposed to the radiant heat from the hot filament. Previous studies have shown that the substrate temperature is affected by the filament-substrate distance even when a separate heater stage is used [51, 54–56]. However, the effect of variations in substrate temperature on diamond growth is not considered part of this discussion but will be covered in the next section (Section 5.2.4).

The Raman analysis of the obtained diamond films provides insights into the contributions of various factors, including the heat supplied by the filament, the heat supplied by the stage, and the reaction of the precursors at different distances from the hot-filament surface, leading to nucleation and film growth on the substrate surface. Figure 5.13 illustrates the Raman spectra of the diamond films grown at varying filament-substrate distance. Two distinct signals can be observed in all recorded Raman spectra. The sharp peak at around 1332 cm^{-1} corresponds to diamond and indicates the presence of sp^3 carbon, while the broad G band in the range of 1500 cm^{-1} – 1600 cm^{-1} is due to various non-diamond carbon (NDC) phases, indicating the presence of sp^2 carbon [57, 58]. Furthermore, minor peaks can be observed at ~1140 cm^{-1} for diamond films grown at filament-substrate distances of 10 mm or greater and are associated with trans-polyacetylene (TPA) at the grain boundaries [56, 57]. The Raman spectral data are summarized in Table 5.4.

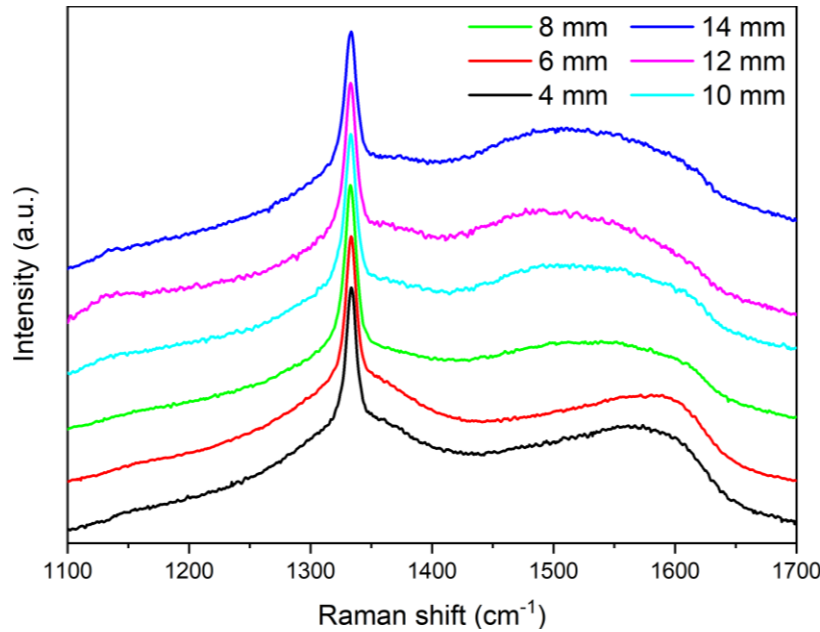

Figure 5.13: Raman spectra of the diamond films grown at different filament-substrate distance

Qualitative information on the quality of diamond films can be gained from the Raman spectra. The quality of diamond films can be assessed by determining the sp^3 / sp^2 ratio from the intensities of the diamond peak (I_D) and G-band (I_G) [52, 59]. A decrease in the I_D / I_G ratio is noticeable (see Table 5.4) with increasing filament-substrate distance, indicating a reduction in sp^3 carbon content and subsequently diamond film quality. Furthermore, the width of the G band becomes broader with increasing filament-substrate distance (see Figure 5.13), suggesting an increase in disorder in sp^2-bonded carbon. This observation can be related to the visible changes in surface morphology (see Figure 5.10), where a decrease in grain size is accompanied by an increase in the number of grain boundaries for films obtained at higher filament-substrate distances. The grain boundaries are composed of both sp^2 and sp^3-bonded carbon, and as a result of the increasing number of grain boundaries, the sp^2 carbon content increases accordingly, reducing the diamond film quality [2, 57]. In addition, with increasing filament-substrate distance, there is a noticable shift in the G band peak towards the ~1500 cm^{-1} range (Figure 5.13), which indicates the amorphization of the non-diamond carbon content [60].

Table 5.4: Raman spectral data for the diamond films obtained at varying filament-substrate distance

Filament-substrate distance (mm)	**Diamond peak position (cm^{-1})**	**G-band peak position (cm^{-1})**	**I_D / I_G**
4	1333.7	1567.0	2.17
6	1333.4	1571.8	2.07
8	1332.9	1552.4	1.78
10	1333.2	1516.4	1.47
12	1333.2	1497.5	1.38
14	1333.7	1503.2	1.23

Residual stresses are commonly observed in diamond films due to the differences in coefficients of thermal expansion between the substrate and the film, which arise during the cooling process. In addition to these extrinsic stresses, intrinsic residual stresses can arise from the non-diamond carbon material at the grain boundaries [61]. The Raman spectra also allow us to estimate the residual stresses (tensile or compressive) present in the films by analyzing the shift in the diamond peak relative to the peak of pure diamond (1332.1 cm^{-1}). The Raman spectra of all the films showed a minor positive shift from the value of pure diamond, indicating the presence of residual compressive stresses in the range of 446 to 904 MPa, between the diamond film and the underlying seeded Si substrate [57, 61, 62].

5.2.4 Stage temperature variation

The SEM images showing the morphology of diamond films synthesized at various stage temperatures (experiments F1 - F6) are illustrated in Figure 5.14. The films grown at stage temperatures of 360 °C and 450 °C consisted of diamond grains with irregular shapes and relatively small average size. In addition, small gaps between the individual diamond grains can be observed (see Figure 5.14a and Figure 5.14b), indicating incomplete coalescence of diamond grains during the growth process. However, at higher stage temperatures, continuous diamond films were obtained. An increase in the stage temperature to 540 °C resulted in finely faceted diamond grains with primarily triangular {111} faces, and a noticeable increase in grain size was observed. At higher stage temperatures (≥ 630 °C), well-faceted pyramid-shaped polycrystals became more prevalent. The cross-sectional SEM images (see insets in Figure 5.14) show an overall increase in film thickness with increasing stage temperature.

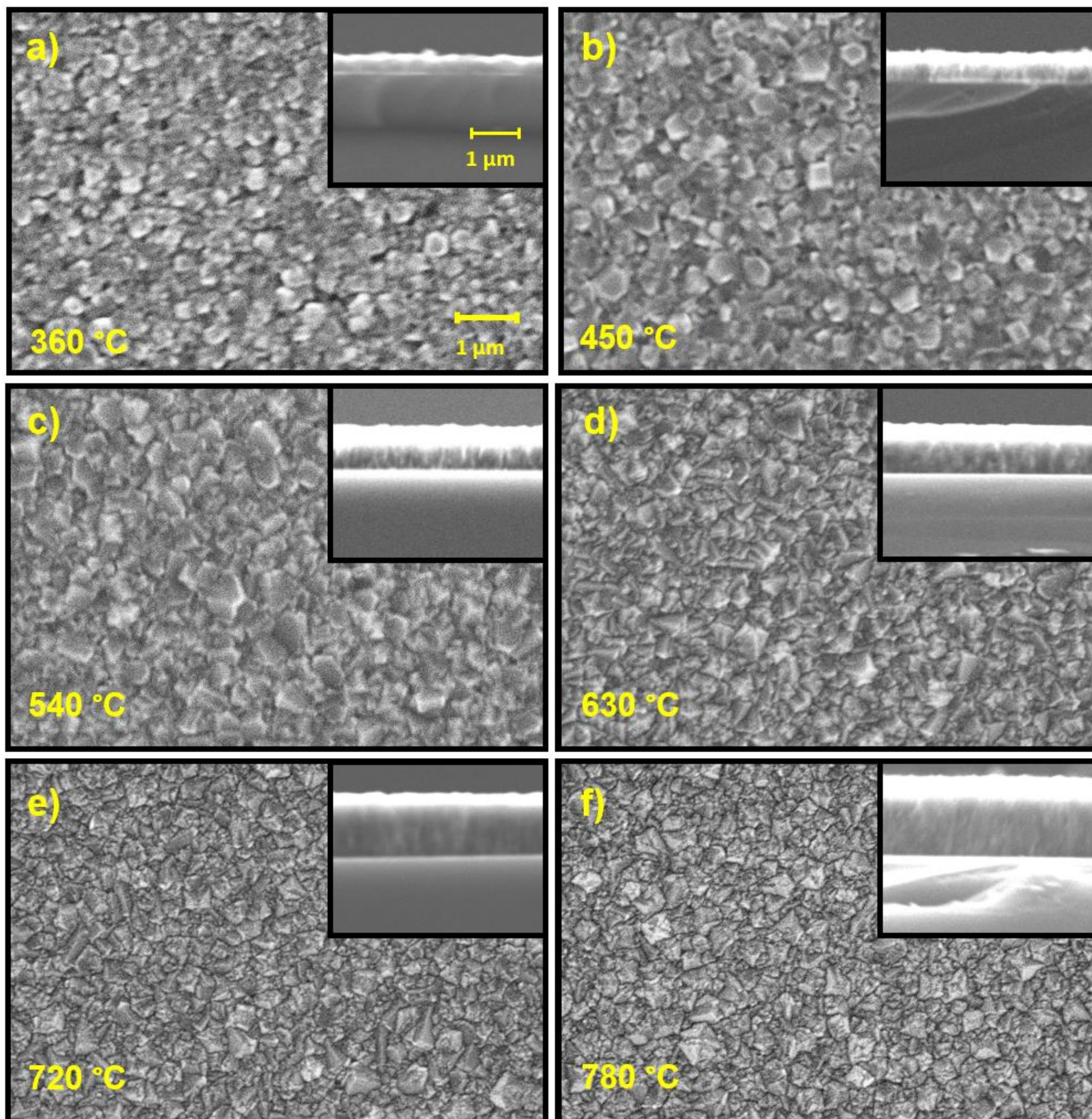

Figure 5.14: SEM micrographs showing the surface and cross-section (inset) morphologies of diamond films obtained at various substrate temperatures

The average grain size and growth rate as a function of the stage temperature are illustrated in Figure 5.15 and Figure 5.16, respectively. The variations in grain size are indicated by the error bars in Figure 5.15. The growth rate showed an overall upward trend, as denoted by the exponential regression line (Figure 5.16). However, a remarkable disruption in the overall upward trend for both grain sizes and growth rate is noticeable at stage temperatures of 540 °C and 630 °C. The maximum average grain size (~352 nm) and highest growth rate (~213 nm/h) were achieved at a stage temperature of 780°C, whereas the minimum average grain size (~273 nm) and slowest growth rate (~ 58 nm/h) were obtained at the lowest substrate temperature of 360°C.

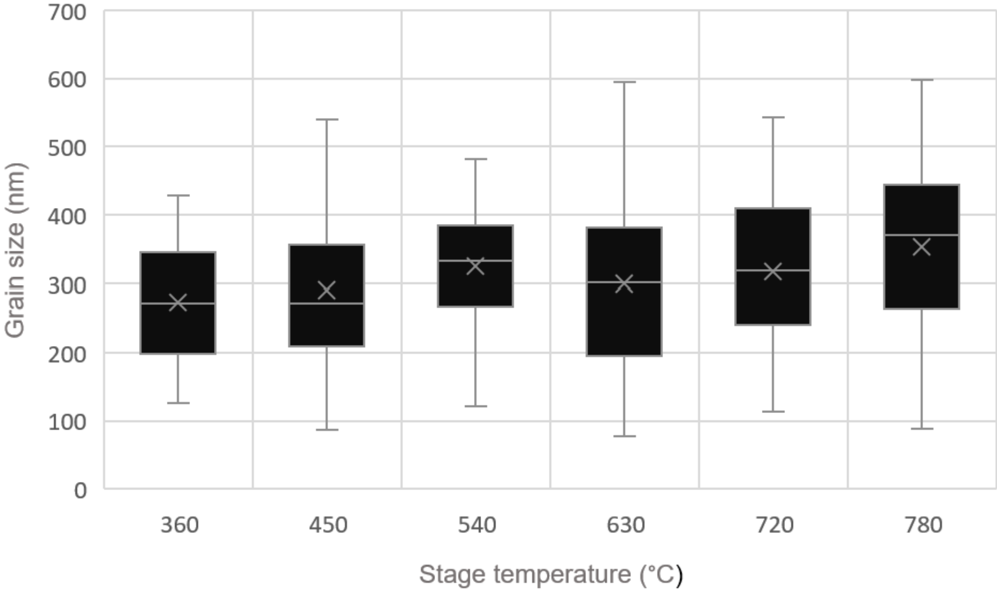

Figure 5.15: Boxplot showing the effect of stage temperature on (average) grain size (average grain size is indicated by the cross and the median by the horizontal line)

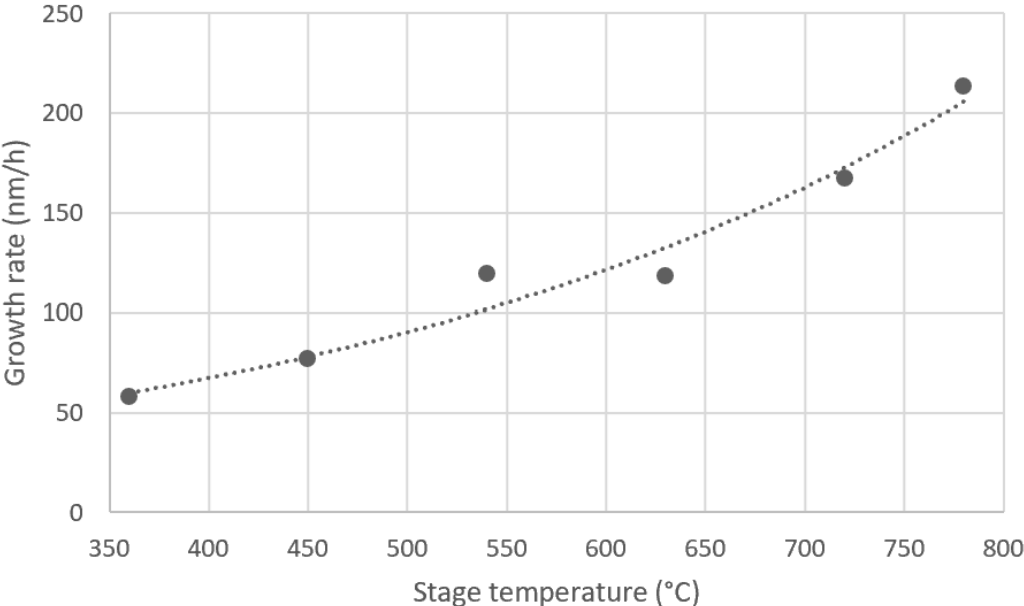

Figure 5.16: Influence of stage temperature on diamond film growth rate

In the existing literature, the term “substrate temperature” is often used instead of the term “stage temperature”. To avoid any confusion in the upcoming discussion, the term substrate temperature will be used from now on.

The diamond morphology and growth rate are strongly correlated to the substrate temperature [52, 54, 56, 63–66]. Typically, at low substrate temperatures, diamond grains with random shapes and small sizes are observed, suggesting the initial stages of diamond (film) nucleation [54, 56]. During this stage, clusters of carbon are formed on the nanodiamond-seeded substrate surface, from which diamond crystals can evolve. An increase in substrate temperature, while keeping all other parameters constant, enhances the surface diffusion of reactive species (e.g., H_2 and CH_4) and consequently promotes the growth of diamond films [63, 66, 67]. Accordingly, a higher growth rate would be expected at a stage temperature of 630 °C compared to 540 °C. However, the experimental results demonstrate slightly contradictory outcomes, which could be related to the pressure fluctuations (1.0 – 2.0 mbar) that occurred during the growth process (see Table 5.3). Pressure has a significant influence on the gas-phase chemistry and the gas speed. For instance, the formation and recombination of H and the residence time of the species are highly sensitive to pressure changes [10, 68]. The deviation in morphology and growth rate observed at 540 °C is apparently due to the increased residence time of the reactant gases in the chamber. A longer residence time results in increased interaction between the chemical precursors, which could consequently promote the formation of reactive species and result in higher growth rates.

The Raman spectra of the diamond films grown at different stage temperatures are displayed in Figure 5.17. The sharp diamond peak at ~1332 cm^{-1} was visible for all analyzed samples. Other peaks were observed at ~1140 cm^{-1}, ~1355 cm^{-1}, and in the ~1470 – 1580 cm^{-1} range. The peak at 1140 cm^{-1} is assigned to trans-polyacetylene (TPA) at the grain boundaries [56, 57]. The peak at 1355 cm^{-1} corresponds to the breathing mode associated with small domains of sp^3 carbon and is also referred to as the D-band [58, 59]. The peaks observed in the 1470 – 1580 cm^{-1} range represent the planar configuration of sp^2-bonded carbon.

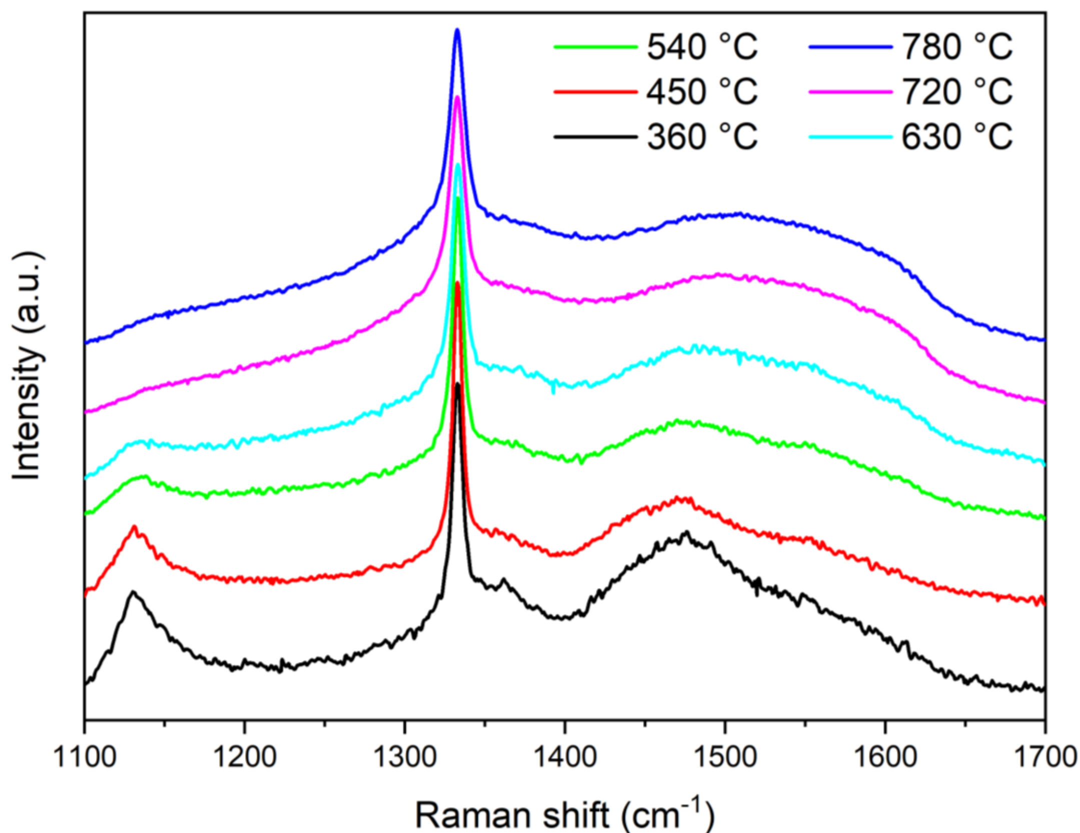

Figure 5.17: Raman spectra of diamond films grown at different stage temperatures

The intensity level of the peaks at 1140 cm^{-1} and 1355 cm^{-1} (D band) is higher for films synthesized at low stage temperatures, and a decrease is noticeable for films obtained at higher stage temperatures. These variations can be linked to the changes in diamond film morphology and microstructure (see Figure 5.14). Increasing the stage temperature generally promotes the growth of larger-sized, well-faceted diamond grains while simultaneously reducing the number of grain boundaries and, therefore, the associated defects. Typically, at higher substrate temperatures, the formation of highly pure diamond with a low non-diamond carbon impurity is favored [63, 66]. Furthermore, a noticeable shift of the G-band peak maximum from ~1470 cm^{-1} to ~1500 cm^{-1} can be observed. Peaks around 1470 cm^{-1} are typically assigned to TPA at the grain boundaries, similar to the 1140 cm^{-1} peak [57]. Conversely, the peak around ~1500 cm^{-1} is often related to disordered amorphous carbon at the grain boundaries. This implies that at lower substrate temperatures, contributions of sp^2-related grain boundaries are dominated by TPA fragments, while at high temperatures by disordered amorphous carbon. The numerical data of the Raman spectra are summarized in Table 5.5.

Table 5.5: Raman spectral data for the diamond films obtained at various stage temperatures

Stage temperature (°C)	**Diamond peak position (cm^{-1})**	**G-band peak position (cm^{-1})**	I_D / I_G
360	1332.9	1475.3	1.81
450	1332.9	1469.9	2.04
540	1333.2	1470.4	1.89
630	1333.2	1481.9	1.56
720	1333.4	1497.5	1.33
780	1332.9	1506.7	1.40

Table 5.5 does not show a clear monotonic trend in film quality. The film grown at 450 °C exhibited the highest quality (i.e., highest I_D / I_G ratio), while the lowest quality was found for the film grown at 720 °C, contradicting the trend reported in the literature. This inconsistency is most likely related to the observed pressure fluctuations during the experiments conducted between 360 °C and 630 °C, caused by gradual malfunctioning of the vacuum seal associated with the heater stage. This makes it difficult to investigate the isolated effect of substrate temperature on diamond growth, as pressure fluctuations were occurring simultaneously. However, the experiments performed at 720 °C and 780 °C, where no pressure fluctuations were present, indicate a certain improvement in terms of film quality. This observation is consistent with the literature, as higher substrate temperatures result in improved film quality under stable growth conditions.

Based on these results, it is evident that even small pressure fluctuations have a significant influence on the overall growth process, disrupting the expected effects of substrate temperature on the diamond growth. Furthermore, the measured diamond peak in the grown diamond films exhibited a positive shift compared to the peak of pure diamond, indicating the presence of compressive stresses ranging from 446 MPa to 749 MPa in the film.

5.2.5 Methane concentration variation

In the last part of the parametric growth study, the gas mixture was varied with methane concentrations of 0.5 vol.%, 1.0 vol.%, and 1.5 vol.% (experiments G1 - G3). The SEM images of the obtained diamond films are shown in Figure 5.18. It can be seen that the surface and cross-sectional morphologies of the diamond films strongly change with the CH_4 concentration. The PCD films were continuous and consisted of faceted crystals of different average grain size and with a film morphology strongly determined by secondary nucleation in the case of using 1.5 vol.% CH_4. Notably, small-sized diamond grains were observed at 0.5 vol% CH_4, while an increase in concentration to 1.0 vol.% CH_4 resulted in the formation of larger diamond grains. The film thickness increased significantly as higher CH_4 concentrations were used. After a growth of 7 ½ hours, the film thickness was ~0.8 µm when using 0.5 vol.% CH_4 and ~2.3 µm when using 1.5 vol.% CH_4. This indicates a nearly threefold increase in film thickness upon increasing the CH_4 concentration by a factor of three.

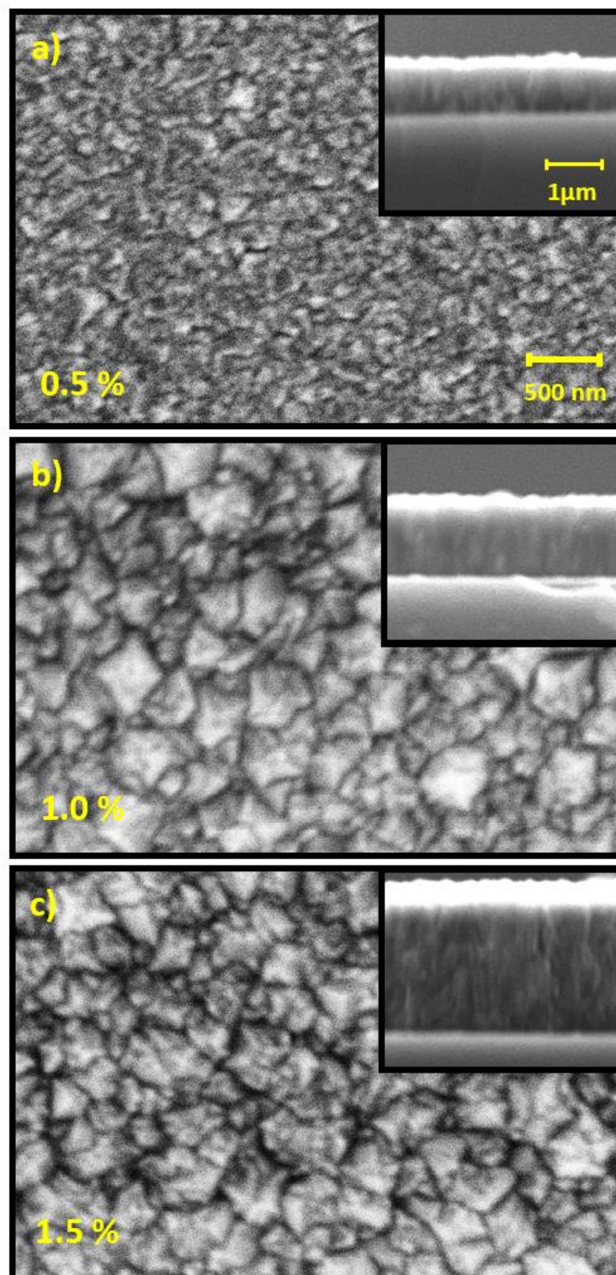

Figure 5.18: SEM images showing the surface and cross-section morphologies of diamond films grown at a) 0.5 vol.% CH_4, b) 1.0 vol.% CH_4, and c) 1.5 vol.% CH_4

The average grain size and growth rate for diamond films grown using various methane concentrations are shown in Figure 5.19 and Figure 5.20, respectively. The average grain size and growth rate show a consistent upward trend with increasing CH_4 concentration. The maximum average grain size (~425 nm) and highest growth rate (~303 nm/h) were achieved at 1.5 vol.% whereas the minimum average grain size (~271 nm) and slowest growth rate (~107 nm/h) were obtained at 0.5 vol.% CH_4. Again, pressure fluctuations were observed during these experiments. The experiments using higher CH_4 concentrations (> 1.5 vol.%) could unfortunately not be conducted due to the significant pressure fluctuations induced by system leakages.

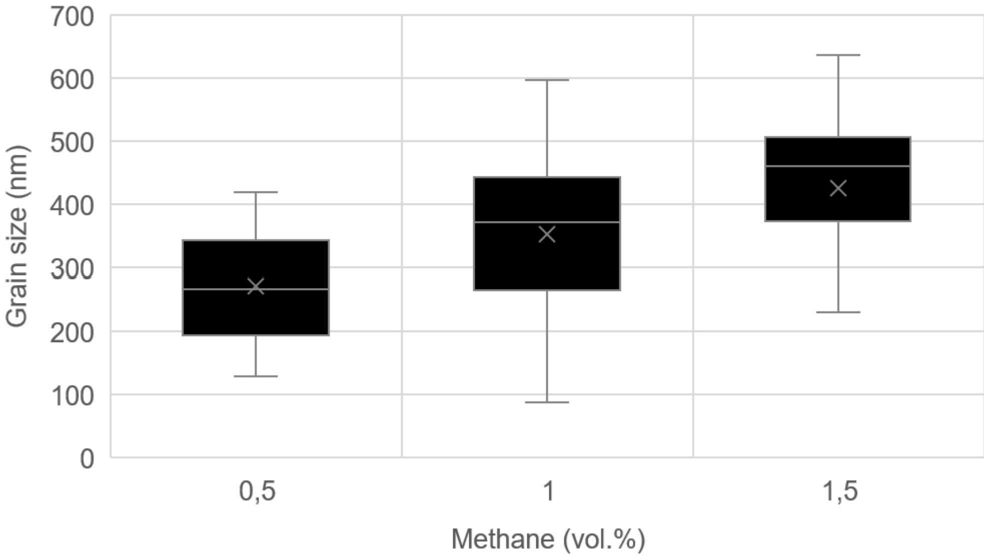

Figure 5.19: Boxplot showing the relation between the (average) grain size and methane concentration (average grain size is indicated by the cross and the median by the horizontal line)

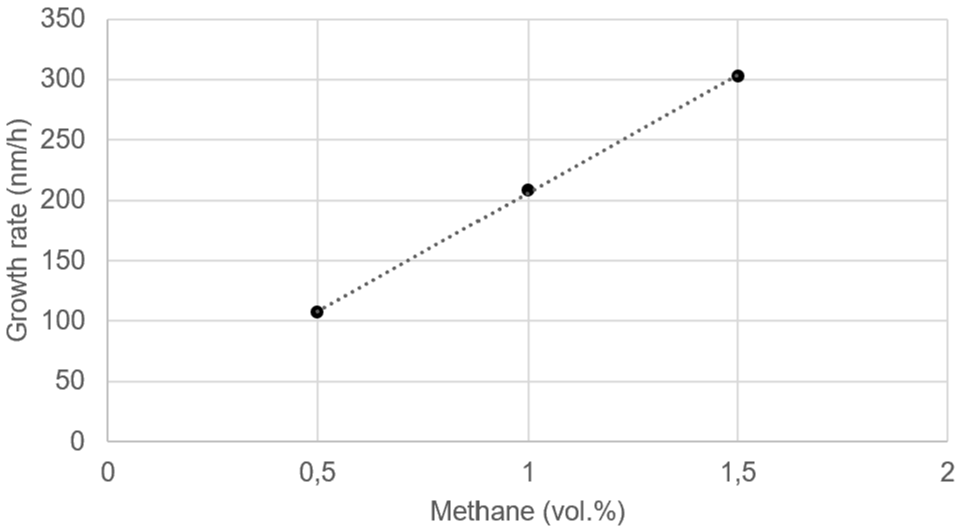

Figure 5.20: Influence of methane concentration on diamond film growth rate

The trend observed is readily attributed to the methane concentration, as it directly affects the availability of activated radicals. An increase in methane concentration consequently results in an increase in methyl radicals, which are considered the main source for diamond growth [62, 65, 68, 69]. However, it is important to note that to obtain high-quality, well-faceted diamond films, the [H] / [CH_3] ratio needs to be sufficiently high at the substrate. Typically, an increase in CH_4 concentration leads to a reduction in the [H] / [CH_3] ratio at the substrate level, resulting in increased (re)nucleation and consequently the formation of poor-quality diamond films [10, 69]. The latter follows from the increased amount of non-diamond carbon, which is due to ineffective etching of sp^2 content at relatively lower H concentrations [66].

Figure 5.21 presents the Raman spectra of the diamond films grown using different CH_4 concentrations. The diamond peak (~1332 cm^{-1}) and the G band (1500 cm^{-1} – 1600 cm^{-1}) are observed in all the films. Additionally, small TPA peaks (~1140 cm^{-1}) and D-bands (~1350 cm^{-1}) were noticeable in the diamond films grown at 0.5 vol.% and 1.0 vol.% CH_4. The shift of the G-band maximum from ~1550 cm^{-1} towards 1500 cm^{-1} with increasing CH_4 indicates the amorphization of the disordered sp^2 carbon content, as explained previously. Also, the intensity ratio (I_D / I_G) is decreasing with increasing CH_4 concentrations. This observation is confirmed by the Raman spectral data shown in Table 5.6.

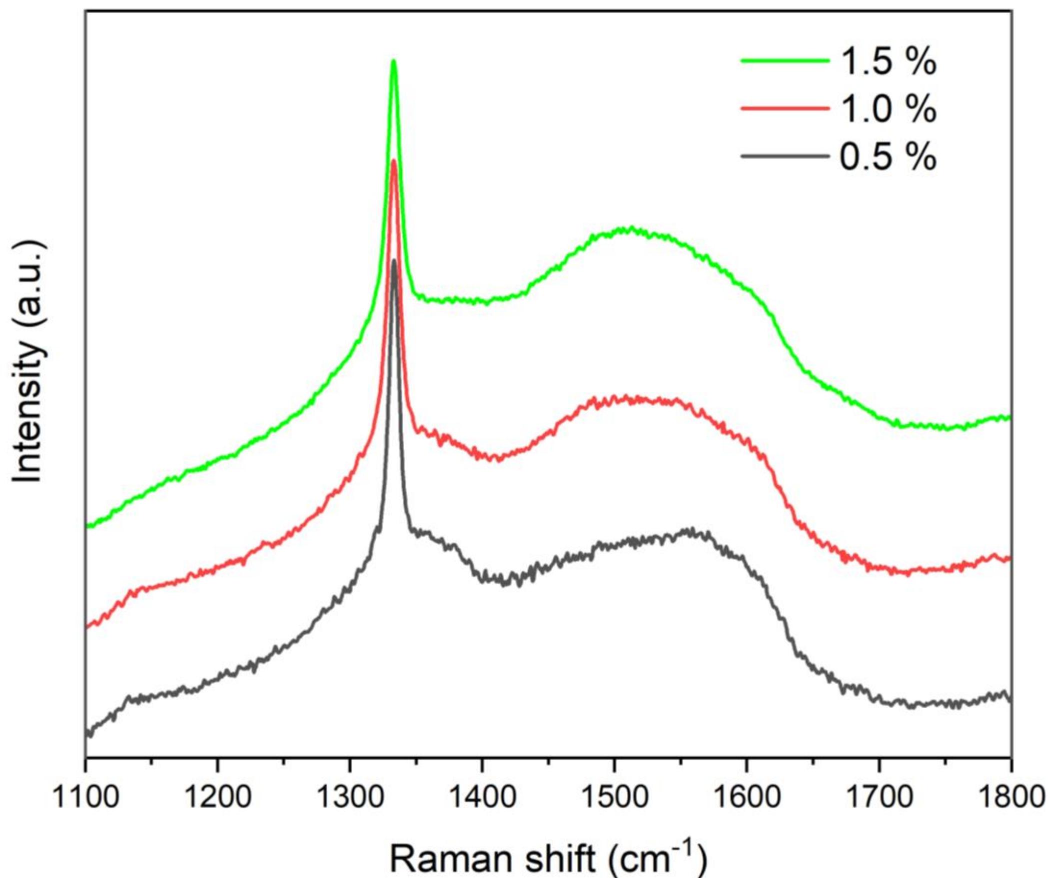

Figure 5.21: Raman spectra of diamond films grown at various methane concentrations

Table 5.6: Raman spectral data of diamond films synthesized using different methane concentrations

Methane (vol.%)	**Diamond peak position (cm^{-1})**	**G-band peak position (cm^{-1})**	I_D / I_G
0.5	1333.4	1559.0	2.17
1.0	1333.2	1508.6	1.65
1.5	1333.2	1513.3	1.32

The decrease in intensity ratio, I_D / I_G, indicates a reduction in sp^3 content and corresponds to a decrease in the film quality. Despite the pressure fluctuations during these experiments, the results are consistent with the findings reported in the literature, as discussed previously. In this case, the quality and growth rate of diamond films are primarily influenced by variations in methane concentration rather than pressure.

Similar to previous experiments (see Sections 5.2.3 and 5.2.4), the films exhibited compressive stress. Since the remaining experiments using 2.0 vol.%, 2.5 vol.%, and 3.0 vol.% methane concentrations could not be performed, the literature provides valuable insights into the expected outcomes of these unperformed experiments. A continuing trend of decreasing film quality with increasing methane concentration is expected, eventually accompanied by a decrease in grain size and an increase in grain boundaries. At higher methane concentrations, the low [H] / [CH_3] concentration ratio will result in ineffective etching of the non-diamond phase. This increases nucleation, and will further intensify the secondary nucleation, resulting in films with smaller grain sizes, smoother surface morphology, and a higher degree of sp^2 carbon content [66, 69]. A similar surface morphology was observed in some of the spare samples that were synthesized at methane concentrations of 2.0 vol.% and 3.0 vol.%. The reader is referred to Appendix C2. Diamond films obtained using higher methane concentrations (2.0 vol.% and 3.0 vol.%) for more details.

5.3 Clamping device

The last part of this thesis project includes the design of a new clamping device that should keep the filaments straight during the deposition process. This chapter outlines the boundary conditions, conceptualization, and designs of the new clamping device.

5.3.1 Boundary conditions and functional requirements

The new clamping mechanism must meet certain boundary conditions. Adjustments to the HF-CVD setup can be both expensive and time-consuming. Therefore, it is essential that the clamping mechanism is compatible with the existing HF-CVD setup and is engineered accordingly. The requirements set for the clamping device are as follows:

- The clamping device must withstand the high temperatures and reactive environment inside the chamber during the deposition process without degrading or causing contamination. Especially when multiple W filaments are used, the operating temperatures in the proximity of the filaments will be significantly higher.
- The clamping mechanism must fit within the HF-CVD setup. The maximum width of the mechanism should be smaller than the 145-mm inner diameter of the front flange (see Figure 4.1). The left and right electrodes of the clamping mechanism should fit on the underlying copper electrodes to ensure fixation and electrical contact. The copper electrodes are mounted at a center distance of 114 mm from each other and have a diameter of 12.7 mm.
- The heater stage should fit within the available space between the electrodes of the clamping mechanism.
- The filaments should be securely held in place during the deposition process to prevent filament movement and ensure steady electrical contact.
- The clamping mechanism should be user-friendly, allowing for easy insertion and removal of the filaments. A simple, compact, and effective solution is desired since complex designs may be difficult to manufacture or require excessive investment.

The new clamping mechanism needs to satisfy several functional requirements. Its primary purpose is to keep multiple filaments straight during the deposition process while ensuring their lifespan is not compromised. In existing mechanisms, a (small) tensile force is usually applied to the filaments to maintain their straightness (see Appendix A2. Tensioning mechanisms). This approach is typically used to compensate for the thermal and carburization elongation (~20%) of the filaments (see Section 2.3.3). The functional requirements are listed below:

- The force delivered by the clamping mechanism should be adjustable since the required force to keep the filaments straight will be determined experimentally.
- The elongation is estimated to be around 16 mm, based on the assumption that 80 mm of the filament is actively heated between the electrodes and will experience 20% elongation. The clamping mechanism should be able to cope with this elongation.
- While exerting a tensile force on the filaments, the clamping mechanism must ensure that the filaments maintain steady electrical contact with the electrodes.
- Any movable parts of the clamping mechanism must not come into contact with the sidewalls or other parts of the HF-CVD setup, as this could induce a short circuit.

5.3.2 Material selection

The materials selected for the components of the clamping mechanism are made of high-temperature-resistant materials. Since the materials used in the original clamping mechanism (see Figure 4.2) performed well during this project, the same materials were selected for the new clamping mechanism designs (concept 1 and concept 2). In particular, the components of the original clamping mechanism are made of molybdenum (melting point 2623 °C) and alumina (melting point 2072 °C). The parts that are conductive are made out of molybdenum (Mo), while alumina (Al_2O_3) is used for the insulating parts. Table 5.7 provides an overview of the materials used for the components in both the original and new clamping mechanism designs. The electrodes, circular guide electrode, screws, and insulator bridges used in the original design are intended to be reused in concepts 1 and 2 and are denoted by *.

Table 5.7: Overview of the materials used for the components in the original and new clamping mechanism designs (concepts 1 and 2)

Clamping mechanism	Design:	Component	Material
Original design	Original	Electrodes*	Mo
	Original	Circular guide electrode*	Mo
	Original	Screws*	Mo
	Original	Weights	Mo
	Original	Fixation plate	Mo
	Original	Insulator bridge*	Al_2O_3
New designs (additional components)	Concept 1	Rotating leg	Mo
	Concept 1	Connecting segment	Mo
	Concept 1	Rotation axis	Mo
	Concept 1	Limiter	Al_2O_3
	Concept 2	Filament support	ZrO_2
	Concept 2	Insulator bridge (modified)	Al_2O_3

*: Components of the original clamping device that will be reused in concept 1 and concept 2

5.3.3 Conceptualization

The conditions inside the deposition chamber can be simulated using computational fluid dynamics (CFD) simulations. This can help optimize and predict the performance of the system before conducting actual experiments. The CFD simulations involve modeling the fluid flow, heat transfer, and chemical reactions inside the chamber using numerical methods and can provide insights into the distribution of species and temperature inside the deposition chamber. However, since this thesis project was initiated and integrally scheduled as an experimental research program, no simulations were performed and no simulation data was available for this setup. Consequently, a conceptual approach was used for the designs of the clamping mechanism.

Reported clamping mechanisms use heat-resistant springs or counterweights to apply a tensile force to the filaments. To select heat-resistant springs, a detailed analysis of the temperature distribution inside the chamber is necessary, as the performance of these springs is often limited by their maximum service temperature. Moreover, prolonged exposure to high temperatures and environmental factors, such as chemical exposure, can potentially cause degradation over time, which may affect the overall performance and reliability of the springs. A design using heat-resistant counterweights typically offers a lower risk of performance degradation that is caused by prolonged exposure to high temperatures or environmental factors. For this reason, heat-resistant counterweights are proposed for the new design.
The new clamping device, illustrated in Figure 5.22, includes some modifications and additional components as compared to the original design. The boundary conditions and the functional requirements mentioned previously were taken into account for this design.

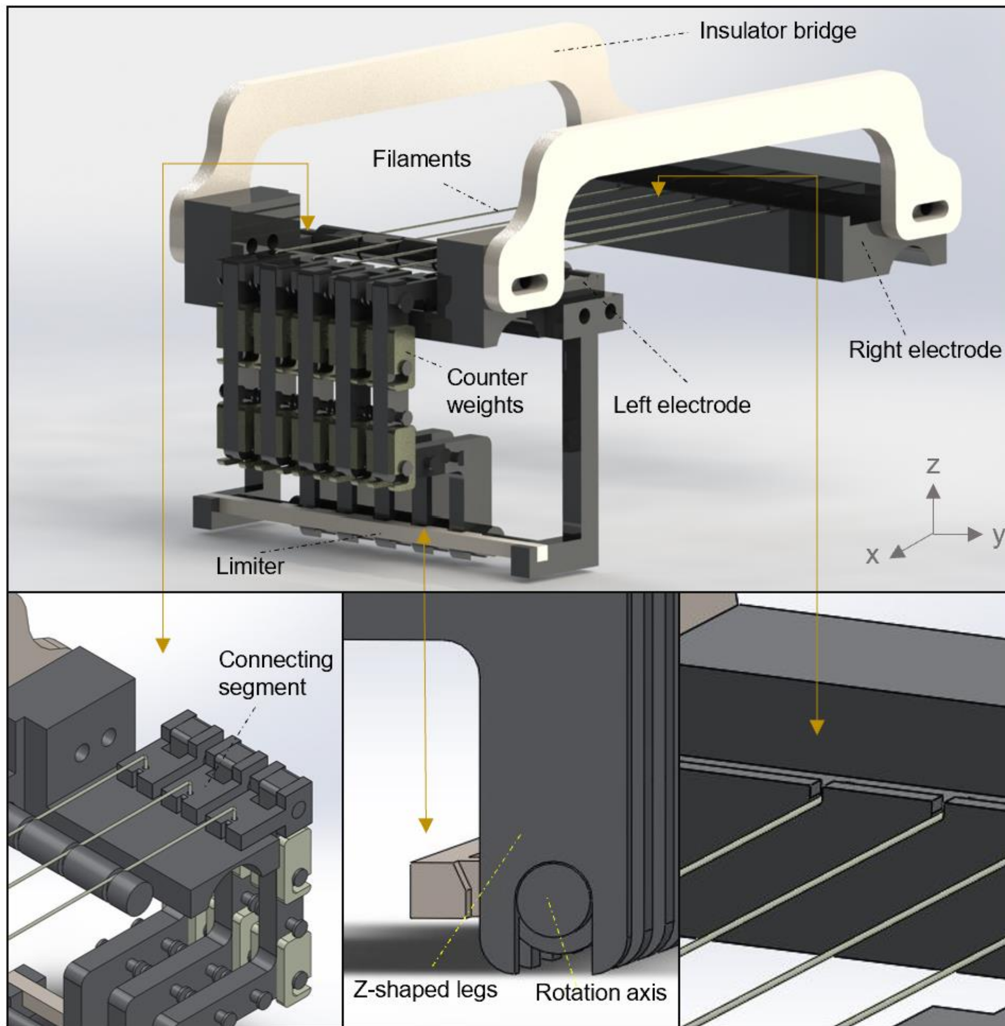

Figure 5.22: Design of new clamping device (concept 1) with close-ups of different components

This clamping device consists of a pair of molybdenum electrodes, insulator bridges, a rod-shaped guide electrode, a rotation axis, a limiter, Z-shaped legs, connecting segments, and counterweights. The electrodes have different dimensions as compared to the original design. The left electrode is extended in the z-direction, enabling the placement of the rotation axis and limiter. The rotation axis consists of multiple slots where Z-shaped legs can be positioned and rotated. These legs contain pins that can support the counterweights, which generate a moment around the rotation axis, and as a result, a tensile force is exerted on the filament. Connecting segments are attached to the top end of the Z-shaped legs, which connect the filaments to the legs. The rotation of the Z-shaped legs is restricted to a rotation angle of 25° to avoid any contact with the sidewall. The limiter also serves as a guide to prevent any contact between the Z-shaped legs, ensuring safe and reliable operation.

The dimensions of the components in the new clamping device have been carefully selected. In the previous design, some dimensions were chosen arbitrarily, which could potentially affect the diamond synthesis process. For instance, the original design allowed the use of seven filaments with a spacing of 7 mm between the filaments, while the new design opted for five filaments with a spacing of 10 mm between the filaments (see Figure 5.23). The spacing distance is selected based on existing optimization studies performed on uniform temperature distribution at the substrate level [70].

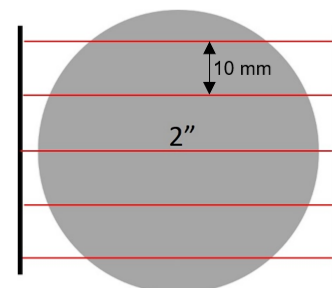

Figure 5.23: Schematic top view filament arrangement

The dimensions of the rotating leg (see Figure 5.24) are based on the minimum required displacement of 16 mm to take up the estimated elongation of the filaments. The distance between the rotation axis of the leg and the connecting segment is fixed at 50 mm, based on a rotation angle of 20°. For ease of manufacturing, rounded values were used, with an added margin of safety to ensure that the minimum displacement of 16 mm is achieved on the outer end. A small rotation angle and a relatively large distance were selected to minimize the curvature of the filament.

The width of the Z-shaped leg is 30 mm, and the maximum lever arm is 23 mm. By attaching the counterweights to the pins at different arm lengths (*x*) or by placing multiple counterweights on the pins simultaneously (e.g., at $x = 23$ mm), the moment and the resulting tensile force can be adjusted. The force *F* (*N*) exerted on the filament can be determined using the following equation:

$$F = \frac{Gx_G + \sum 2m_n x_n g}{50\ E{-}3} \qquad \text{(Eq. 5.2)}$$

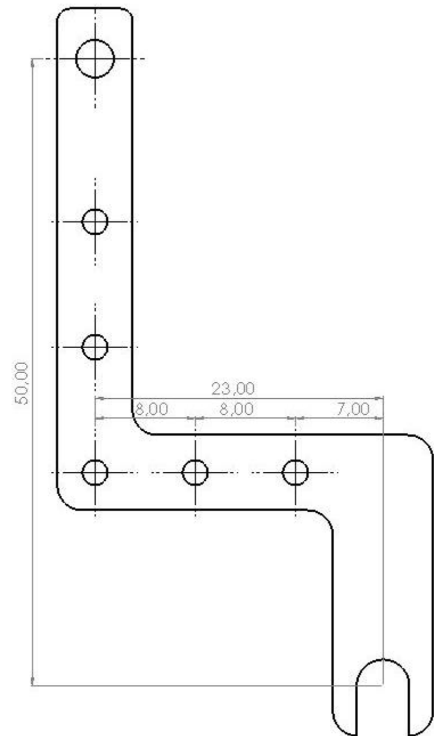

Figure 5.24: Dimensions of the Z-shaped leg (values in mm)

This equation involves several parameters, where *m* represents the mass of the counterweights *m* (*kg*) used on each side of the leg, and the arm length is denoted by *x* (*m*). The index letter *n* indicates the counterweights to the corresponding arm lengths. To prevent any unbalanced rotation, a pair of counterweights (i.e., on each side of the Z-shaped leg) are used, resulting in *m* being multiplied by 2. The weight is determined by multiplying *m* by the gravitational acceleration *g* (ms^{-2}). The respective moments can be determined by multiplying the weight by the corresponding arm length x_n. The moments exerted by the counterweights are summed up with the moment exerted by the rotating structure's weight *G* (*N*) located at x_G. The resulting total moment is divided by the distance between the rotation axis and connecting segment to determine the total tensile force exerted on the filament. A schematic representation of the two extremes in filament positioning (i.e., unstretched and maximum elongation) along with the force balance is given in Figure 5.25.

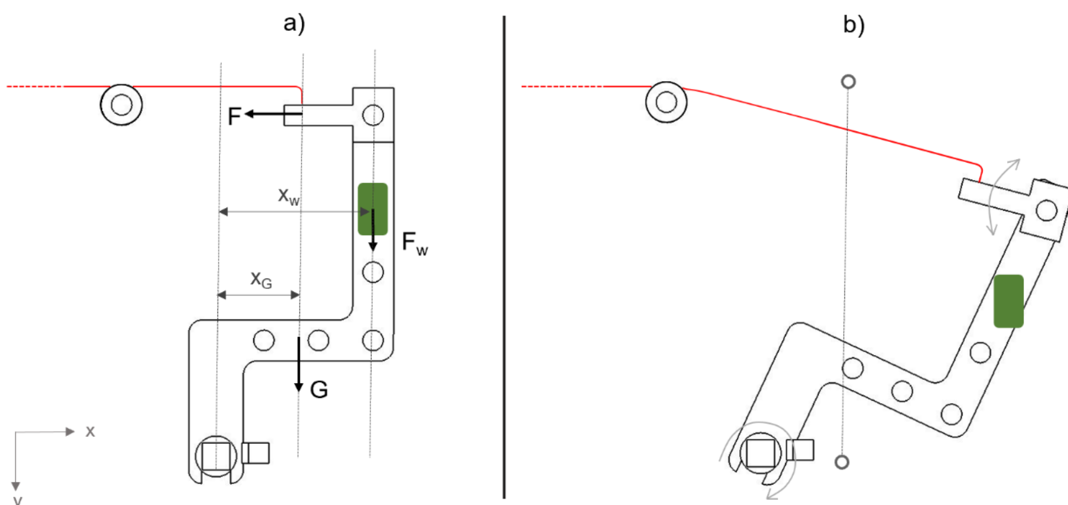

Figure 5.25: Schematic representation of a) initial stage (filament unstretched) and b) maximum rotated stage (filament fully elongated) of the Z-shaped leg

To prevent the rotating components from blocking due to heat expansion at the operating temperatures, a 0.2-mm spacing was used between the components.

The use of additional components increases the complexity in terms of manufacturability and usability. Therefore, a simpler and more straightforward solution, referred to as concept 2, was considered (see Figure 5.26). In this design, an additional ceramic support consisting of five arc-shaped slots is included in the middle of the clamping device in order to reduce filament sagging. This support has a thickness of a few mm and is made out of zirconia (melting temperature > 2500 °C). The thickness of the support should be as low as possible to avoid the obstruction of filament radiation, which could cause a shadow effect on the substrate surface and as a result, affect the growth process. However, the thickness should also be sufficient to dissipate the heat generated by the filaments.

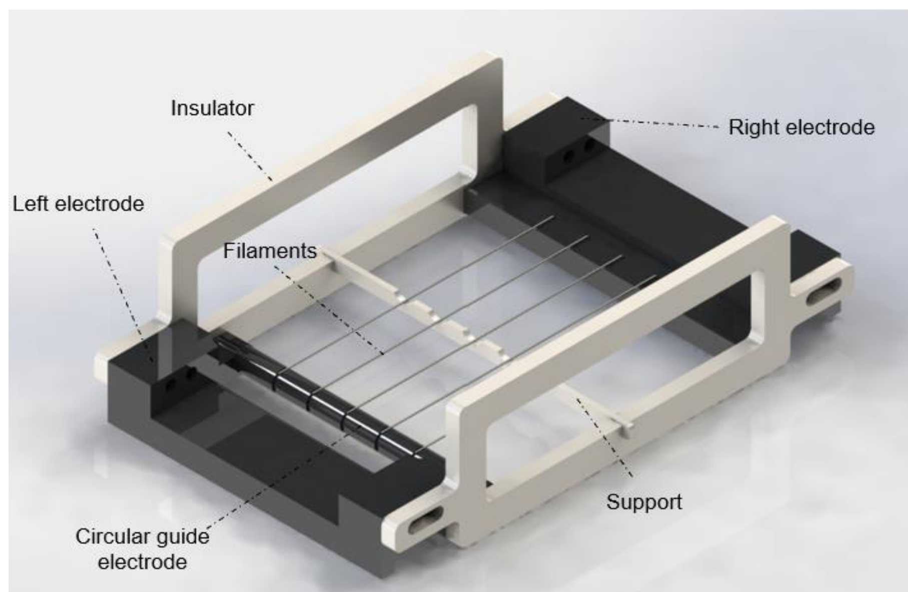

Figure 5.26: Design of new clamping device (concept 2)

The proposed designs required the production of additional components. However, due to extended waiting time at the manufacturer and the detected system leakages, these components could not be realized and tested within the designated timeline of this thesis project. Nevertheless, a 3D-printed prototype of the new clamping device design (concept 1) was used to evaluate its compatibility with the existing HF-CVD setup (for more details, see Appendix C3. 3D printed prototype (Concept 1)).

6. Conclusions and recommendations for future work

6.1 Conclusions

The aim of this MSc. thesis project was to enable diamond growth in the new HF-CVD setup. Several steps were taken in order to achieve this. This project was divided into three main research activities in sequential order. The first step was to prolong the lifespan of the filaments, as this allows the formation of reactive species from the chemical precursors needed for diamond growth. Next, a growth study was performed to investigate the effects of various deposition parameters (filament-substrate distance, stage temperature, and methane concentrations) on the morphology and quality of diamond films. Lastly, preliminary concept designs for the clamping mechanism to maintain straight filaments during the deposition process are proposed.

Different placements of the W filaments were tested within the original clamping device, and it was found that resting the filament on both electrodes proved to be the most effective approach to maximize the lifespan of the filaments. In this configuration, the filaments can be used for multiple interrupted deposition runs, and even after 162 hours of usage, the filaments remained intact. Furthermore, the carburization of the filaments was monitored, and the results showed a similar response to that found in the literature. The methane concentration significantly affected the carburization rate. The average carburization time required to reach a constant filament power consumption, which is required to initiate the diamond synthesis process, was ~8 hours when using 0.5 vol.% methane and ~5 hours when using 1.0 vol.%.

The growth study revealed that dense polycrystalline diamond films can be synthesized in this HF-CVD setup with growth rates ranging from ~50 nm/h to ~300 nm/h in the investigated range of deposition parameters (i.e., 360 °C to 780 °C). At small filament-substrate distances, high-quality diamond films were synthesized at considerably high growth rates, while increasing the filament-substrate distance resulted in lower-quality diamond films at lower growth rates. The second parameter study showed that an increase in stage temperature resulted in higher growth rates. However, contrary to the expected improvement in film quality with increasing stage temperatures as reported in the literature, the highest and lowest film quality (in terms of Raman spectral I_D/I_G ratio) were obtained at stage temperatures of 450 °C and 720 °C, respectively. This inconsistency in film quality can be related to the unintentional presence of pressure fluctuations during the experiments conducted between 360 °C and 630 °C, caused by gradual malfunctioning of the vacuum seal associated with the heater stage. Pressure variations had a more pronounced impact on the growth rate and film quality than changes in stage temperature.
Finally, the effect of methane concentration on diamond growth was investigated. An increase in methane concentration from 0.5 vol.% to 1.0 vol.% methane led to higher growth rates and initially larger diamond grain sizes, primarily due to the increased methyl radical concentration at the substrate level. The highest-quality diamond films were obtained, however, at a methane concentration of 0.5 vol.%, while the overall film quality decreased with increasing methane concentration. Despite the pressure fluctuations during these experiments, the results were consistent with the findings reported in the literature. Among the investigated parameters, the growth rate and film quality exhibited the highest sensitivity to changes in methane concentration.

Based on the experimental results, new designs for the clamping device were proposed to ensure the straightness of the filaments during the deposition process. In the first concept, a rotating Z-shaped structure, which is equipped with counterweights, generates a moment around the rotation axis, and as a result, a tensile force is exerted on the filaments. In the

second concept, a ceramic support in the middle of the clamping device is used to reduce the sagging of the filaments. However, due to system leaks and extended waiting times at the manufacturer, the implementation and testing of these designs were not feasible within the timeline of the project.

6.2 Recommendations for future work

HF-CVD has proven to be a promising technique to synthesize polycrystalline diamond films. The successful extension of the filament lifetime and subsequent successful growth of polycrystalline diamond films in the new HF-CVD setup are major milestones in reactor optimization and have opened the doors for other researchers to perform their own growth experiments. Over the course of this thesis project, unexpected events unfolded, leaving certain aspects unfinished. In addition, as a first user, it was not feasible to complete all activities of interest within the timeline of this thesis project. Therefore, the recommendations for future work are listed below:

- Scaling up the area of diamond growth: The use of multiple straight filaments has not yet been tested. Various upgrades to the HF-CVD setup were required to prepare the reactor for these experiments. Future work could involve conducting experiments using multiple filaments, which are placed according to approach D, where the filaments rest on both electrodes. The scaling-up process will provide valuable insights on various aspects, including the simultaneous carburization of multiple filaments, the optimal current and total gas flow required to carburize the filaments at an acceptable rate, and the effects of filament temperature on the overall growth process (e.g., uniformity of diamond deposition across 2” wafers).
- Growth study: For future work, it is recommended to perform a similar growth study as was done in this research, with a specific focus on the pending experiments at methane concentrations of ≥ 2.0 vol.%. Additionally, scaling up the HF-CVD process using multiple filaments opens the possibility of growing diamond films on larger substrates, such as 2” seeded Si wafers. To enhance the experimental conditions, it is advised to equip the HF-CVD setup with a pressure controller unit. This will enable to investigate the isolated effects of various other parameters on diamond film growth. The pressure controller will also allow to study the isolated effect of pressure on diamond growth. Additionally, other critical parameters such as gas composition, total gas flow, and the effect of a rotating or stationary stage should be investigated to gain a comprehensive understanding of their impact on diamond growth. Of particular interest is the use of trimethyl boron, which can be used to synthesize conductive boron-doped diamond (BDD) films suitable for electrochemical (sensing) applications.
- Implementing and testing proposed clamping device designs: Sagging of the filaments is expected over time. To limit this undesired effect, testing of the new clamping device(s) is recommended. Especially the second concept could easily be manufactured, as it only requires extra ceramic parts that could be laser cut.
- Computational simulation of the HF-CVD setup: A detailed computational simulation could be performed to optimize and predict the overall performance of the HF-CVD system. The computational fluid dynamics (CFD) simulations involve modeling the fluid flow, heat transfer, and chemical reactions inside the chamber using numerical methods and can provide insights into the distribution of species and temperature inside the deposition chamber. From this, optimal growth conditions for diamond synthesis can be established. Furthermore, with a detailed understanding of the operating conditions within the reactor, it becomes possible to establish the precise boundary conditions for the clamping device, which could be engineered accordingly.

7. Bibliography

1. May PW (2000) Diamond thin films: a 21st-century material. Philosophical Transactions of the Royal Society of London Series A: Mathematical, Physical and Engineering Sciences 358:473–495. https://doi.org/10.1098/rsta.2000.0542

2. Haubner R (2021) Low-pressure diamond: from the unbelievable to technical products. ChemTexts 7:10. https://doi.org/10.1007/s40828-021-00136-z

3. Auciello O, Aslam DM (2021) Review on advances in microcrystalline, nanocrystalline and ultrananocrystalline diamond films-based micro/nano-electromechanical systems technologies. J Mater Sci 56:7171–7230. https://doi.org/10.1007/s10853-020-05699-9

4. Li G, Rahim MZ, Pan W, et al (2020) The manufacturing and the application of polycrystalline diamond tools – A comprehensive review. Journal of Manufacturing Processes 56:400–416. https://doi.org/10.1016/j.jmapro.2020.05.010

5. Lux B, Haubner R (1998) CVD diamond for cutting tools. In Low-Pressure Synthetic Diamond. Springer, Berlin, Heidelberg 223–242

6. Gicquel A, Hassouni K, Silva F, Achard J (2001) CVD diamond films: from growth to applications. Current Applied Physics 1:479–496. https://doi.org/10.1016/S1567-1739(01)00061-X

7. Tang L, Tsai C, Gerberich WW, et al (1995) Biocompatibility of chemical-vapour-deposited diamond. Biomaterials 16:483–488. https://doi.org/10.1016/0142-9612(95)98822-V

8. Nagasaka H, Teranishi Y, Kondo Y, et al (2016) Growth Rate and Electrochemical Properties of Boron-Doped Diamond Films Prepared by Hot-Filament Chemical Vapor Deposition Methods. e-J Surf Sci Nanotech 14:53–58. https://doi.org/10.1380/ejssnt.2016.53

9. Herlinger J (2006) sp3’s experience using hot filament CVD reactors to grow diamond for an expanding set of applications. Thin Solid Films 501:65–69. https://doi.org/10.1016/j.tsf.2005.07.108

10. Haubner R, Lux B (1993) Diamond growth by hot-filament chemical vapor deposition: state of the art. Diamond and Related Materials 2:1277–1294. https://doi.org/10.1016/0925-9635(93)90008-P

11. Vector Illustration S P Atomic Orbitals: stockvector (rechtenvrij) 1916336144. In: Shutterstock. https://www.shutterstock.com/nl/image-vector/vector-illustration-s-p-atomic-orbitals-1916336144. Accessed 14 Apr 2023

12. Flowers P, Theopold K (2019) Advanced Theories of Covalent Bonding (Chemistry)

13. (2022) (Allotropes Of Carbon). In: Infinity Learn. https://infinitylearn.com/surge/blog/iit-jee/allotropes-of-carbon/. Accessed 14 Apr 2023

14. S Tong Lee, Lin Z, Jiang X (1999) PII: S0927-796X(99)00003-0 | Elsevier Enhanced Reader. CVD diamond films: nucleation and growth. https://doi.org/10.1016/S0927-796X(99)00003-0

15. Bundy FP (1980) The *P* , *T* phase and reaction diagram for elemental carbon, 1979. J Geophys Res 85:6930. https://doi.org/10.1029/JB085iB12p06930

16. Moseley PT, Rand DAJ, Davidson A, Monahov B (2018) Understanding the functions of carbon in the negative active-mass of the lead–acid battery: A review of progress. Journal of Energy Storage 19:272–290. https://doi.org/10.1016/j.est.2018.08.003

17. Palyanov YN, Kupriyanov IN, Khokhryakov AF, Borzdov YM (2017) High-pressure crystallization and properties of diamond from magnesium-based catalysts. CrystEngComm 19:4459–4475. https://doi.org/10.1039/C7CE01083D

18. Okoli S, Haubner R, Lux B (1991) INFLUENCE OF THE FILAMENT MATERIAL ON LOW-PRESSURE HOT-FILAMENT CVD DIAMOND DEPOSITION. J Phys IV France 02:C2-923-C2-930. https://doi.org/10.1051/jp4:19912111

19. Kromka A, Babchenko O, Izak T, et al (2012) Linear antenna microwave plasma CVD deposition of diamond films over large areas. Vacuum 86:776–779. https://doi.org/10.1016/j.vacuum.2011.07.008

20. Kromka A, Balon F, Daniš T, et al (2003) Influence of Substrate Bias Pretreatment on Growth of Diamond Films By HFCVD. Surface Engineering 19:417–420. https://doi.org/10.1179/026708403225010073

21. Gracio JJ, Fan QH, Madaleno JC (2010) Diamond growth by chemical vapour deposition. J Phys D: Appl Phys 43:374017. https://doi.org/10.1088/0022-3727/43/37/374017

22. Chandran M (2019) Synthesis, Characterization, and Applications of Diamond Films. In: Carbon-Based Nanofillers and Their Rubber Nanocomposites. Elsevier, pp 183–224

23. Liu H, Dandy DS (1995) Studies on nucleation process in diamond CVD: an overview of recent developments. Diamond and Related Materials 4:1173–1188. https://doi.org/10.1016/0925-9635(96)00297-2

24. Tsigkourakos M, Hantschel T, Janssens SD, et al (2012) Spin-seeding approach for diamond growth on large area silicon-wafer substrates: Spin-seeding approach for diamond growth on large area Si. Phys Status Solidi A 209:1659–1663. https://doi.org/10.1002/pssa.201200137

25. Diamond cutting tools - CUTS DIAMANT - Italy – Diamond blades, core bits, joint cutters, floor saws, table saw, Cut-off saws, wall-chasers, walk-behind saw, diamond discs. https://www.cutsdiamant.com/en/diamond-core-bits-for-dry-and-wet-drilling. Accessed 14 Apr 2023

26. Bennet KE, Tomshine JR, Min H-K, et al (2016) A Diamond-Based Electrode for Detection of Neurochemicals in the Human Brain. Front Hum Neurosci 10:. https://doi.org/10.3389/fnhum.2016.00102

27. Moustakas T (1989) The role of the tungsten filament in the growth of polycrystalline diamond films by filament-assisted CVD of hydrocarbons. Solid State Ionics 32–33:861–868. https://doi.org/10.1016/0167-2738(89)90368-8

28. Matsubara H, Sakuma T (1990) Diamond deposition on cemented carbide by chemical vapour deposition using a tantalum filament. J Mater Sci 25:4472–4476. https://doi.org/10.1007/BF00581110

29. Sommer M, Smith FW (1990) Activity of tungsten and rhenium filaments in CH_4/H_2 and C_2H_2/H_2 mixtures: Importance for diamond CVD. J Mater Res 5:2433–2440. https://doi.org/10.1557/JMR.1990.2433

30. Okoli S, Haubner R, Lux B (1991) Carburization of tungsten and tantalum filaments during low-pressure diamond deposition. Surface and Coatings Technology 47:585–599. https://doi.org/10.1016/0257-8972(91)90329-U

31. Kweon D-W, Lee J-Y (1992) The effect of the change in filament characteristics on diamond growth in hot filament chemical vapor deposition. Materials Research Bulletin 27:783–791. https://doi.org/10.1016/0025-5408(92)90087-G

32. Mehta Menon P, Edwards A, Feigerle CS, et al (1999) Filament metal contamination and Raman spectra of hot filament chemical vapor deposited diamond films. Diamond and Related Materials 8:101–109. https://doi.org/10.1016/S0925-9635(98)00444-0

33. Kromka A, Janik A, Satka A, et al (2002) Investigation of carburisation of tungsten-carbide formation by hot-filament CVD technique.

34. Zeiler E, Schwarz S, Rosiwal SM, Singer RF (2002) Structural changes of tungsten heating filaments during CVD of diamond. Materials Science and Engineering: A 335:236–245. https://doi.org/10.1016/S0921-5093(01)01933-5

35. Li DM, Ma¨ntyla¨ T, Hernberg R, Levoska J (1996) Diamond deposition by coiled and grid filaments using high methane concentrations. Diamond and Related Materials 5:350–353. https://doi.org/10.1016/0925-9635(95)00358-4

36. Tsutsumoto T (1998) Improvement of Ta filament for diamond CVD. Thin Solid Films 317:371–375. https://doi.org/10.1016/S0040-6090(97)00626-3

37. Jansen F, Machonkin MA, Kuhman DE (1990) The deposition of diamond films by filament techniques. Journal of Vacuum Science & Technology A: Vacuum, Surfaces, and Films 8:3785–3790. https://doi.org/10.1116/1.576494

38. (2011) Granta Design Limited - CES EduPack

39. ASM Handbook Committee (1990) Properties and Selection: Nonferrous Alloys and Special-Purpose Materials. ASM International

40. Hörz G, Lindenmaier K (1974) The kinetics and mechanisms of the absorption of carbon by niobium and tantalum in a methane or acetylene stream. Journal of the Less Common Metals 35:85–95. https://doi.org/10.1016/0022-5088(74)90148-9

41. Clausing RE, Horton LL, Angus JC, Koidl P (1991) Diamond and Diamond-like Films and Coatings. Springer US, Boston, MA

42. Davidson CF, Alexander GB, Wadsworth ME (1979) Catalytic effect of cobalt on the carburization kinetics of tungsten. MTA 10:1059–1069. https://doi.org/10.1007/BF02811652

43. Lassner E, Schubert W-D (1999) Tungsten: Properties, Chemistry, Technology of the Element, Alloys, and Chemical Compounds. Springer US, Boston, MA

44. Dischler B, Wild C (1998) Low-Pressure Synthetic Diamond: Manufacturing and Applications. Springer Berlin Heidelberg, Berlin, Heidelberg

45. Ashby MF, Shercliff H, Cebon D (2014) Materials: engineering, science, processing and design, Third edition, North American edition. Elsevier Butterworth-Heinemann, Amsterdam ; Boston ; Heidelberg ; London

46. Yoshimura Y, Kawarada H (1994) Sagging of tungsten filaments in hot filament chemical vapor deposition of diamond films. 1994 Diamond and Related Materials:

47. Wang Q (2005) Combinatorial approach to studying tungsten filament ageing in fabricating hydrogenated amorphous silicon using the hot-wire chemical vapour deposition technique. Meas Sci Technol 16:162–166. https://doi.org/10.1088/0957-0233/16/1/021

48. Akgul M, Schneider R, Ren Z, et al (2011) Hot filament CVD conductive microcrystalline diamond for high Q, high acoustic velocity micromechanical resonators. In: 2011 Joint Conference of the IEEE International Frequency Control and the European Frequency and Time Forum (FCS) Proceedings. IEEE, San Francisco, CA, USA, pp 1–6

49. Kondoh E, Ohta T, Mitomo T, Ohtsuka K (1992) Experimental and calculational study on diamond growth by an advanced hot filament chemical vapor deposition method. Journal of Applied Physics 72:705–711. https://doi.org/10.1063/1.351856

50. James Studies of H atoms and CH3 radical species in a HF-CVD reactor. Bristol University

51. Kondoh E, Tanaka K, Ohta T (1993) Reactive-flow simulation of the hot-filament chemical-vapor deposition of diamond. Journal of Applied Physics 74:4513–4520. https://doi.org/10.1063/1.354368

52. Wei Q, Ashfold MNR, Mankelevich YuA, et al (2011) Diamond growth on WC-Co substrates by hot filament chemical vapor deposition: Effect of filament–substrate separation. Diamond and Related Materials 20:641–650. https://doi.org/10.1016/j.diamond.2011.02.017

53. Schäfer L, Sattler M, Klages C-P (1991) Upscaling of the Hot-Filament CVD Process for Deposition of Diamond Films on Large-Area Substrates. In: Materials Science Monographs. Elsevier, pp 453–460

54. Haubner R, Okoli S, Lux B (1992) The importance of the substrate surface temperature and other parameters in hot-filament diamond synthesis. International Journal of Refractory Metals and Hard Materials 11:259–269. https://doi.org/10.1016/0263-4368(92)90052-4

55. Wolden C, Mitra S, Gleason KK (1992) Radiative heat transfer in hot-filament chemical vapor deposition diamond reactors. Journal of Applied Physics 72:3750–3758. https://doi.org/10.1063/1.352295

56. Alcantar-Peña JJ, Montes J, Arellano-Jimenez MJ, et al (2016) Low temperature hot filament chemical vapor deposition of Ultrananocrystalline Diamond films with tunable sheet resistance for electronic power devices. Diamond and Related Materials 69:207–213. https://doi.org/10.1016/j.diamond.2016.09.007

57. Prawer S, Nemanich RJ (2004) Raman spectroscopy of diamond and doped diamond. Philosophical Transactions of the Royal Society of London Series A: Mathematical, Physical and Engineering Sciences 362:2537–2565. https://doi.org/10.1098/rsta.2004.1451

58. Merlen A, Buijnsters J, Pardanaud C (2017) A Guide to and Review of the Use of Multiwavelength Raman Spectroscopy for Characterizing Defective Aromatic Carbon Solids: from Graphene to Amorphous Carbons. Coatings 7:153. https://doi.org/10.3390/coatings7100153

59. Paprocki K, Dittmar-Wituski A, Trzciński M, et al (2019) The comparative studies of HF CVD diamond films by Raman and XPS spectroscopies. Optical Materials 95:109251. https://doi.org/10.1016/j.optmat.2019.109251

60. Dychalska A, Popielarski P, Franków W, et al (2015) Study of CVD diamond layers with amorphous carbon admixture by Raman scattering spectroscopy. Materials Science-Poland 33:799–805. https://doi.org/10.1515/msp-2015-0067

61. Salgueiredo E, Amaral M, Neto MA, et al (2011) HFCVD diamond deposition parameters optimized by a Taguchi Matrix. Vacuum 85:701–704. https://doi.org/10.1016/j.vacuum.2010.10.010

62. Ahmed R, Siddique A, Saha R, et al (2020) Effect of precursor stoichiometry on morphology, phase purity, and texture formation of hot filament CVD diamond films grown on Si (100) substrate. J Mater Sci: Mater Electron 31:8597–8606. https://doi.org/10.1007/s10854-020-03395-7

63. Ali M, Qazi IA (2012) Effect of substrate temperature on hot-filament CVD grown diamond films at constant filament current. IJSURFSE 6:214. https://doi.org/10.1504/IJSURFSE.2012.049054

64. Ali M, Ürgen M (2012) Growth of in situ multilayer diamond films by varying substrate–filament distance in hot-filament chemical vapor deposition. J Mater Res 27:3123–3129. https://doi.org/10.1557/jmr.2012.378

65. Hao T, Zhang H, Shi C, Han G (2006) Nano-crystalline diamond films synthesized at low temperature and low pressure by hot filament chemical vapor deposition. Surface and Coatings Technology 201:801–806. https://doi.org/10.1016/j.surfcoat.2005.12.037

66. Guo L, Chen G (2007) High-quality diamond film deposition on a titanium substrate using the hot-filament chemical vapor deposition method. Diamond and Related Materials 16:1530–1540. https://doi.org/10.1016/j.diamond.2006.12.016

67. Mehta Menon P, Clausing RE, Heatherly L, Feigerle CS (1998) The morphology of diamond grown by hot filament chemical vapor deposition. Diamond and Related Materials 7:1201–1206. https://doi.org/10.1016/S0925-9635(98)00178-2

68. Ali M, Ürgen M (2011) Surface morphology, growth rate and quality of diamond films synthesized in hot filament CVD system under various methane concentrations. Applied Surface Science 257:8420–8426. https://doi.org/10.1016/j.apsusc.2011.04.097

69. Khlayboonme ST, Warawoot T (2020) Phase Transformation of Nanocrystalline Diamond Films: Effect of Methane Concentration. KEM 831:127–131. https://doi.org/10.4028/www.scientific.net/KEM.831.127

70. Wu Y, Zhang H, Yan G, et al (2021) Hot filament chemical vapor deposition temperature field optimization for diamond films deposited on silicon nitride substrates. Mater Res Express 8:116403. https://doi.org/10.1088/2053-1591/ac3278

71. Mechanism for fixing, straightening and tensioning tungsten filaments through hot filament CVD - patent - CN202337820U - China - 29/11/2011

72. Zuo D, Kun B, Xianfeng L Hot wire for diamond film growth device and electrode structure - patent - CN1844450A - 27/03/2006 - China

73. Herlinger JE, David K, Studley DK Reactor having an array of heating filaments and a filament force regulator - patent - US5997650A - 06/11/1986 - USA

74. Jinren N, Yuan Break-resistant hot filament chemical vapor deposition system in preparation of large-size BDD electrode - patent - CN103952686A - 23/05/2014 - China

8. Appendix

A. Literature review (part II)

The findings from the literature are categorized based on the following aspects:

- Filament type including the initial length (L), diameter (Ø), purity level and shape (coiled or straight geometry) of the metallic filaments.
- Pressure in the reaction chamber measured in Torr.
- Methane concentration present in the gas mixture is indicated as CH_4 (vol %).
- Temperature of the filament ($T_{filament}$) measured in °C.
- Carburization time, i.e. total time the filament is exposed to the carbon atmosphere.
- Phase transformation, i.e. the different phases formed in the filaments.
- Changes observed in the appearance of the filaments during the carburization process.

Table 8.1: Literature findings on the carburization of tungsten filaments

Reference & First author	Filament type	Pressure (Torr)	CH_4 (vol %)	$T_{filament}$ (°C)	Carburization time	Phase transformation	Observations
[27] Moustakas	Ø: 0.5 mm Straight	30	0.5 5*	1700	12 min	α-W_2C	Crack formation Volume increase Poisoning
[28] Matsubara	Ø: 0.5 mm Straight Purity: 99.85%	30	5	2200	~2 h ~4 h	W_2C + WC WC	-
[29] Sommer et al.	Ø: - Coiled Purity: 99.9%	9 - 25	1*	1900	~1 h	W_2C	Volume increase Poisoning
[30] Okoli, et al.	L: 0.5 m Ø: 0.8 mm Coiled Purity: 99.99%	10 & 40 10 & 40	0.5 & 1 0.5 & 1	2000 2000	5h 24 h	W + W_2C + WC W_2C + WC	Volume increase
[18] Okoli, et al.	L: 0.5 m Ø: 0.8 mm Coiled Purity: 99.99%	10	0.5	2000	16 h	"Partially carburized"	-
[31] Kweon et al.	Ø: 0.5 mm Coiled	20 20	0.8-1.6* 1.6 3.0*	1900 2150	7 h 10 min 30 min 7 h & 20 h 7 h	W_2C + WC W + W_2C W_2C + WC W_2C + WC	Poisoning Poisoning
[32] Menon et al.	L: 0.12 m Ø: 0.5 mm Coiled	40	0.5	1950	16 h	-	Light gray in color
[33] Kromka et al.	L: 0.12 m Ø: 0.6 mm Straight	22.5	1	1600	5 h	WC	Light gray in color Crack formation Volume increase
[34] Zeiler et al.	L: 0.112 m Ø: 0.5 mm Straight Purity: 99.8%	22.5	1	2450	$<$1 h 1 h $>$1 h 40 h	W(↓)+W_2C(↑) +WC(↑) W_2C + WC W_2C(↓) + WC(↑) WC $>>$ W_2C	12% vol exp Crack formation 8.6% vol exp

*:Filament poisoning was detected at the corresponding CH_4 concentration and/or filament temperature.

Table 8.2: Literature findings on the carburization of tantalum filaments

Reference & First author	Filament type	Pressure (Torr)	CH_4 (vol %)	$T_{filament}$ (°C)	Carburization time	Phase transformation	Observations
[28] Matsubara	Ø: 0.5 mm Straight Purity: 99.85%	30	5	2200	~1 h ~ 4 h	$Ta + Ta_2C + TaC$ TaC	-
[30] Okoli, et al.	L: 0.5 m Ø: 0.8 mm Coiled Purity: 99.85%	10 & 40	0.5 1*	2000	5 h & 24 h	$Ta + Ta_2C + TaC$	Poisoning
		10	0.5	2200	24 h 64 h	$Ta + Ta_2C + TaC$ $Ta_2C + TaC$	
		40	1*		<24 h	$Ta + Ta_2C + TaC$	Poisoning
		10 & 40	0.5 & 1	2400	5 h 24 h	$Ta + Ta_2C + TaC$ TaC	
[18] Okoli, et al.	L: 0.5 m Ø: 0.8 mm Coiled Purity: 99.85%	10	0.5	2200	14 h	$Ta + Ta_2C + TaC$	Volume increase
[32] Menon et al.	L: 0.12 m Ø: 0.5 mm Coiled	40	0.5	1950 2380	16 h 16 h	- TaC	- Golden yellow color
[35] Li et al.	Ø: 0.5 mm (a) Coiled (b) Straight	-	6 12	~2000 2400 (a) 2890 (b)	2 h	TaC	-
[36] Tsutsumato	L: 0.101m Ø: 0.5 mm Straight	30	0.5	~2500	22 min 60 min	$Ta_2C + TaC$ TaC	Volume increase
			1		14 min 30 min	$Ta_2C + TaC$ TaC	
			3		14 min 25 min	$Ta_2C + TaC$ TaC	
			5		2 h	TaC	

*:Filament poisoning was detected at the corresponding CH_4 concentration and/or filament temperature.

A1. Tantalum filaments

Phase change

The carburization of tantalum filaments proceeds according to the following sequence:

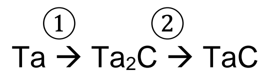

Circular metal carbide layers were formed during the carburization of tantalum filaments, and at a certain point the filament consisted of three phases, namely Ta, Ta_2C and TaC [28, 30, 36]. The SEM micrographs for a partially and fully carburized Ta filament are shown in Figure 8.1. The degree of filament carburization is dependent on the filament temperature, CH_4 concentration, and carburization time, as denoted for W filaments.

Carburization rate

The carbide-forming reaction proceeded faster in W filaments than in Ta filaments [10, 30, 32, 36]. After 24 hours of carburization (40 Torr, T_{fil} = 2000 °C, 0.5 vol.% CH_4), it was found that W filaments consisted of W_2C and WC phases, while in Ta filaments a Ta core, Ta_2C, and TaC were detected [30]. Therefore, under the same deposition conditions, Ta filaments maintained their mechanical strength much longer than W filaments, due to the presence of a metal core [44]. When Ta filaments were heated up to 2200 °C under the same deposition conditions, the carburized filament consisted of Ta_2C and TaC after 64 hours. When 5 vol.% CH_4 was used at 2200 °C for the duration of 1 hour, the Ta filaments consisted of a Ta core, Ta_2C, and TaC, and after 4 hours only TaC was present in the filament, as shown in Figure 8.1.

Mechanical stability

The growth kinetics of the carburization of Ta filaments are similar to those of W filaments [30]. However, Ta filaments showed minor deformations when heated in 5 vol% CH_4 at 2200 °C for 4 hours, while W filaments deformed severely under the same deposition conditions (see Figure 8.2) [28]. At higher temperatures (about 2800 °C), Ta filaments showed limited deformations, which makes them very suitable for high-temperature use [28]. The maximum operating temperatures for Ta filaments are reported to be around 2600 °C and for W filaments around 2000 °C – 2200 °C [28, 30]. Ta filaments are much superior to W filaments despite having a lower melting point. The melting points of Ta_2C and TaC are higher than those of W_2C and WC (see Table 8.3). Ta filaments last longer as compared to W filaments owing to the lower carburization rate and can be used for multiple cycles of diamond deposition [32, 35].

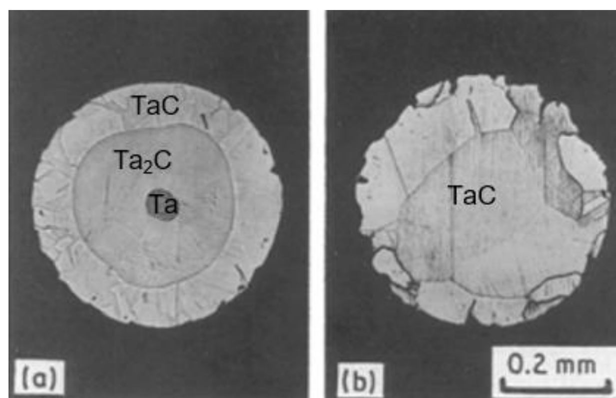

Figure 8.1: Carburization of a Ta filament after a) 1 hour and b) 4hours [28]

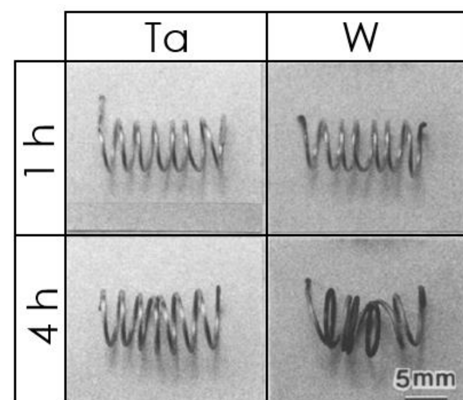

Figure 8.2: State of Ta and W filaments after 1 hour of carburization and 4h [28]

Table 8.3: Melting points of W and Ta carbides [28, 38]

Phase	Melting point (°C)	Phase	Melting point (°C)
W_2C	~2800	Ta_2C	3880
WC	2785	TaC	3985

Filament poisoning

Poisoning of Ta filaments was observed at filament temperatures of 2000 °C and 2200 °C when using a 1 vol.% CH_4 gas mixture (see Figure 8.3) [10, 30]. For this, the same reasons were given as described previously for W filaments. As circular carbide layers form on the outer shell, Ta filaments become more sensitive to surface poisoning as compared to W filaments at 2000 °C owing to the lower diffusion rates of carbon into the carbides. The diffusion coefficients of carbon in W and Ta metals and carbides are given in Table 8.4.

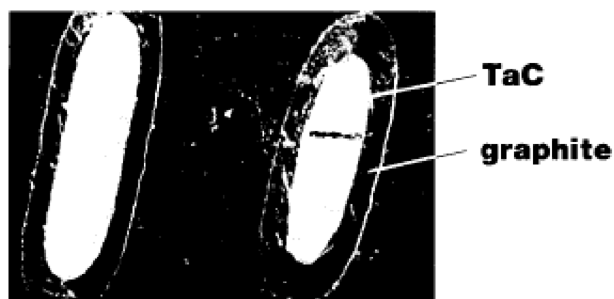

Figure 8.3: SEM micrographs showing the poisoning of Ta filaments after 16 hours of diamond deposition (1.0 vol % CH_4 and 2000 °C) [10]

Table 8.4: Diffusion coefficients for carbon [30]

Phase	Diffusion coefficient (m^2/s)
W	1×10^{-11}
W_2C	2×10^{-13}
WC	-
Ta	2×10^{-9}
Ta_2C	4×10^{-14}
TaC	2×10^{-14}

Volume expansion and crack formation

During the carburization process, Ta filaments showed an increase in volume, accompanied by the formation of large cracks along the length of the filament, as was the case for W filaments. The densities of Ta, Ta_2C, and TaC are given in Table 8.5. Okoli and coworkers have reported a total volume increase in the range of 15% - 18.8% for a carburized Ta filament [30]. Tsutsumoto revealed that the net elongation for a fully carburized filament was around 5%, the thermal elongation of 2% was excluded from the total elongation, and the average increase in diameter was about 8%, resulting in a total estimated volume increase of 22.5% [36]. The cracks become larger and wider during the first stage of carburization (see Figure 8.4a). When the carburization proceeded further, the cracks reduced in size (Figure 8.4b) due to sintering.

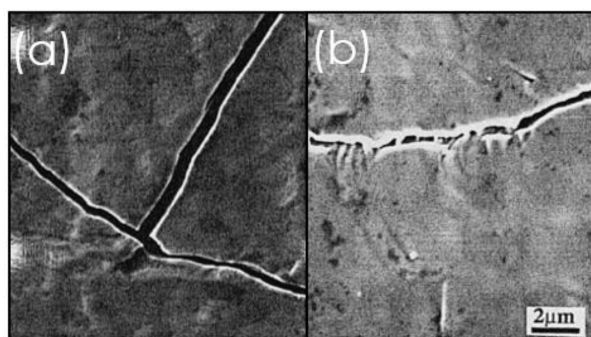

Figure 8.4: SEM images Ta filaments after a) 60 min and b) 200 min of carburization (0.5 vol % CH_4, 30 Torr, 2500 °C) [36]

Table 8.5: Density and specific resistance of tantalum phases at 25 °C [30]

Phase	Density (g/cm^3)	Specific resistance at 25 °C (µΩ cm)
Ta	16.6	12.5
Ta_2C	15.017	80
TaC	14.48	25

Bending strength

Tsutsumoto also investigated the bending strength of the carburized Ta filaments by performing several bending tests. The filament strength is strongly correlated to the formation and disappearance of the cracks. During the first stage of carburization, in which the conversion of Ta into its carbides occurred and cracks were formed, the bending strength of the Ta filament decreased significantly (see Figure 8.5). This decline persisted until Ta_2C completely vanished. At its lowest point (i.e., after 60 min), the bending strength was 2 kgf/mm^2 and the filament became very brittle. At this point, the filament consisted of only TaC and large cracks were observed, as can be seen in Figure 8.4a. As the carburization proceeded further, the bending strength showed a steady recovery to about 30 – 60 kgf/mm^2 and the cracks reduced in size (see Figure 8.4b). The embrittlement of Ta filaments can thus be overcome through full carburization of the filament.

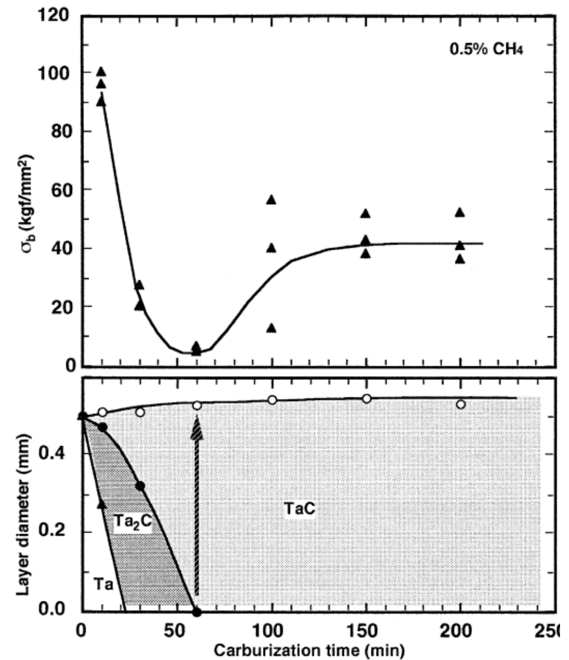

Figure 8.5: Bending strength of a Ta filament and layer diameter of the phases (Ta, Ta_2C and TaC) vs. time [36]

Electrical resistance

The electrical resistance of Ta filaments exhibited a comparable response to that of W filaments [30, 36]. At higher filament temperatures (≥ 2400 °C), the electrical resistance increased more rapidly to even greater resistance levels. After reaching its maximum resistance, a decrease in electrical resistance was noticed. The electrical resistance almost returned to its starting value when the carburization process was completed. The specific resistance values for Ta, Ta_2C, and TaC are given in Table 8.5. An increase in CH_4 concentration resulted in a slight shift of the resistance curve (electrical resistance vs. carburization time) towards the left, and a small decrease in the maximum and final resistance values was reported (see Figure 8.6), which indicates a faster carburization.

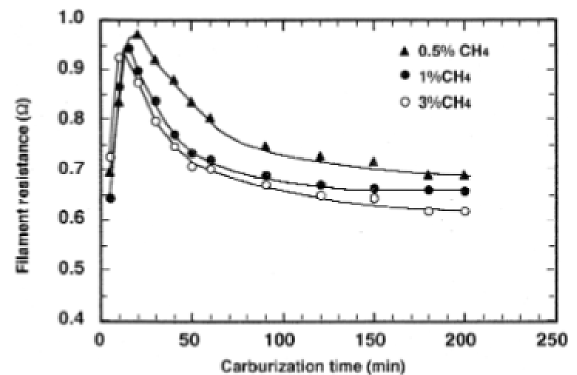

Figure 8.6: Electrical resistance (Ta) vs. carburization time at 2500 °C, 30 Torr and various CH_4 vol % [36]

A2. Tensioning mechanisms

This section provides a brief description of various clamping mechanisms employed in HF-CVD setups to maintain straight filaments during the deposition process. Typically, the filaments are clamped at one end on a fixed electrode, while the other end is connected to either a movable electrode or directly to a tensioning mechanism. In the latter, the filaments are usually directed through so-called slots to ensure reliable electrical contact before reaching the tensioning mechanism.

Suspended masses have been used to apply tension to the filament. In Figure 8.7, the filament is fixed at one end, while the other end is connected to the vertical leg of the rotatable L-shaped structure [71]. On the horizontal leg, a weight is suspended, which creates a clockwise moment around the pivot point by which tension is exerted on the filament. In Figure 8.8, a Ta wire (Ø: 0.5 mm) is fixed at one end on an electrode, while the other end is connected to a thick Ta wire (Ø: 2 mm). A weight is suspended on the other end of the thick Ta wire, and as a result, a tension of about 0.12 N is applied.

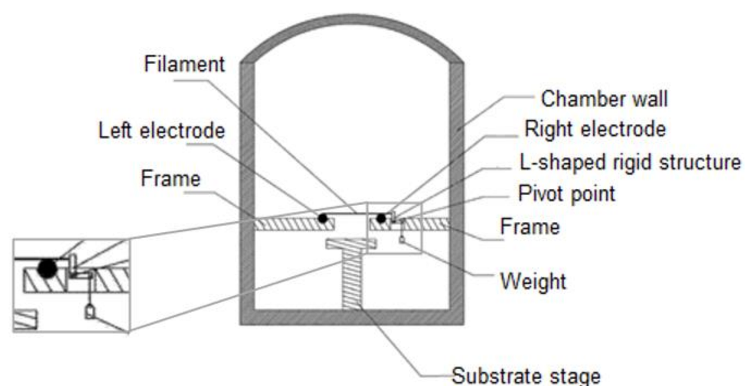

Figure 8.7: Filament tensioning mechanism by suspending a weight on a rotatable L-shaped structure [72]

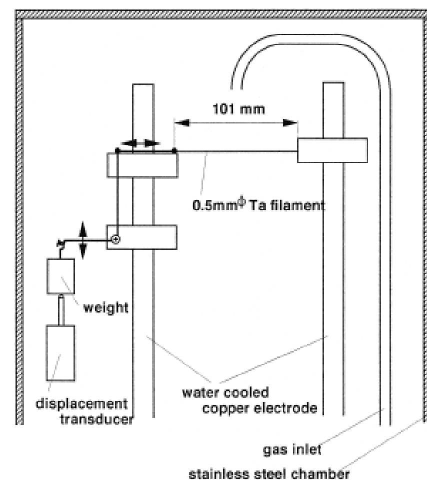

Figure 8.8: Filament tensioning mechanism in which a tension is applied by suspending a weight on the left end of Ta wire [36]

Another method to compensate for the thermal and carburization expansion of the filaments is by using tension springs. Each spring or a set of springs, depending on the mechanism and the number of filaments used, is attached at one end to a fixed frame and at the other end either to a movable electrode or directly to the filaments. The springs usually have hooks or loops on both ends and are in a pre-loaded state when used for filament tensioning.

A relatively simple design of a spring-loaded tensioning mechanism is given in Figure 8.9 [72]. A single Ta filament strip is wrapped around the electrode columns of the fixed and movable molybdenum electrodes. The movable electrode is attached to a single tension spring, which exerts a tensile force on the moving electrode and subsequently on the filament strip. The tension tends to keep the filament straight. However, its use has not been recommended by other inventors [73]. The large contact resistance of the filament will affect the overall current distribution, resulting in low electrical conductivity or unequal deformation of the filament. A loosening of the filament at the electrode columns or breakage at a single point will interrupt the diamond growth process.

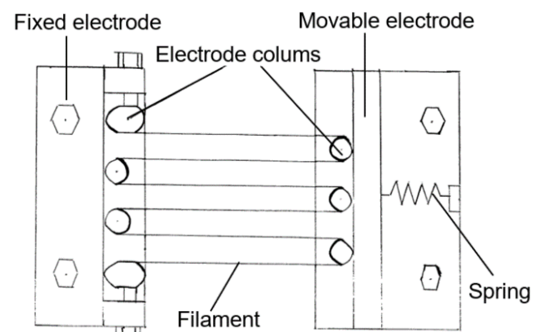

Figure 8.9: Spring-loaded tensioning mechanism. The movable electrode is connected to a pre-loaded tension spring. A filament strip is kept under tension by the pre-loaded spring [73]

A more complex design is shown in Figure 8.10 [74]. The frame, which consists of multiple subframes, is placed on top of four water-cooled molybdenum electrodes. This design allows the use of an array of filaments placed in a horizontal and/or vertical configuration. Each filament is fixed at one end to the frame, while the other end is attached to the spring. Both ends of the filaments are placed at an adjustable angle in the range of 10° - 45° with the horizontal. The tension applied to the filaments can be adjusted by changing the angle at which the springs are fixed to the right subframe or by changing the angle at which the filament is fixed to the left subframe. The filaments are guided through slots in the platina electrodes, and by applying a downward-directed sloped tensile force, the filaments are kept under tension and also maintain electrical contact with the electrodes. To prevent short circuits between the horizontally and vertically arranged filaments, the filaments are guided individually through cross-shaped insulators.

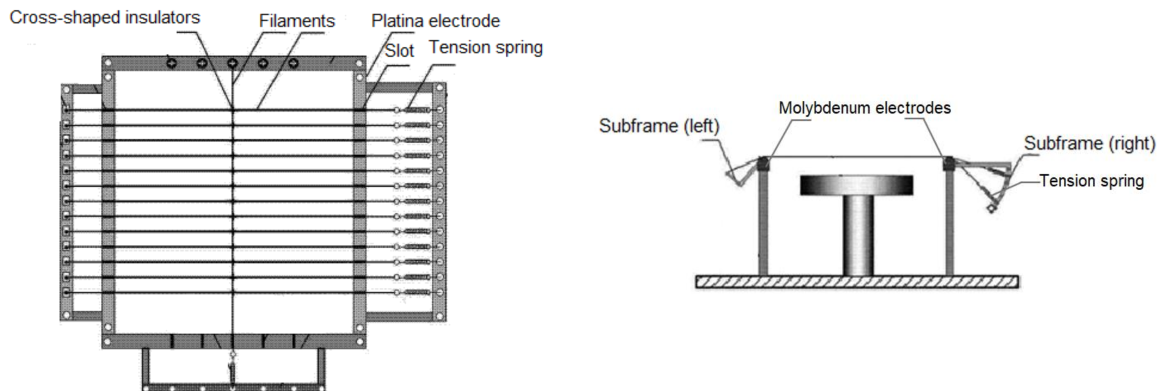

Figure 8.10: Tensioning device for an array of filaments in horizontal and vertical arrangement: top view (left) and side view (right) [75]

Another approach to prevent breakage of the filaments during operation is to use an adjustable force regulator (see Figure 8.11) [73]. This force regulator is used to adjust and control the force on an array of filaments and is attached to a movable electrode that can slide on a titanium support rod. The force regulator consists of a tension spring and an adjustment screw. The spring is attached to the adjustment screw on one end and to a movable electrode on the other. Tightening or loosening the screw manually will decrease or increase the amount of tension force supplied by the tension spring. A spring with a low spring rate (i.e., force divided by change in spring length) is preferred in order to minimize the change in tension force as the filaments expand. The force regulator provides a sufficient amount of tension (up to about 0.027 N for a single filament) to accommodate the thermal and carburization expansion of the filaments. To maximize the mechanical reliability of the force regulator, it is advised to place the force regulator either outside or in the cooler zone of the reactor, as this may prevent or minimize the carburization of the components.

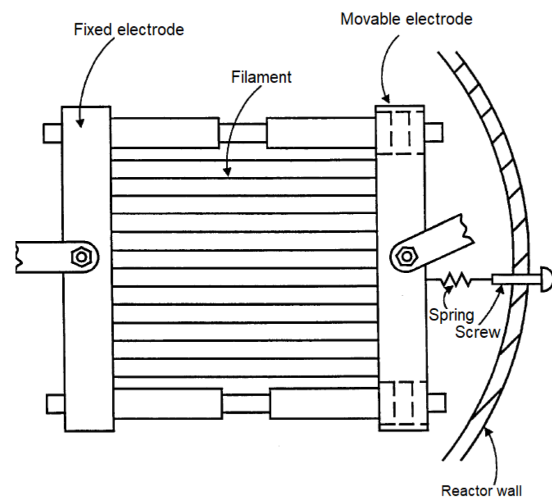

Figure 8.11: Top-view of the adjustable force regulator used for tensioning the filaments [74]

Most of these designs have been suggested as solutions to extend the lifespan of the filaments in HF-CVD processes that are carried out continuously. Here, the filaments are maintained at their incandescent temperature for the remainder of their operating life. The cooling and contraction of the filaments and their associated thermal stresses were not considered design parameters. Nonetheless, the adjustable tensioning mechanism has the option to increase and decrease the tension on the filaments during the HF-CVD process.

B. Methodology (Supplementary)

B1. HF-CVD setup (1st generation)

The previous HF-CVD setup (see Figure 8.12) consists of a 6-way cross reaction chamber. The front flange, upper flange, and right flange can be opened and closed. The front flange allows users to insert and extract the samples. This flange is equipped with a transparent quartz glass window, allowing users to visually observe and monitor the CVD process in real-time. Each tube of the HF-CVD setup is water-cooled. The gas feed system allows the introduction of various gases, including argon, hydrogen, methane, and nitrogen at controlled mass flow rates. To maintain low pressure conditions, a vacuum system is employed. A coiled W (or Ta) filament is position between the two molybdenum electrodes. The Molybdenum electrodes are mounted to the upper flange. A DC power supply provides the electrical power to the filaments. The stage is heated through induction heating.

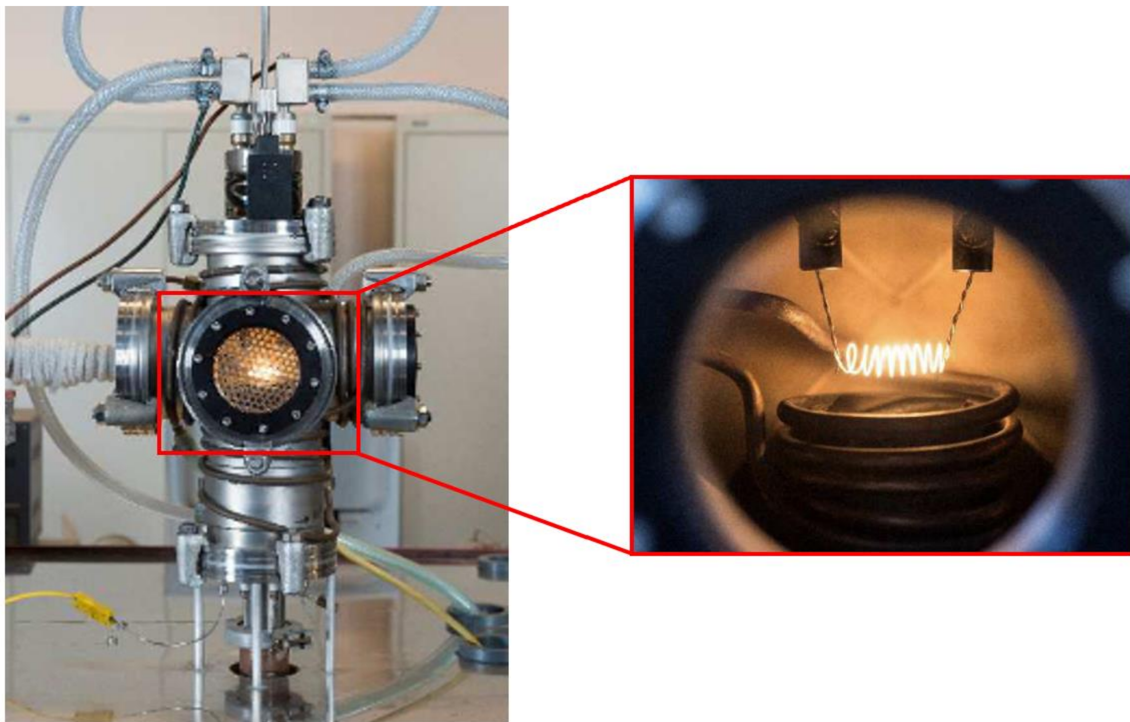

Figure 8.12: HF-CVD setup (1st generation) with a close-up view on the inside

B2. Filament straightening protocol

Several methods can be used for straightening the W wires. The approach used in this research was based on a careful evaluation of available options and weighing factors such as simplicity, effectiveness, and the availability of in-house equipment. For this method, a vise and a drill machine were required. The filaments were prepared by performing the following sequence of steps:

(1) To prevent any contamination, gloves were worn before initiating the straightening process;
(2) A portion (0.5 m – 1 m) of the W wire was gently uncoiled and cut from the spool;
(3) One end of the cut wire was securely clamped in the vise, while the other end was fixed in the chuck of the drill machine (see Figure 8.13);
(4) The drill machine operated at a moderate speed while applying a steady and constant tensile force to the wire;
(5). The rotating direction was alternated every 4-5 turns to prevent the formation of kinks or snapping of the wire;
(6) After achieving a relatively straight wire, the wire was cut into smaller and more manageable lengths (~ 15 cm);
(7) Each of these smaller wires was then placed in the vise and straightened manually;
(8) Each wire was inserted into a custom shaping device, which shaped the wire into its final form;
(9) The excessive lengths were cut off, and each filament was decontaminated using ethanol.

Figure 8.13: Filament fixation during the straightening process (step 3)

B3. Filament-substrate distance measurement

To ensure accurate and reliable results, the change in filament-substrate distance as a result of carburization and subsequent sagging was also taken into account. The filament-substrate distance was measured before and after each experiment. A gauge block with a height of 5 mm was used as a reference to set up the scaling in ImageJ in order to determine the exact filament-substrate distance through image analysis (see Figure 8.14).

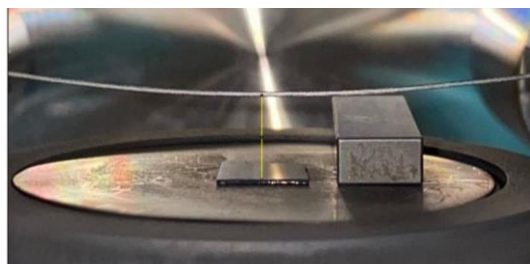

Figure 8.14: Image analysis to determine filament-substrate distance (ImageJ)

B4. Wobbling of the substrate

At the beginning of this project, when the 2” wafer was positioned in the center of the rotating stage, the wafer exhibited a noticeable wobbling effect during the deposition process. To overcome this, different placements of the wafers on the stage were tested (see Figure 8.15). The wobbling effect was eliminated when the wafer was intentionally positioned off-center, creating a noticeable gap on the other side. This placement facilitated the effective escape of the gas that had built-up underneath the wafer.

Gap
2'' Si wafer
Stage (without sample)
Sample placed in the middle (wobbling)
Sample placed not in the middle (no wobbling)

Figure 8.15: Different placements of the 2" Si wafer to prevent wobbling

B5. Grain size and film thickness analysis

The average grain sizes of each experiment were determined using four different SEM images (top view), and on each SEM image, 25 randomly selected grains were measured (see Figure 8.16. The average thickness was based on 10 measurements from different SEM images (cross-sections). The measurement tools that were available in the associated SEM software (In Touch Scope) were used, and the data was processed in Excel.

SEI 20kV WD27mm SS30 x15,000 1μm
SEI 15kV WD27mm SS35 x10,000 1μm
1.960μm

Figure 8.16: SEM images of surface (left) and cross-section (right) morphologies

C. Experimental results (Supplementary: SEM, higher methane concentrations & prototype)

C1. Zoomed-out SEM of diamond films obtained from the growth study

The surface morphologies of samples obtained throughout the experimental parametric growth study are shown in Figure 8.17, Figure 8.18, and Figure 8.19, respectively. These SEM images provide a zoomed-out view.

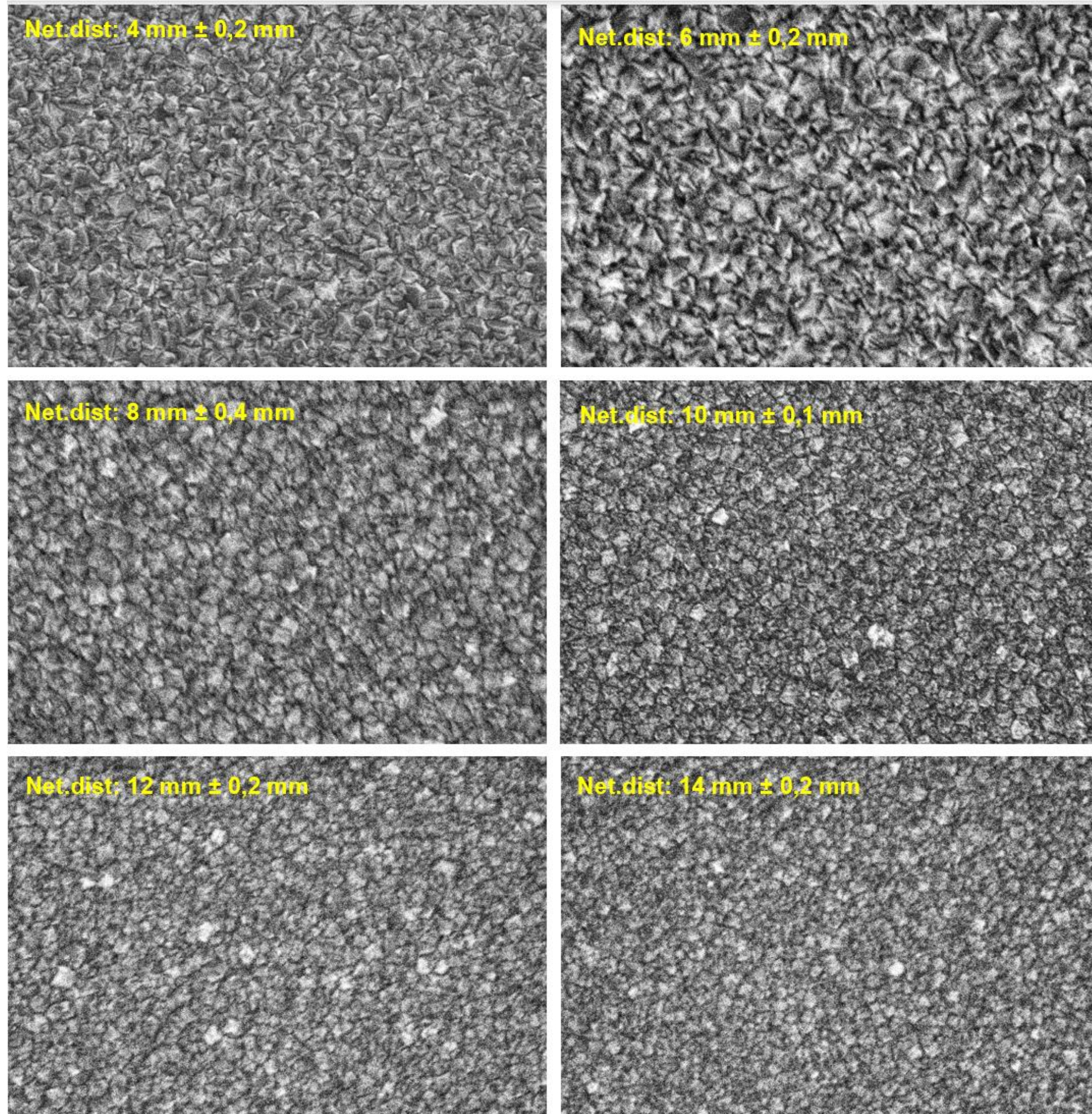

Figure 8.17: Zoomed-out SEM images of surface morphology of samples obtained at various filament-substrate distances, stage T = 780 °C and 1.0 vol.% methane was used

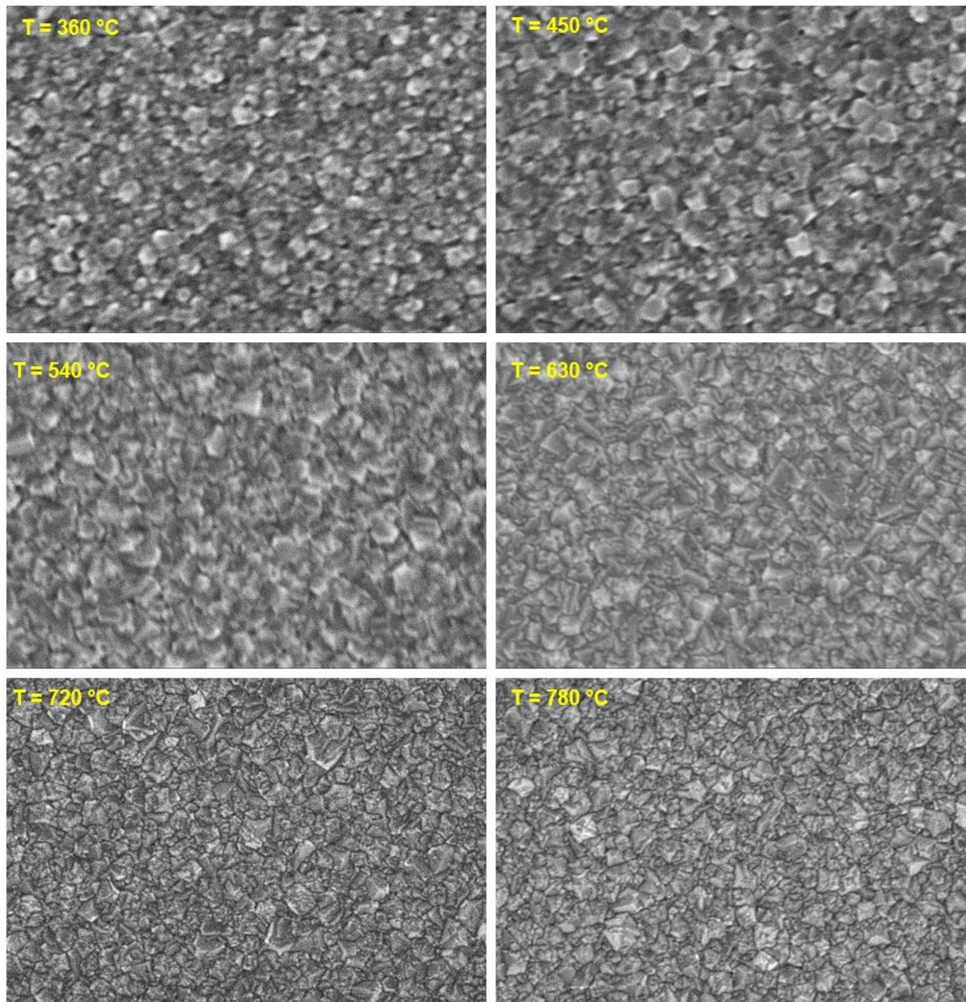

using different stage temperatures, filament-substrate distance was set at 10 mm and 1.0 vol.% methane was used

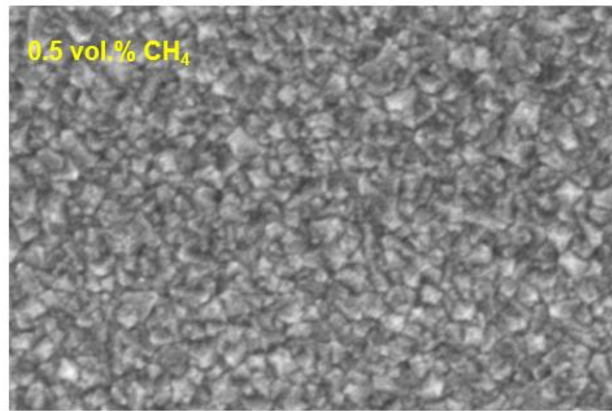

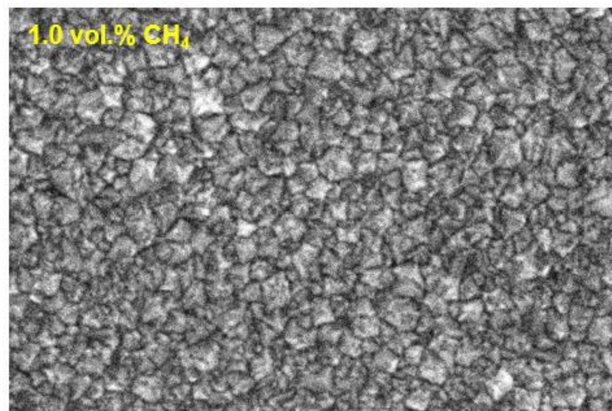

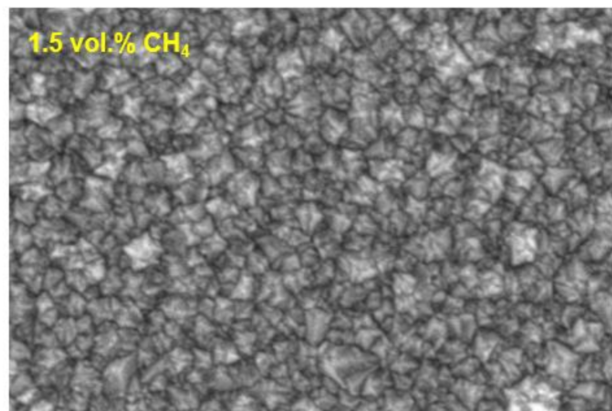

Figure 8.19: Zoomed-out SEM images of surface morphology of samples obtained using different methane concentrations, filament-substrate distance was set at 10 mm and stage temperature was 780 °C

C2. Diamond films obtained using higher methane concentrations (2.0 vol.% and 3.0 vol.%)

Throughout this research, additional experiments were conducted. However, these results were not included in the results and discussion section due to small deviations in filament-substrate distances. The filament-substrate distance was not consistently set at 10 mm. However, these experiments do provide valuable insights. The experiments conducted at methane concentrations of 2.0 vol.% and 3.0 vol.% showed the formation of unfaceted diamond grains and cauliflower-like diamond grains, as can be seen in Figure 8.20. These observations align with the expected outcomes expected when increasing the methane concentration.

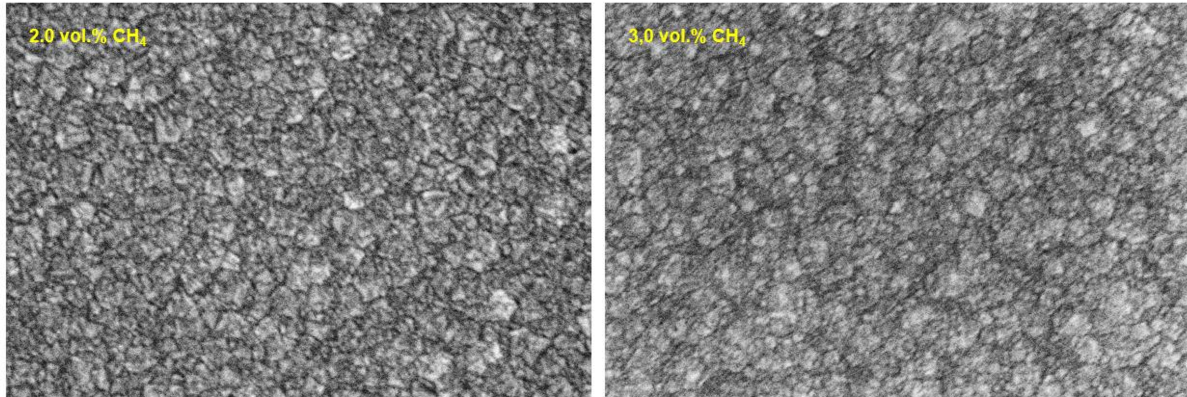

Figure 8.20: SEM images of experiments performed using 2.0 vol.% methane (filament-substrate distance: 11.5 mm) and 3.0 vol.% methane (filament-substrate distance: 9.7 mm)

C3. 3D printed prototype (Concept 1)

The first conceptual design of the clamping device was 3D-printed and tested to evaluate its compatibility with the HF-CVD setup. The entire assembly did fit within the HF-CVD setup (see Figure 8.21), and the clamping device aligned perfectly with the underlying copper electrodes. Additionally, the rotating leg safely avoided physical contact with the reactor, even in its maximum extended position. Furthermore, the stage did fit within the available space between the two molybdenum electrodes, allowing for height adjustments in the z-direction without any interference or contact with the electrodes. The insertion and extraction of the clamping were carried out with precision due to the limited space between the clamping device and the inner diameter of the front flange.

Figure 8.21: 3D-printed clamping device (prototype) inserted in the HF-CVD setup

D. User manual – Hot-filament chemical vapor deposition (HFCVD) system

User guide for diamond growth

Step 1: Starting up the HFCVD system

1.1. Turn the main power switch ON (*if it is not switched on already, this switch can be found on the backside of the setup*).

1.2. Turn the vacuum pump ON (switch on the backside).

1.3. Turn the cooling system ON (switch on the back side).

1.4. Press and hold the [RUN/STOP] button for 1 second to start the cooling process.
(*Make sure that the target cooling temperature is set to ~18 °C, the target temperature can be adjusted by using the [▲] [▼] keys).*

1.5. Turn the substrate stage heater controller (green switch) ON and enable the output (blue switch).

1.6. Turn the computer ON (login with username **.\Diamandreactor** and password **Reactor01**) and launch the software 'CVD Reactor simple V1.6-Shortcut'.

1.7. Press the RUN button in the software (the vacuum pump will be turned off automatically).

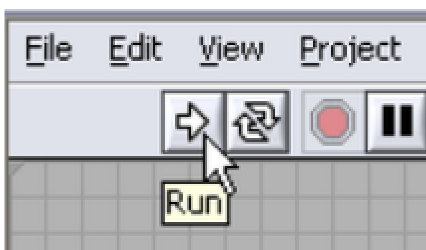

Step 2: Load the sample

2.1. Open the needle valve fully. Once at ambient pressure (~996 mbar on the display), wait for ~1 minute until a ‘gasp’ sound is audible.

2.2. Open the front flange by loosening the knurled screw.

2.3. Adjust the distance between the filament and the substrate holder to ~38.50 mm by turning the rotary wheel located below the setup.

2.4. Place the sample at the center of the substrate holder.
Be careful, do NOT touch the filament (extremely fragile)!

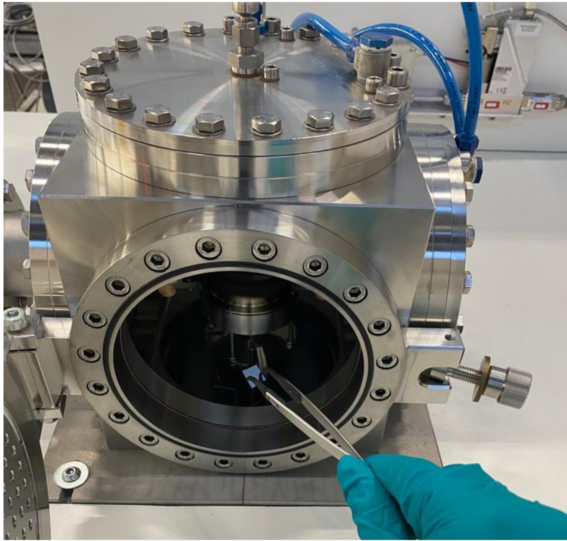

2.5. Close the front flange by applying a moderate force to the knurled screw.

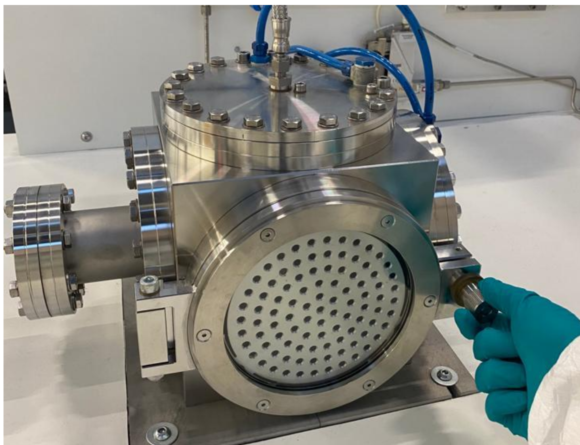

2.6. Set the distance between the filament and the substrate holder back to ~10 mm.

2.7. Turn the pump ON in the software and set the pump speed at level 5.

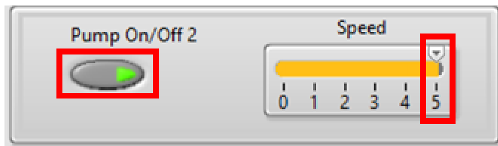

Step 3: Turn on the power supply

3.1. Turn the power supply ON for the filament and then press the [OUTPUT ON/OFF] button once.

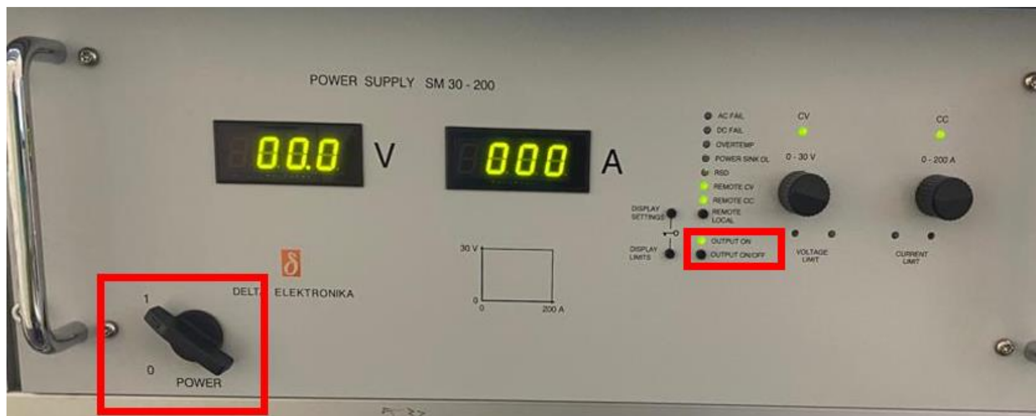

3.2. Turn the power supply ON for the substrate heater.

Step 4: Flush the HFCVD chamber

4.1. Open the main argon (Ar) valve manually.

4.2. Open the argon needle valve fully.

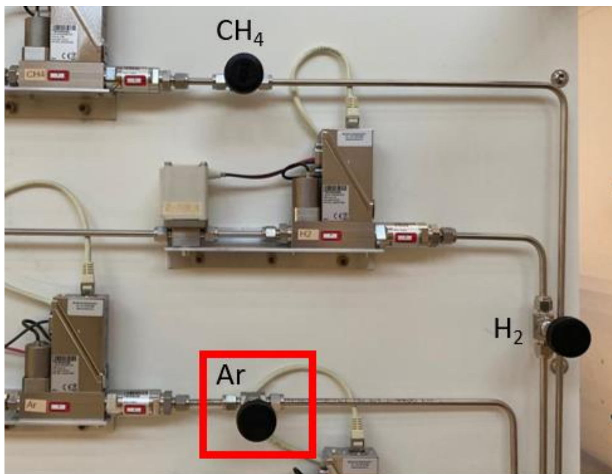

4.3. Open the second argon valve by clicking on the argon valve icon in the software.

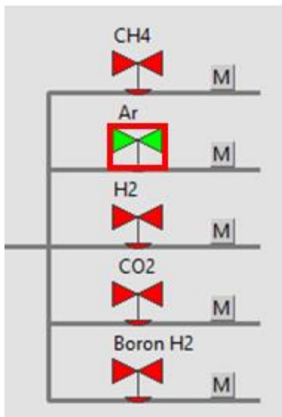

4.4. Set the argon mass flow to 250 sccm and press enter.

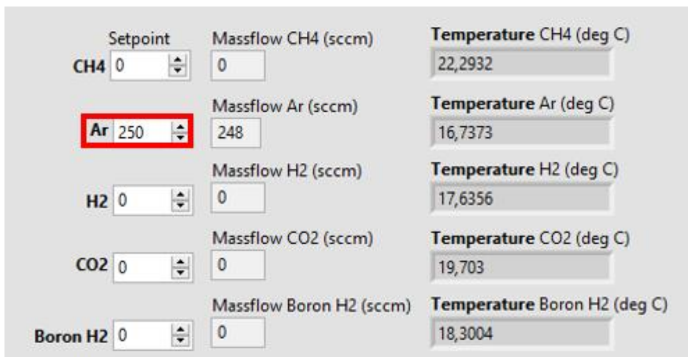

4.5. After ~10 seconds turn off the argon valve by clicking on the argon valve icon.

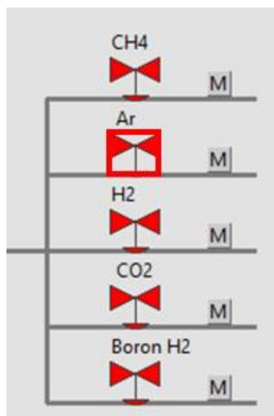

4.6. Open the main vacuum valve in the software and wait until the pressure stabilizes.

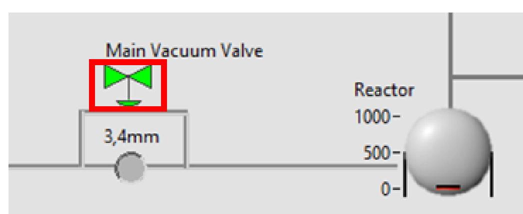

4.7. Close the main vacuum valve in the software.

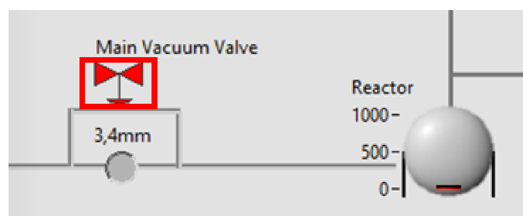

4.8. Repeat steps 4.3, 4.4, 4.5, 4.6 and 4.7 several times (~3). (Before proceeding to step 5, make sure that the pressure is in the range of 5E-2 – 8E-2 mbar.)

Step 5: Set process gas composition and flow

5.1. Open the main hydrogen (H_2) and methane (CH_4) valve manually.

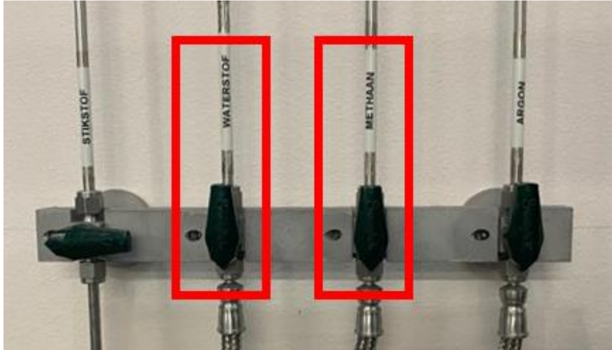

5.2. Open the hydrogen and methane needle valves fully.

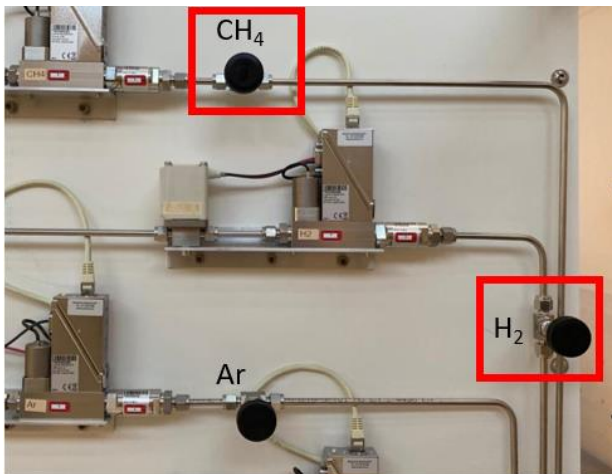

5.3. Open the second hydrogen valve by clicking the hydrogen valve icon in the software.

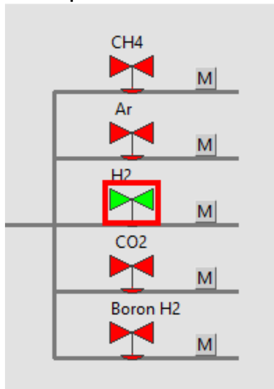

5.4. Gradually increase the hydrogen flow in steps of 100 sccm (0 → 100 → 200 → 300 sccm) until the final/desired gas flow is reached. Make sure to let the pressure stabilize after each increment.

5.5. Open the second methane valve by clicking the methane valve icon in the software.

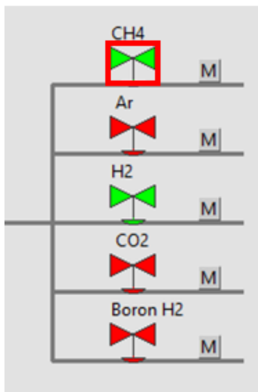

5.6. Set the final/desired value for the methane gas flow (for example, 3 sccm CH_4 and 300 sccm H_2 to set the process gas ratio at CH_4 : H_2 ~ 1 : 99).

Setpoint Massflow CH4 (sccm)

CH4 3 2,999

Step 6: Initiate the diamond growth process

6.1. Turn the heater stage ON by clicking on the 'Heater stage' switch and then click the [Apply] button.

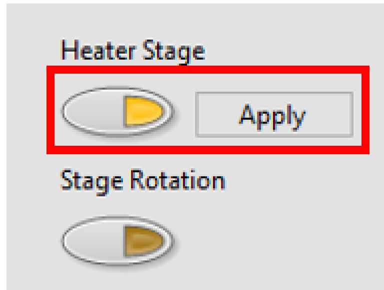

6.2. Turn the stage rotation ON.

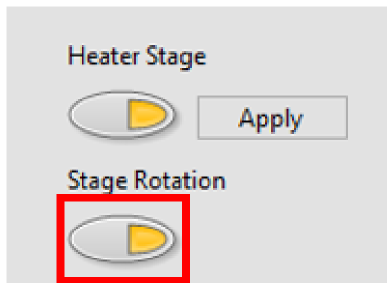

6.3. Tick the Low Power Data box and save the file.

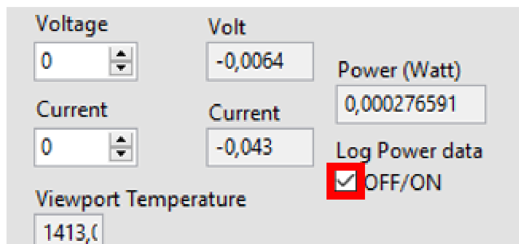

6.4. Set the filament voltage to 30 V and press enter.

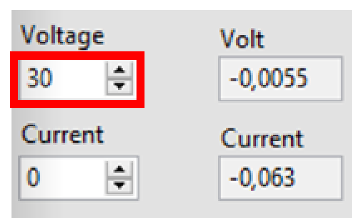

6.5. **Gradually increase** (at a rate of 0.1 A/s) the filament current to its final desired value (e.g., 23 A).

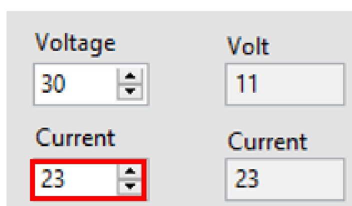

Step 7: Monitor the growth process

7.1. Monitor the growth process by filling in the 'process protocol sheet'.

Operator: Process protocol - Carburisation Date: ___ - ___ - ___

Step #	t (hh:mm)	Pressure (mbar)	H_2 flow (sccm)	CH_4 flow (sccm)	Current (A)	Voltage (V)
1	0:00					
2	0:15					
3	0:30					
4	0:45					
5	1:00					
6	1:15					
7	1:30					
8	1:45					
9	2:00					
10	2:15					
11	2:30					
12	2:45					
13	3:00					
14	3:15					
15	3:30					
16	3:45					
17	4:00					

7.2. Check the sample regularly (e.g., every 30 minutes) by wearing the safety goggles.

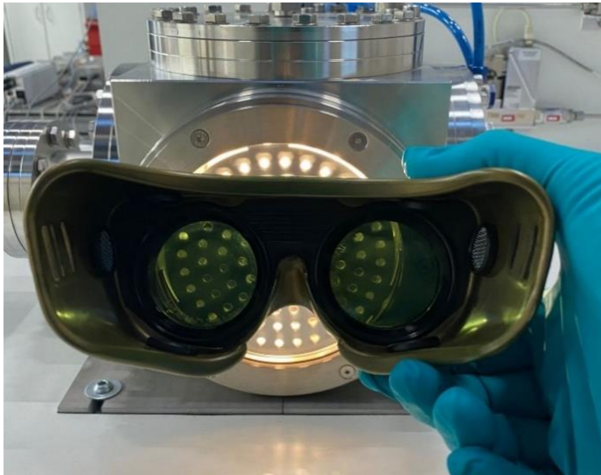

7.3. Interrupt the procedure immediately in the following situations:
(a). Visible sparks inside the chamber → press the [Emergency Stop] button.
(b). Crack in the window → press the [Emergency Stop] button.
(c). Gas leakage → press the [Emergency Stop] button and CLOSE the main valves.
(d). When in doubt of an emergency → press the [Emergency Stop] button.

7.4. Interrupt the procedure according to the 'finish growth & shut down procedure' (steps 8 & 9) in the following situations:
(a). Filament fails (current becomes 0 A).
(b). A sudden change in pressure of more than 10%.
(c). A change or deviation in gas flow of more than 10%.
(d). If the cooling is not working (target temperature and measured temperature deviate >3 °C).
(e). Sample is not visible anymore on the substrate holder.
(f). To extract your sample.

Step 8: Finish the diamond growth process

8.1. Adjust the distance between the filament and the substrate holder to ~38.50 mm by turning the rotary wheel located below the setup.

8.2. Turn OFF the heater stage by clicking on the 'Heater stage' switch and then click the [Apply] button.

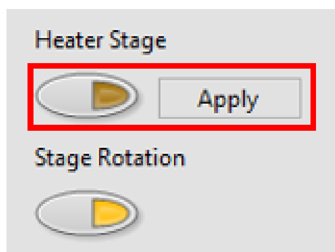

8.3. Turn OFF the stage rotation.

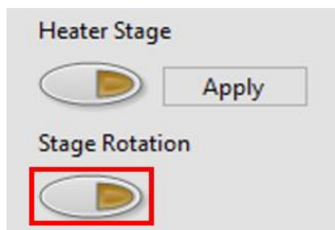

8.4. **Gradually decrease** (at a rate of 0.1 A/s) the filament current to 0 A.

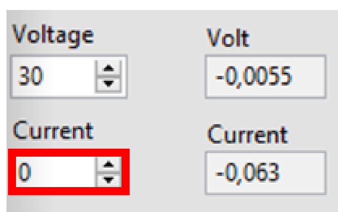

8.5. Wait and let the system cool down (until the stage temperature is ~ 65 °C).

8.6. Close the methane and hydrogen needle valves.

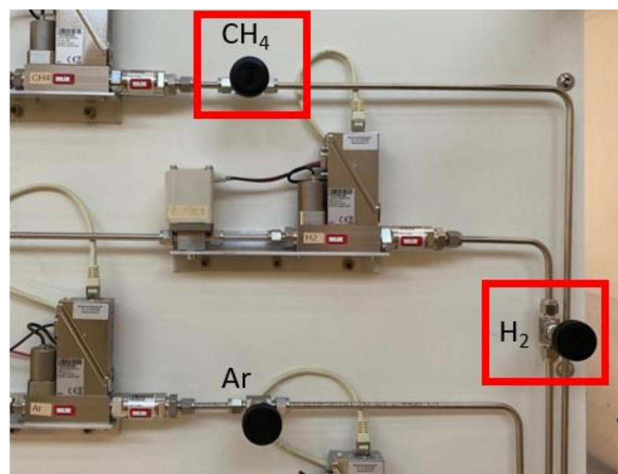

8.7. Monitor the gas flow and wait until the gas flow is 0 sccm.

	Setpoint	Massflow (sccm)	Temperature (deg C)
CH4	0	Massflow CH4 (sccm): 0	Temperature CH4 (deg C): 19,2951
Ar	0	Massflow Ar (sccm): 0	Temperature Ar (deg C): 14,4542
H2	0	Massflow H2 (sccm): 0	Temperature H2 (deg C): 14,9304
CO2	0	Massflow CO2 (sccm): 0	Temperature CO2 (deg C): 19,3996
Boron H2	0	Massflow Boron H2 (sccm): 0	Temperature Boron H2 (deg C): 17,8962

8.8. Close the hydrogen valve by pressing on the hydrogen valve icon in the software.

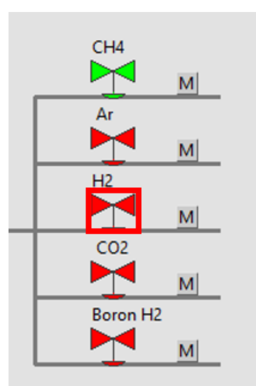

8.9. Close the methane valve by pressing on the methane valve icon in the software.

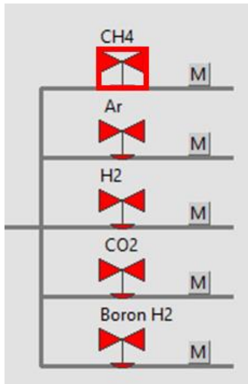

Step 9: Shut down the HFCVD system

9.1. Open the main vacuum valve in the software and wait until the pressure stabilizes (~5 E-2 – 7 E-2 mbar)

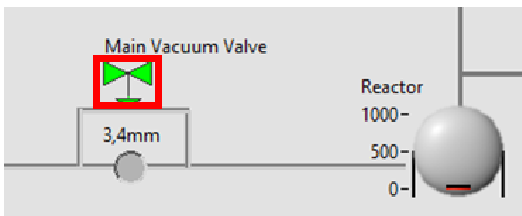

9.2. Close the needle valve manually (clockwise rotation).

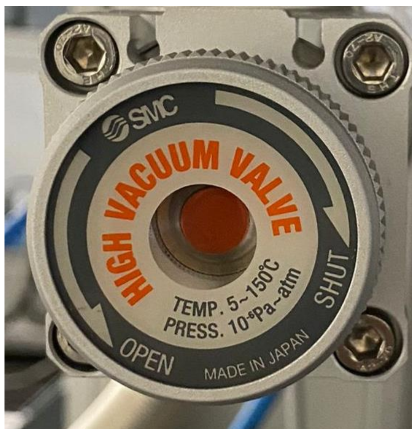

9.3. Close the main vacuum valve in the software.

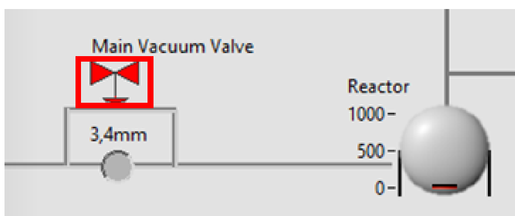

9.4. Turn the vacuum pump OFF in the software.

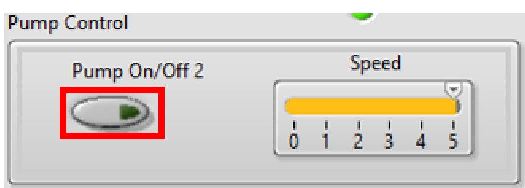

9.5. Close all main gas valves manually.

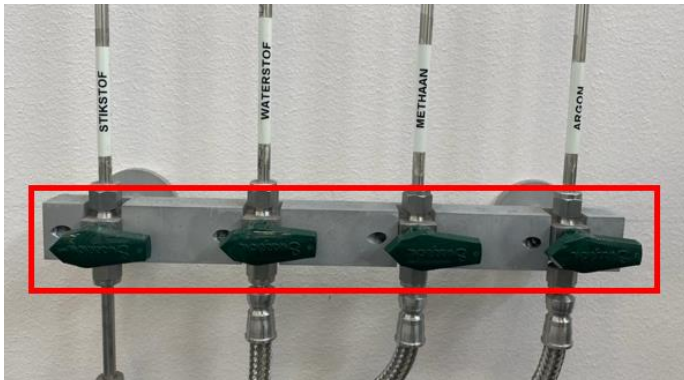

9.6. Turn OFF the power to the filament.

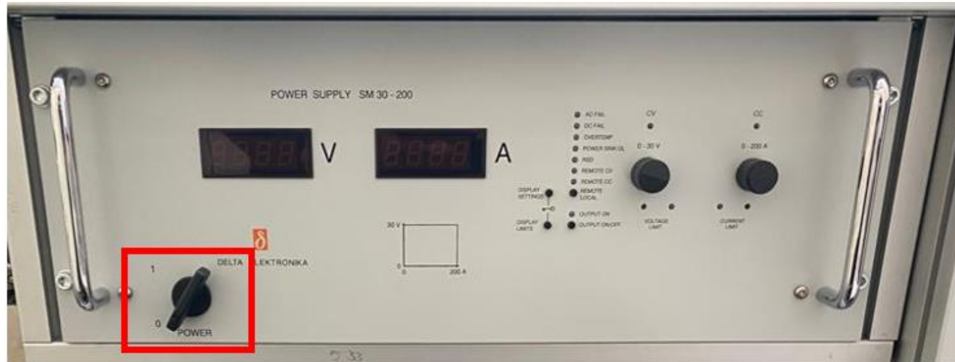

9.7. Turn OFF the power to the substrate heater.

9.8. Press and hold the [RUN/STOP] button for 1 second and turn OFF the water cooling system.

9.9. Turn the vacuum pump OFF.

9.10. Press the STOP button and close the software.

9.11. Turn the substrate stage heater controller (green switch) OFF and disable the output (blue switch).

Step 10: Sample extraction

10.1. Let the chamber cool down for several hours.
10.2. Follow steps 2.1, 2.2 and 2.3. **Be careful, do NOT touch the filament (extremely fragile)!**
10.3. Extract your sample.
10.4. Close the front flange by applying a moderate force to the knurled screw. (see step 2.5)
10.5. Turn ON the vacuum pump and wait until the pressure stabilizes. (see step 1.2)
10.6. Close the needle valve manually. (see step 9.2)
10.7. Turn the vacuum pump OFF. (see step 9.9)